



**HAL**  
open science

# Elaboration of photocatalytically active composite materials for environmental applications

Šárka Paušová

► **To cite this version:**

Šárka Paušová. Elaboration of photocatalytically active composite materials for environmental applications. Other. Université Blaise Pascal - Clermont-Ferrand II, 2014. English. NNT : 2014CLF22475 . tel-01138210

**HAL Id: tel-01138210**

**<https://theses.hal.science/tel-01138210>**

Submitted on 1 Apr 2015

**HAL** is a multi-disciplinary open access archive for the deposit and dissemination of scientific research documents, whether they are published or not. The documents may come from teaching and research institutions in France or abroad, or from public or private research centers.

L'archive ouverte pluridisciplinaire **HAL**, est destinée au dépôt et à la diffusion de documents scientifiques de niveau recherche, publiés ou non, émanant des établissements d'enseignement et de recherche français ou étrangers, des laboratoires publics ou privés.

N° d'ordre : D.U. 2475

## UNIVERSITE BLAISE PASCAL

U.F.R. Sciences et Technologies

### ECOLE DOCTORALE DES SCIENCES FONDAMENTALES

N° 793

## THESE

Présentée pour obtenir le grade de

**DOCTEUR D'UNIVERSITE**

Spécialité : Chimie Physique

**Par Šárka Paušová**

---

### Elaboration de matériaux composites photocatalytiquement actifs pour des applications environnementales

---

Soutenue publiquement le 25 septembre 2014 devant la commission d'examen.

**Rapporteurs :**

Dr. Florence BENOIT-MARQUIE (Université Paul Sabatier Toulouse, France)

Dr. Michal VESELY (Université Technique de Brno, République Tchèque)

**Examineurs :**

Pr. Karel BOUZEK (VSCHT Prague, République Tchèque)

Dr. Vlastimil FILA (Université Blaise Pascal, France)

Dr. Gilles MAILHOT (Université Blaise Pascal, France)

Dr Vanessa PREVOT (Université Blaise Pascal, France)



I hereby declare that this thesis is my own work. Where other sources of information have been used, they have been acknowledged and referenced in the list of used literature and other sources. I have been informed that the rights and obligations implied by Act No. 121/2000 Coll. on Copyright, Rights Related to Copyright and on the Amendment of Certain Laws (Copyright Act) apply to my work. In particular, I am aware of the fact that the Institute of Chemical Technology in Prague has the right to sign a license agreement for use of this work as school work under §60 paragraph 1 of the Copyright Act. I have also been informed that in the case that this work will be used by myself or that a license will be granted for its usage by another entity, the Institute of Chemical Technology in Prague is entitled to require from me a reasonable contribution to cover the costs incurred in the creation of the work, according to the circumstances up to the full amount. I agree to the publication of my work in accordance with Act No. 111/1998 Coll. on Higher Education and the amendment of related laws (Higher Education Act).

In Prague on .....

First of all, I would like to thank my supervisors Prof. Dr. Ing. Josef Krýsa, Dr. Vanessa Prevot and Dr. Gilles Mailhot for their guidance, help and support during the preparation of this thesis. I would also like to thank RNDr. Jaromír Jirkovský, CSc. for his valuable advices, suggestions and ideas. I would like to thank my colleague Ing. Martin Zlámal Ph.D. for helpful discussions regarding the photocatalysis. Many thanks belong to all members of the laboratories and Ph.D. students of ICCF in Clermont Ferrand and Department of Inorganic technology, ICT Prague. I also highly appreciate the financial support of French government (BGF). Last but not the least I would like to thank my family and friends for the support and patience they gave me.



## Résumé

Ce travail décrit la synthèse et le comportement de nouveaux photocatalyseurs à base de dioxyde de titane utilisés pour des applications environnementales. Dans la première partie, la pertinence des composés testés, le colorant acide orange 7 (AO7) et le 4-chlorophénol (4-CP), pour des traitements photocatalytiques à base de  $\text{TiO}_2$  a été étudiée et validée. Cette étude a été centrée sur l'effet de la concentration initiale en composé et sur la vitesse d'agitation pendant la réaction photocatalytique. La deuxième partie est consacrée principalement à la synthèse et la caractérisation des suspensions de particules colloïdales de  $\text{TiO}_2$ . Cependant, leur séparation puis leur récupération après le traitement est pratiquement impossible. Pour cette raison, nous avons cherché à immobiliser ces particules sur des supports, les hydroxydes doubles lamellaires (HDL) qui sont connus pour être de bon support photocatalytique. Nous avons concentré le travail afin de préparer un matériau composite  $\text{TiO}_2$ /HDL présentant la même activité photocatalytique que le dioxyde de titane pur. Le deuxième type de composite étudié est basé sur des mélanges de  $\text{TiO}_2$ / $\text{SiO}_2$  qui ont été utilisés aussi dans la préparation de fines couches. Enfin, le comportement photocatalytique d'HDL seul, sans addition de  $\text{TiO}_2$ , a également été étudié et est présenté dans la partie finale de cette thèse.

*Les matériaux préparés ont été caractérisés par différentes analyses chimiques, diffraction et fluorescence des rayons X, microscopie électronique à transmission et à balayage, spectroscopie IR à transformé de Fourier, analyse thermogravimétrique, mesure du potentiel Zeta, diffusion de la lumière, mesure d'adsorption  $\text{N}_2$ . Les différents matériaux ont été testés photocatalytiquement via la photo-oxydation en solution aqueuse de l'acide orange 7 (AO7), du 4-chlorophénol (4-CP) ou du bleu de méthylène à différents pH. L'activité photocatalytique du matériau composite à base de  $\text{TiO}_2$ / $\text{SiO}_2$  sous forme de film fin a été évaluée en phase gaz en présence d'hexane.*

Nous avons trouvé que le rendement quantique de dégradation du 4-CP dans toutes les suspensions colloïdales alcalines de  $\text{TiO}_2$  était plus faible que celui obtenu en milieu acide. Au contraire des suspensions en milieu acide qui restent stable d'un point de vue photochimique, le rendement quantique des suspensions de  $\text{TiO}_2$  en milieu alcalin décroît au cours du vieillissement. Dans le cas du nanomatériau préparé  $\text{TiO}_2$ / $\text{Mg}_2\text{Al}_{1.5}$  l'activité photocatalytique est plus forte que celle observée en milieu basique avec les particules originales de  $\text{TiO}_2$  et il est également beaucoup plus aisé de récupérer le photocatalyseur par simple sédimentation après le traitement. Dans le cas des composites  $\text{TiO}_2$ / $\text{SiO}_2$  il a été trouvé que le composite avec un ratio 1:1 avait une activité photocatalytique plus forte que le  $\text{TiO}_2$  de départ mais si l'on augmente la part de  $\text{SiO}_2$  la vitesse de dégradation de l'AO7 diminue. Les films fins de  $\text{TiO}_2$ : $\text{SiO}_2$  préparés par co-précipitation sont capables de dégrader photocatalytiquement l'hexane. Dans le cas des HDL purs, il a été montré que même non-calciné  $\text{Zn}_2\text{CrCO}_3$  produit des radicaux  $\text{HO}^\bullet$ . Cependant, des oxydes mixtes (contenant ZnO) préparés par calcination des HDL à des températures supérieures à  $500^\circ\text{C}$  montrent une plus grande efficacité.



## Summary

This work describes the behaviour and fabrication of new photocatalysts based on titanium dioxide for the purpose of environmental applications. It consists of five closely connected parts. In the first part the suitability of chosen model compounds, azo dye Acid Orange 7 (AO7) and 4-chlorophenol (4-CP), for photocatalytic activity assessment of  $\text{TiO}_2$  was studied. This study was focused on the effect of different initial concentrations of model compound and different rates of stirring during photocatalytic reaction. The second part then focused mainly on the synthesis and characterization of aqueous colloidal suspensions of  $\text{TiO}_2$ . The separation of  $\text{TiO}_2$  particles in the form of colloidal suspensions and their regeneration after the reaction, while keeping the same photocatalytic properties, is almost not possible. Therefore, it was necessary to find an appropriate method how to immobilize these particles on the support or in the form of composite. The layered double hydroxides (LDH) were chosen as one of suitable supports for  $\text{TiO}_2$  photocatalyst. The focus was kept on the preparation of  $\text{TiO}_2$ /LDH composites with the same or higher photocatalytic activity as pure colloidal titanium dioxide. The second chosen type of composite was based on two-component  $\text{TiO}_2$ / $\text{SiO}_2$  material and these composites were used for the preparation of thin layers. Photocatalytic behaviour of pure LDHs and their possible use as photocatalyst without  $\text{TiO}_2$  addition was also studied and described in a final part of this work.

*Prepared materials were characterized by chemical analysis, X-ray diffraction and fluorescence, transmission electron microscopy, scanning electron microscopy, Fourier transform infrared spectroscopy, thermogravimetric analysis, dynamic light scattering, zeta potential measurement and  $\text{N}_2$  adsorption. As another step, materials were tested as photocatalyst by the photooxidation of Acid Orange 7, 4-chlorophenol and Methylene Blue in different pH in aqueous medium. Photocatalytic activity of  $\text{TiO}_2$ / $\text{SiO}_2$  composites in the form of thin films was tested in gaseous phase using hexane as a model pollutant.*

It was found that quantum yields of 4-CP degradation for all prepared alkaline colloidal suspensions of  $\text{TiO}_2$  were lower than those obtained for acidic  $\text{TiO}_2$  colloidal suspensions. In the contrary to the quantum yield of acidic  $\text{TiO}_2$ , the quantum yield of alkaline suspensions decreased during the aging. Prepared  $\text{TiO}_2$ / $\text{Mg}_2\text{Al}_{1.5}$  nanocomposites exhibited higher photocatalytic activity than the original  $\text{TiO}_2$  in basic conditions and also it was much easier to recover the photocatalyst after reaction by simple sedimentation. In the case of  $\text{TiO}_2$ / $\text{SiO}_2$  composites, it was found that composite prepared with  $\text{TiO}_2$ : $\text{SiO}_2$  ratio 1:1 has higher photocatalytic activity in aqueous media than starting pure  $\text{TiO}_2$  but with increasing  $\text{SiO}_2$  content reaction rate of AO7 degradation decreases. Thin layers of  $\text{TiO}_2$ : $\text{SiO}_2$  composite prepared from simultaneously co-precipitated particles (they have improved crystallinity in relation to pure  $\text{TiO}_2$ ) are able to photocatalytically degrade hexane. In the case of pure LDH, it was proved that even noncalcined  $\text{Zn}_2\text{CrCO}_3$  LDH can produce  $\text{HO}^\bullet$  radicals. However,

mixed oxides (containing ZnO) prepared by LDH calcination at temperatures higher than 500°C, showed higher efficiency.

## Souhrn

Tato práce popisuje chování a přípravu nových fotokatalyzátorů využitelných pro aplikace v životním prostředí založených na oxidu titaničitým. Celá práce se skládá z pěti těsně spojených částí. V první části byla zkoumána vhodnost vybraných modelových látek, azo barviva Acid Orange 7 (AO7) a 4-chlorfenolu (4-CP), pro stanovování fotokatalytické aktivity  $\text{TiO}_2$ . Tato studie byla zaměřena na vliv různé vstupní koncentrace modelových látek a různých rychlostí míchání během fotokatalytické reakce. Druhá část byla hlavně zaměřena na syntézu a charakterizaci vodných koloidních suspenzí  $\text{TiO}_2$ . Separace  $\text{TiO}_2$  ve formě částic ve formě koloidní suspenze a jejich následná regenerace po reakce za uchování jejich fotokatalytických vlastností je téměř nemožná. Proto bylo nezbytné najít vhodnou metodu imobilizace těchto částic na nosiči nebo ve formě kompozitu. Podvojně vrstevnaté hydroxidy (LDH) byly vybrány jako jeden vhodný nosič pro  $\text{TiO}_2$  fotokatalyzátor. Při syntéze byl kladen důraz na přípravu  $\text{TiO}_2$ /LDH kompozitu se stejnou nebo vyšší fotoaktivitou jako čistý koloidní oxid titaničitý. Druhý vybraný typ kompozitu byl založen na dvousložkovém  $\text{TiO}_2$ / $\text{SiO}_2$  materiálu a tyto kompozity byly také použity na přípravu tenkých vrstev. Fotokatalytická aktivita čistého LDH a jeho možnost použití jako fotokatalyzátoru byla také studována a je popsána v poslední části této práce.

Připravené materiály byly charakterizovány pomocí chemické analýzy, rentgenové difrakce a fluorescence, transmisní elektronové mikroskopie, skenovací elektronové mikroskopie, infračervené spektroskopie s Fourierovou transformací, termogravimetrické analýzy, dynamického rozptylu světla, měření zeta potenciálu a adsorpce  $\text{N}_2$ . Fotokatalytické vlastnosti připravených materiálů byly testovány pomocí fotooxidace Acid Orange 7, 4-chlorfenolu a Methylenové Modře při různých pH ve vodném prostředí. Fotoaktivita  $\text{TiO}_2$ / $\text{SiO}_2$  kompozitů ve formě tenkých vrstev byla testována v plynné fázi za použití hexanu jako modelové látky.

Bylo zjištěno, že kvantový výtěžek degradace 4-CP závisí na pH a pro všechny alkalické koloidní suspenze  $\text{TiO}_2$  byly nižší než u kyselých koloidních suspenzí  $\text{TiO}_2$ . Na rozdíl od kvantových výtěžků kyselých  $\text{TiO}_2$  suspenzí kvantové výtěžky alkalických suspenzí s časem stárnutí klesaly. Dále bylo zjištěno, že fotokatalytická aktivita připraveného nanokompozitu  $\text{TiO}_2$ / $\text{Mg}_2\text{Al}_1.5$  byla vyšší než u výchozího  $\text{TiO}_2$  v alkalickém pH a také bylo jednodušší separovat tento fotokatalyzátor ze systému po reakci prostou sedimentací. V případě  $\text{TiO}_2$ / $\text{SiO}_2$  bylo zjištěno, že kompozity připravené v poměru  $\text{TiO}_2$ / $\text{SiO}_2$  1:1 mají vyšší fotoaktivitu ve vodném prostředí než čistý  $\text{TiO}_2$ , ale s rostoucím obsahem  $\text{SiO}_2$  rychlost degradace AO7 klesá. Současně srážené  $\text{TiO}_2$ : $\text{SiO}_2$  částice vykazují zvýšení krystalinity (vzhledem k čistému  $\text{TiO}_2$ ). Vrstvy připravené z těchto částic  $\text{TiO}_2$ : $\text{SiO}_2$  kompozitů byly schopny fotokatalyticky degradovat hexan v plynné fázi. V případě čistého LDH bylo prokázáno, že při použití  $\text{Zn}_2\text{CrCO}_3$  LDH dochází k tvorbě  $\text{HO}^\bullet$  radikálů. Avšak směsné oxidy (obsahující  $\text{ZnO}$ ), připravené kalcinací tohoto LDH při teplotách vyšších než  $500^\circ\text{C}$ , vykazovaly vyšší účinnost.



# Content

<b>1. INTRODUCTION.....</b>	<b>1</b>
<b>2. RESEARCH GOALS.....</b>	<b>2</b>
<b>3. THEORETICAL PART.....</b>	<b>3</b>
<b>3.1. Photocatalysis.....</b>	<b>3</b>
3.1.1. Principle of photocatalysis.....	3
3.1.2. Decomposition of aqueous pollutants.....	5
3.1.3. Decomposition of gaseous pollutants.....	6
3.1.4. Adsorption isotherm.....	8
3.1.5. Different expressions of photocatalytic activity.....	8
3.1.6. Light sources and influence of light intensity.....	10
3.1.7. Kinetics approach of photocatalytic reactions.....	11
<b>3.2. Photocatalysts.....</b>	<b>12</b>
3.2.1. Titanium dioxide.....	12
3.2.2. Layered double hydroxides.....	17
3.2.3. Composite materials.....	20
<b>3.3. Model compounds for photoactivity evaluation.....</b>	<b>22</b>
3.3.1. Criteria for selection of model compounds.....	22
3.3.2. Parameters influencing degradation of organic compounds in liquid phase.....	23
3.3.3. Photodegradation of dyes.....	23
3.3.4. Photodegradation of pesticides.....	26
3.3.5. Parameters influencing degradation of VOC in gas phase.....	28
<b>4. EXPERIMENTAL PART.....</b>	<b>30</b>
<b>4.1. Preparation of photocatalyst (composite) materials.....</b>	<b>30</b>
4.1.1. Preparation of layers from commercial TiO <sub>2</sub> .....	30
4.1.2. Preparation of TiO <sub>2</sub> nanoparticles.....	30
4.1.3. Preparation of layered double hydroxides.....	30
4.1.4. Preparation of composite materials.....	31
<b>4.2. Characterization methods.....</b>	<b>32</b>
4.2.1. Particle size and zeta potential measurement.....	32
4.2.2. X-ray diffraction and fluorescence.....	32
4.2.3. FT-IR and Raman spectroscopy.....	33
4.2.4. Electron microscopy (FESEM, HRTEM, XPS).....	33
4.2.5. Surface area measurement.....	33
4.2.6. Thermogravimetry analysis.....	34
4.2.7. UV-VIS absorption spectroscopy and band gap energy determination.....	34
4.2.8. Measurement of AO7 adsorption on ZnCr-LDH.....	34
<b>4.3. Photocatalytical measurements.....</b>	<b>35</b>

4.3.1.	Photodegradation in aqueous media, system for the test of suitability of model compounds.....	35
4.3.2.	Photodegradation of model compounds in aqueous media, system for the evaluation of synthesized photocatalysts.....	35
4.3.3.	Photodegradation of model compound in gaseous media.....	36
4.3.4.	HO <sup>•</sup> radical photoproduction rate measurement.....	38
4.3.5.	Liquid-Phase Actinometry Using Potassium Ferrioxalate.....	38
4.3.6.	Measurement of quantum yield of 4-CP photocatalytic degradation.....	40
<b>5.</b>	<b>RESULTS AND DISCUSSION.....</b>	<b>42</b>
<b>5.1.</b>	<b>Photocatalytic evaluation of TiO<sub>2</sub> photocatalysts using model compounds.....</b>	<b>42</b>
5.1.1.	Using of UV-VIS spectroscopy to determine 4-CP and AO7 concentration.....	42
5.1.2.	Influence of initial concentration.....	43
5.1.3.	Influence of mass transfer.....	47
<b>5.2.</b>	<b>Titanium dioxide nanoparticles.....</b>	<b>50</b>
5.2.1.	Influence of pH.....	50
5.2.2.	Influence of temperature and aging.....	54
5.2.3.	Evolution of the band gap energy and photocatalytic activity.....	58
<b>5.3.</b>	<b>TiO<sub>2</sub>/LDH composites.....</b>	<b>63</b>
5.3.1.	Nanocomposite elaboration and characterization.....	63
5.3.2.	Photocatalytic activity.....	69
<b>5.4.</b>	<b>TiO<sub>2</sub>/SiO<sub>2</sub> composites.....</b>	<b>73</b>
5.4.1.	Stability of colloidal suspensions.....	73
5.4.2.	Photocatalytic test of prepared composite suspensions.....	76
5.4.3.	Immobilisation of TiO <sub>2</sub> /SiO <sub>2</sub> composites.....	81
5.4.4.	Relation between surface morphology and photocatalytic activity.....	90
<b>5.5.</b>	<b>ZnCr-LDH.....</b>	<b>97</b>
5.5.1.	Characterization of prepared Zn <sub>2</sub> CrCO <sub>3</sub> -LDH.....	97
5.5.2.	Photocatalytic activity.....	109
5.5.3.	Study of the reaction mechanism.....	120
<b>6.</b>	<b>CONCLUSIONS.....</b>	<b>127</b>
<b>7.</b>	<b>REFERENCES.....</b>	<b>131</b>
<b>8.</b>	<b>APPENDIX.....</b>	<b>143</b>
<b>8.1</b>	<b>Appendix 1 Aging of TiO<sub>2</sub>/SiO<sub>2</sub> 1:1 composites.....</b>	<b>144</b>
<b>9.</b>	<b>LIST OF SYMBOLS AND ABBREVIATIONS.....</b>	<b>145</b>
<b>10.</b>	<b>PUBLICATION AND PRESENTATION ACTIVITY.....</b>	<b>149</b>

# 1. INTRODUCTION

With the increasing agricultural and industrial production, the amount of pollutants released to environment increases. The technologies used for the air and water cleaning mainly consist of conventional phase separation techniques, such as adsorption processes or stripping techniques, and processes designed to destroy the pollutants, chemical oxidation/reduction. The chemical oxidation should be able to lead to the total mineralization of the pollutants to carbon dioxide, water and inorganic salts or at least to the production of harmless organic compounds. However, it was observed that pollutants, which are not biodegradable, are also characterized by high stability or by high difficulty to be completely mineralized [1, 2]. To decompose those pollutants, it is necessary to introduce more effective processes than chemical oxidation. An appropriate technique seems to be a special class of oxidation methods defined as advanced oxidation processes (AOP).

AOPs are based on the generation of very reactive free radicals which are able to destroy pollutants by oxidation. Those radicals are produced using single oxidants (hydrogen peroxide, ozone) or by their combination with UV irradiation (hydrogen peroxide and UVC, ozone and UVC); combination of hydrogen peroxide with ferrous or ferric ion (Fenton processes); combination of hydrogen peroxide with ferrous ion and UV irradiation (photoassisted Fenton processes); and combination of semiconductor catalyst and light irradiation (photocatalysis) [3].

The photocatalysis is a process which uses semiconductor metal oxide as a photocatalyst, oxygen as oxidizing agent and light with proper wavelength as an energy for electron excitation [4]. Thousands of studies have already been published describing the use of photocatalysis for decompositions of many different pollutants. Many different photocatalysts were synthesized and so far titanium dioxide in anatase phase still seems to be the most promising material [5]. However, the intensive research is carried out to develop modified or doped TiO<sub>2</sub>, composite photocatalyst containing TiO<sub>2</sub> or completely new photocatalysts based on different type of metal semiconductors to develop a photocatalyst active in visible light.

The present study describes the preparation and the photocatalytic activity of new types of photocatalysts. The different types of composite materials based on the association of titanium dioxide with other constituent material (layered double hydroxide, silicon dioxide) were prepared, as well as photocatalysts based on layered double hydroxides, whose photocatalytic activity was less studied till now. The suitability of commonly used compounds (Acid Orange 7 and 4-chlorophenol) for the determination of photocatalysts activity and influence of different parameters on their degradation were also studied.

## 2. RESEARCH GOALS

The main objective of this thesis is the development and characterization of two types of inorganic-inorganic composites and evaluation of their performance for environmental applications. The first group of composites is based on the association of TiO<sub>2</sub> nanoparticles with lamellar inorganic matrices - Layered Double Hydroxides, and the second type of nanocomposite is developed by the combination of colloidal suspension of TiO<sub>2</sub> and SiO<sub>2</sub>. The more detailed goals of this work are the following:

- Detailed investigation of Acid Orange 7 and 4-chlorophenol as model compounds for photoactivity assessment of TiO<sub>2</sub> based photocatalysts
- Preparation, characterization and photocatalytic activity assessment of TiO<sub>2</sub> colloidal suspension used further for composite preparation;
- Synthesis and assessment of photocatalytic activity of pure Layered Double Hydroxides;
- Preparation of TiO<sub>2</sub>/LDH and TiO<sub>2</sub>/SiO<sub>2</sub> composite materials, their characterization and photocatalytic activity assessment.
-

### **3. THEORETICAL PART**

#### **3.1. Photocatalysis**

In 1972 Fujishima and Honda reported the photocatalytic water splitting on  $\text{TiO}_2$  electrodes which started a new era in heterogeneous photocatalysis [6]. Since then, researchers put high effort in understanding the fundamental processes and in enhancing the photocatalytic efficiency of  $\text{TiO}_2$  and developing a new photocatalysts. These studies are often related to energy renewal, energy storage and removal of pollutants from environment mainly the degradation of organic pollutants in air and water [7].

The pollution of environment is growing to be bigger problem each year. So it is necessary to find a suitable method for cleaning of waste waters and polluted air. These days commonly used methods are non-biological processes (mechanico-physical, chemical, electrochemical process etc.) and biological processes. But some of the pollutants (azo dyes, pesticides etc.) are resistant to biological attack, light, heat or oxidation. So the photocatalysis seems to be a suitable method how to perform the degradation of these organic pollutants because it is a process which allows destruction of persistent molecules by highly reactive non-selective hydroxyl radical oxidation.

##### **3.1.1. Principle of photocatalysis**

Photocatalysis is a process in which a chemical reaction takes place only in the presence of photocatalyst and light irradiation. Photocatalyst is therefore a substance which becomes a catalyst after absorption of light. Heterogeneous photocatalytic processes are generally carried out by using semiconductor photocatalyst particles suspended or immobilised on a support in aqueous or gaseous medium and irradiated by monochromatic or polychromatic light with energy that exceeds the band gap energy of the used photocatalyst material. Principle of photocatalysis is shown in Fig. 1.

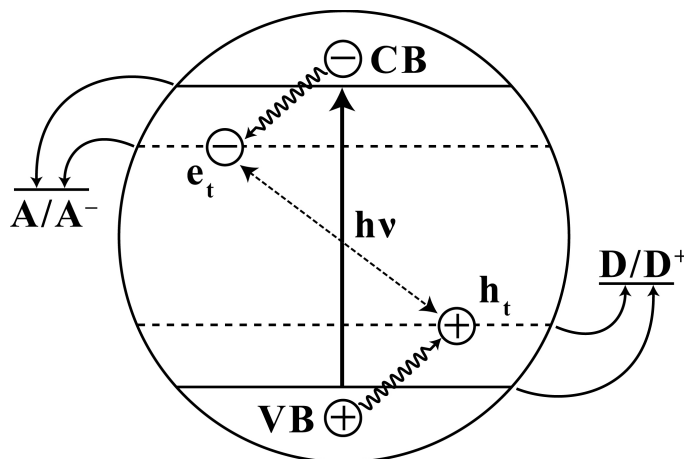


Fig. 1: Schema of the photocatalysis – CB – conduction band, VB – valance band, D – donor, A – acceptor,  $h_t$  – positive hole,  $e_t$  – electron

Absorption of the photon with band gap energy higher than the semiconductor band gap energy results in the formation of conduction band electron and valance band hole, according to the reaction:



Photogenerated  $h^+$  and  $e^-$  have strong oxidation and reduction power. The hole is quickly converted to the hydroxyl radical upon oxidation of surface water as it is shown in following reaction:



The formed hydroxyl radical is the major reactant, which is responsible for oxidation of organic substrate [8].



Electrons most often react with dissolved O<sub>2</sub> with formation of superoxide radical (  $O_2^{\bullet -}$  ) according to the equation (3-1-3). They can further react and produce HO• radicals (3-1-4) and thus contribute to oxidation of organic materials (3-1-5) [4].



The unique properties of produced radicals are:

- non-selective degradation of organic compounds,
- high oxidation potential, which allows the degradation of stable pollutants.

These properties allow using photocatalysis in many applications such as:

- decomposition of almost all organic pollutants such as toxic compounds that are present in the aquatic environment;
- removing of the air pollutants (NO<sub>x</sub>, SO<sub>x</sub> [9]) that are generated by automobiles and industries;
- decomposition of substances such as ammonia (NH<sub>3</sub>), hydrogen sulphide (H<sub>2</sub>S), methylmercaptane (CH<sub>3</sub>SH), acetaldehyde (CH<sub>3</sub>CHO) etc.
- destruction of the microbial organisms like e.g. E Coli, MRSA etc. which cause infectious diseases.

### 3.1.2. Decomposition of aqueous pollutants

Most of the pollutants in water can be mineralized at the surface of photocatalyst under the UV irradiation; these includes alkanes, haloalkanes, aliphatic alcohols, carboxylic acids, aromatics, haloaromatics, polymers, surfactants, herbicides, pesticides, and dyes [4, 10-15]. During recent decades, the photocatalytic degradation of various toxic organic compounds has been proposed, e.g. persistent pesticide pentachlorophenol (compound with persistence higher than 5 years in soil [16]) can be quite fast photodegraded using TiO<sub>2</sub> thin films (2.5 ppm of this pesticide was decomposed in less than 1 hour) [17]. In liquid-solid system, degradation reaction is influenced by many different factors such as light intensity, pH, ions, photocatalysts (its crystalline structure, surface area, defects, crystalline size, band gap energy, concentration), initial pollutant concentration, oxygen concentration etc. Often, the influence of these parameters is not the same for different pollutants. The influence of light intensity can be generalized for all pollutants, with increasing light intensity the rate of decomposition of pollutants increases. Oxygen presence is also important for the organic compounds photocatalytic degradation process. Absence of oxygen in the reaction system leads to the inhibition of most of the photodegradations. Oxygen is not only electron acceptor but also is involved in the formation of other reactive species (superoxide, hydrogen peroxide, HO<sup>•</sup> radicals). It means that constant feeding with oxygen to the photoreactor will increase the reaction rate in the comparison with system without oxygen flow. And it is necessary to mention that the photocatalytic reactions in water work best at room temperature, and thus no heating is needed. Parameters influencing the degradation of organic compound in aqueous system will be described in detail in chapter 3.3.2.

Different approaches describing the degradation mechanism of pollutant in liquid phase have been proposed in literature. The most discussed is a model describing photocatalytic reactions involving hydroxyl radical attack [18-20], but this approach cannot be applied for all photocatalytic reactions. It was found that in some cases oxidation may occur directly via photogenerated holes [21, 22]. Direct electron transfer is thermodynamically feasible since the oxidation potentials of most organic compounds lie below oxidation potential of valance band holes. Carboxylic acids, lacking abstractable hydrogens or C-C unsaturation, such as trichloroacetic acid and oxalic acid, seem to be oxidized primarily by valance band holes via a photo-Kolbe process [23]. It was documented that the initial step of photocatalytic reaction of 2,4-dichlorophenoxyacetic acid at pH 3 was done by direct hole mechanism, however, below and above pH 3, the main mechanism was HO<sup>•</sup> oxidation.

The oxidation of an organic molecule by HO<sup>•</sup> radicals is supported by following facts:

- water molecules and OH<sup>-</sup> ions are available on the surface of photocatalyst to produce HO<sup>•</sup> radicals via hole transfer;

- by the degradation of aromatic compounds, similar semi-products are formed as in radiolytic systems [24] and by Fenton-type [25] reactions, in those systems HO<sup>•</sup> radical existence was well established;
- it was proved by electron spinning resonance (ESR) spectroscopy that after irradiation of photocatalyst HO<sup>•</sup> radicals are produced [26];
- photoproduction of HO<sup>•</sup> radicals was also proved by measurements based on competition kinetics [27].

However, the different facts are in favour of the direct hole mechanism. In some cases:

- the isomer distribution and kinetics are different from expected in the presence of HO<sup>•</sup> radicals [28];
- the profile of reaction in the photocatalytic system is similar to the direct oxidation by SO<sub>4</sub><sup>-•</sup> radical or azid radical N<sub>3</sub><sup>•</sup> [24, 29];
- HO<sup>•</sup> radicals are not observed and the inhibition by HO<sup>•</sup> radicals scavenger does not work, which means that other oxidant species are involved [30, 31].

The whole reaction scheme was described by Turchi and Ollis [18] and it is shown in Table 1. According to this scheme it is obvious that the hydroxyl radical mechanism is possible only in the presence of moisture.

Table 1 Reaction scheme of photocatalytic reaction on the surface of TiO<sub>2</sub> [18]

Charge-carrier generation	$\begin{array}{c} +\dot{\iota} \\ -\dot{\iota}+h^{\dot{\iota}} \\ \text{TiO}_2 h\nu e_{\text{TiO}_2}^{\dot{\iota}} \\ \rightarrow \end{array}$	(3-1-0)
Adsorption	$\text{Ti}^{\text{IV}} + \text{H}_2\text{O} \leftrightarrow \text{Ti}^{\text{IV}} - \text{H}_2\text{O}$	(3-1-0)
	$\text{Site} + \text{R}_i \leftrightarrow \text{R}_{i,ads}$	(3-1-0)
Recombination	$\begin{array}{c} +\dot{\iota} \rightarrow \text{heat} \\ -\dot{\iota}+h^{\dot{\iota}} \\ e^{\dot{\iota}} \end{array}$	(3-1-0)
Hole trapping	$\begin{array}{c} +\dot{\iota} \leftrightarrow \text{Ti}^{\text{IV}} \vee \text{HO}^{\cdot} \\ -\dot{\iota}+h^{\dot{\iota}} \\ \text{Ti}^{\text{IV}} - \text{OH}^{\dot{\iota}} \end{array}$	(3-1-0)
	$\begin{array}{c} +\dot{\iota} \leftrightarrow \text{Ti}^{\text{IV}} \vee \text{HO}^{\cdot} + \text{H}^{\dot{\iota}} \\ \text{Ti}^{\text{IV}} - \text{H}_2\text{O} + h^{\dot{\iota}} \end{array}$	(3-1-0)
Electron trapping	$\begin{array}{c} -\dot{\iota} \leftrightarrow \text{Ti}^{\text{III}} \\ \text{Ti}^{\text{IV}} + e^{\dot{\iota}} \end{array}$	(3-1-0)
	$\text{Ti}^{\text{III}} + \text{O}_2 \xrightarrow{-\dot{\iota}} \text{Ti}^{\text{IV}} - \text{O}_2^{\dot{\iota}}$	(3-1-0)
Hydroxyl attack		(3-1-0)
Case I	$\text{Ti}^{\text{IV}} \vee \text{HO}^{\cdot} + \text{R}_{i,ads} \rightarrow \text{Ti}^{\text{IV}} + \text{R}_{j,ads}$	(3-1-0)
Case II	$\text{HO}^{\cdot} + \text{R}_{i,ads} \rightarrow \text{R}_{j,ads}$	(3-1-0)
Case III		(3-1-0)

### 3.1.3. Decomposition of gaseous pollutants

Photocatalysis can be used for cleaning of indoor and outdoor air [14]. For such an application the supply of O<sub>2</sub> and UV irradiation is sufficient to lead the reaction to complete mineralization and quantum yields of these reactions for TiO<sub>2</sub> are ranging from 1% to 100%. However, the removal of gaseous organic compound on TiO<sub>2</sub> thin films is influenced by many different parameters, which includes light intensity, substrate concentration, O<sub>2</sub> partial pressure, humidity, substrate type and so on. It was observed that the photocatalytic activity increased with increasing light intensity, the decomposition rate depends on the photon flux, being in proportion to the light intensity [32]. Another essential parameter is the presence of oxygen. The degradation rate of pollutant decomposition increased with increasing oxygen concentration [33] so the excess of oxygen should promote photocatalytic reaction. It was found that O<sub>2</sub> suppress the electron-hole recombination processes which lead to more efficient photoactivity, so the adsorbed oxygen can be considered as an effective electron trap to prevent such a recombination process [34].

As the photocatalytic reactions are typically covered by the generation of hydroxyl radicals, the presence of water vapour in the system is required for its processing as well as its adsorption on the surface of the photocatalyst. It means that the photocatalyst with higher surface area should exhibit higher photocatalytic ability to degrade the organic compounds in gas phase. In the absence of water, the photocatalytic decomposition of some chemical compounds is seriously inhibited such as the degradation of formaldehyde [35], acetone [33], toluene [36]. However, for the concentration of water vapour an optimal concentration is necessary because the excessive amount of water can also inhibit the reaction by its adsorption on the surface of photocatalyst, blocking its surface [37]. This is called “competitive adsorption” between water vapour and organic compound and it was reported for different organic compounds such as acetone [33], formaldehyde [35], ketone [38] etc.

The important fact, which was many times mentioned in literature, is deactivation and subsequent decrease in removal efficiency of gaseous pollutants [14]. There are several reasons for this deactivation. The main one is the accumulation of intermediate products or products on the surface of TiO<sub>2</sub> [39, 40]. This type of deactivation was reported for example for toluene [41], ethanol [42], and trichloroethylene [14]. Another one is that some compounds may photopolymerize on the surface, usually in the absence of water, such an example is benzene [14]. Some of these deactivation are reversible and after the deactivation it is possible to recover the photocatalyst by UV irradiation in clean humid air [43]. Recovery of photocatalyst activity was observed for deactivated photocatalyst after toluene degradation [44]. Nevertheless, some deactivations are not reversible. These irreversible deactivations are

usually observed during the removal of gaseous compounds containing heteroatoms such as S, N, P, etc. [45]. In this case, the surface of TiO<sub>2</sub> is blocked by mineral acid products and the reactivation of the photocatalyst has to be done by washing of TiO<sub>2</sub> surface by water. However, no deactivation processes were observed with different compounds for example during the degradation of ethylene [37, 46] and 1,3-butadiene [37].

#### **3.1.4. Adsorption isotherm**

A key factor in delivery of degraded molecule to the surface is adsorption on the surface, which relates to some specific interaction possibilities (e.g., chemisorption), point of zero charge and surface areas. Increasing the surface area of the photocatalysts results in increased both equilibrium and dynamic rates [47]. Adsorption is a phenomenon inducing decrease of solute concentration in solution due to the strength of attraction (Van der Waals, hydrogen bonds, electrostatic interactions etc.). The different models (Langmuir, Freundlich etc.) can be applied based on different assumptions. Adsorption equilibrium is maintained during the photocatalytic reaction. In this case the adsorption rate is faster than reaction rate of h<sup>+</sup> and e<sup>-</sup>, so the photoadsorption is not the rate-determining step.

Langmuir adsorption model [48] describes the adsorption of adsorbate onto the surface of the adsorbant and requires three assumptions:

- The surface of the adsorbant is in contact with a solution containing an adsorbate which is strongly attracted to the surface.
- The surface has a specific number of sites where the solute molecules can be adsorbed.
- The adsorption involves the attachment of only one layer of molecules to the surface, i. e. monolayer adsorption.

#### **3.1.5. Different expressions of photocatalytic activity**

The term photocatalytic activity is used for the description of photocatalyst ability to degrade model compound. The rate of photocatalytic activity (often also named as photoactivity) is mostly specified by determining the removal of model compounds in the studied system. Some researchers determine the photocatalytic activity by different methods such as: measurement of total organic carbon (TOC) [49] or chemical oxygen demand (COD) [50].

The rate of photocatalytic activity can be expressed by different ways; conversion of model compound [51], first order kinetic constant [52], reaction rate in mol.L<sup>-1</sup>.s<sup>-1</sup> [53], quantum yield [54].

The reaction rate can be more specified because it depends on different parameters of reaction system; amount of used photocatalyst [55], intensity of light, irradiated area of used layers [56] and so on. So in some publications authors included these parameters in reaction rate. Another expression of photoactivity can be the initial rate of reaction which is calculated from the initial slope of the model compound concentration dependence on time during the degradation [57].

The most precise expression of photocatalytic activity is a quantum yield of model compound reaction. Quantum yield is defined as the number of defined events which occur per photon absorbed by the system or as the amount (mol) of reactant consumed or product formed per amount of photons (mol or Einstein) absorbed.

Photochemists have routinely determined quantum yields of reactant disappearance, product formation, light emission, and of various other events occurring in some photochemical process.

The quantum yield in homogeneous photochemistry is the amount (mol) of reactant consumed or produced divided by photon absorbed by the system at a specified wavelength. The quantum yield for a photochemical reaction [58] is defined according to equations:

$$\phi = \frac{\text{amount of reactant consumed} \vee \text{product formed}}{\text{amount of photons absorbed}} \quad (3-1-0)$$

Similarly as in homogeneous photochemistry, the quantum yield in heterogeneous photocatalysis,  $\Phi$ , must express the moles of reactant consumed or product formed in the bulk phase, n, to the amount (i.e., mol or Einstein) of photons at wavelength  $\lambda$  absorbed by the photocatalyst,  $I_0$ ,

$$\phi = \frac{n}{I_0} \quad (3-1-0)$$

For some undefined reactor geometry and for polychromatic radiation, the quantum yields of photocatalytic reactions are often defined as the number of molecules converted relative to the total number of photons incident on the reactor walls.

Similarly to the quantum yield, the photonic efficiency  $\xi$  of a process is defined as a molar amount (mol) of reactant consumed or product formed per molar amount (einstein) of incident photons on the reaction system either at a given wavelength or under broadband irradiation [54].

$$\xi = \frac{N_{\text{molecules}} (\text{mol} \cdot \text{s}^{-1}) \text{transformed} \vee \text{produced}}{N_{\text{photons}} (\text{einstein} \cdot \text{s}^{-1}) \text{incident} \in \text{reaction cell}} \quad (3-1-0)$$

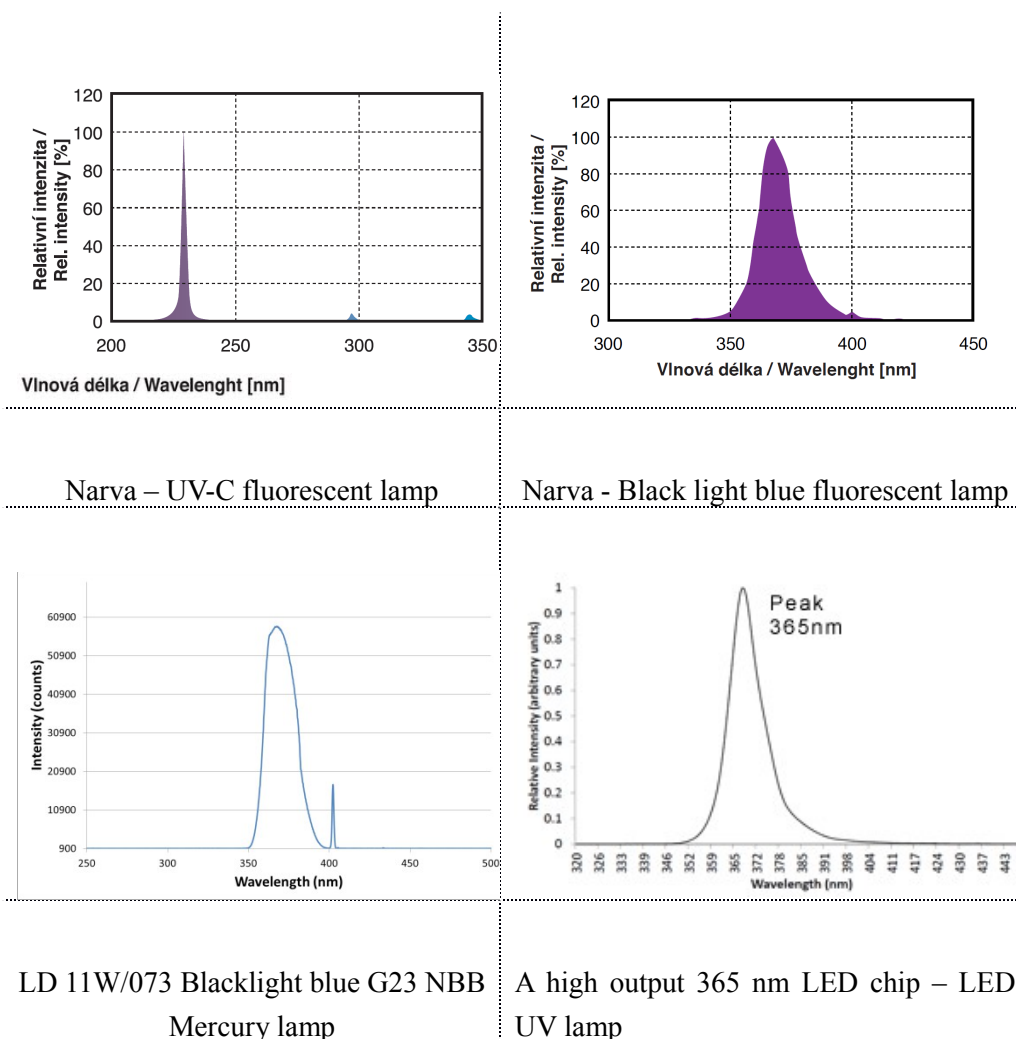
To avoid the error of usage of different reactors and light sources  $\xi_r$  relative photonic efficiency of a process given should be used.  $\xi_r$  is related to an acceptable standard process, a standard photocatalyst material [59], and a standard "secondary actinometer" in photocatalyzed processes. When the photonic efficiency obtained for the test substrate and for standard secondary actinometer are obtained under the same conditions, there is no need to measure the photon flow and thus relative photonic efficiency can be calculated by following equation:

$$\xi_r = \frac{\text{Initial rate of disappearance of reactant}}{\text{Initial rate of disappearance of secondary actinometer}} \quad (3-1-0)$$

### 3.1.6. Light sources and influence of light intensity

In studies describing efficiency of photocatalytic degradation of organic compound many different light sources are used such as Xenon lamps [60, 61]; low, medium or high pressure mercury lamps [51, 62, 63]; fluorescent lamps [64]; laser [65]; UV-light-emitting diodes [66]; or sun as the cheapest alternative [67]. But more important than the type of the light source are the intensity of the light emitted and its wavelength. In Fig. 2 emission spectra of few typical light sources of UV are shown.

Fig. 2



Emission spectra of different UV light sources

The rate of photocatalytic electron–hole formation is strongly dependent on the light intensity [68]. Thus light intensity distribution on photocatalytic reactor strongly influence degradation efficiency of pollutant decomposition [69]. The influence of light intensity on degradation rate of pollutants was described in many publications [14, 70-72]. In some cases the reaction rate exhibit a square root dependency on intensity of light [73], in other publication linear dependence was described [74, 75]. It has been found that the reaction rate

was directly proportional to radiant flux (light intensity)  $\Phi_e$  for  $\Phi_e < 25 \text{ mW.cm}^{-2}$ , above this value the rate varied as  $\Phi_e^{1/2}$  which indicates that the flux is too high and the electron-hole recombination increased. When the intensity is too high, the reaction rate started to be independent on light intensity [75].

Spectral output of used light source is another determining parameter. Reaction led under the same conditions using the different lamps emitting light at 365 nm and 254 nm with the same watt input gives the resulting quantum yield differing in one order of magnitude showing that the high energy radiation (lower wavelength) is more effective in photocatalysis [62].

### 3.1.7. Kinetics approach of photocatalytic reactions

#### 3.1.7.1. Langmuir-Hinshelwood approach

In photocatalytic (or photoadsorption) reactions, the rate dependence on reagent concentration (pressure for gases) is usually described by Langmuir–Hinshelwood (L–H) kinetic scheme which can be approximated by the equation:

$$r = \frac{-dC}{dt} = k \frac{K_{ads} C}{1 + K_{ads} C} \quad (3-1-0)$$

where  $k$  and  $K_{ads}$  are the apparent rate constants and adsorption coefficients, respectively, obtained at a given light intensity of the light at given wavelength, and  $C$  (or  $p$ ) is the reactant concentration (or pressure) [18].

The L–H mechanism is defined as the reaction of a surface-adsorbed substrate obeying a Langmuir isotherm governing the overall rate, but a reciprocal linear relation between concentration of the substrate in solution and rate of photocatalytic reaction ( $\frac{1}{r} = a \frac{1}{C} + b$ ), is not always proof of this mechanism [47]. With ongoing oxidation the surface of photocatalyst is covered with decomposed organic compound. Nevertheless, many authors express, with minor variations, the rate of photocatalytic degradation of organic compounds

on the surface of  $\text{TiO}_2$  by L–H mechanism [76]. However this cannot be taken as general approach because it do not take in account the formation of intermediates with different adsorption and reaction properties, nor presence of co-adsorbents. So the L-H approach can fail in the case of complex degradation process [64].

### 3.1.7.2. Photostationary state approach

According to the described problems with L-H approach, another general kinetics approach was proposed by Krýsa et al. [64]. Photostationary state approach provides a consistent explanation for the different reaction systems. The starting point of the photostationary model is the assumption that the primary reactive species (photogenerated holes or  $\text{HO}^\bullet$  radicals) reach an equilibrium determined by their rates of formation (by irradiation) and disappearance (by reaction with molecules in the system), and that these reactions determine the rate of degradation.

## 3.2. Photocatalysts

An ideal photocatalyst should be stable, inexpensive, non-toxic and highly photoactive. Another primary criterion for the degradation of organic compounds is that the redox potential of  $\text{H}_2\text{O}/\text{HO}^\bullet$  couple lies within the band gap of semiconductors [5]. Several semiconductors have band gap energies sufficient for catalysis of the wide range of chemical reactions. These include  $\text{TiO}_2$ ,  $\text{SrTiO}_3$ ,  $\text{WO}_3$ ,  $\alpha\text{-Fe}_2\text{O}_3$ ,  $\text{ZnO}$ , and  $\text{ZnS}$ . The position of valance and conductance bands and value of band gap energies of different semiconductors are shown in Fig. 3.

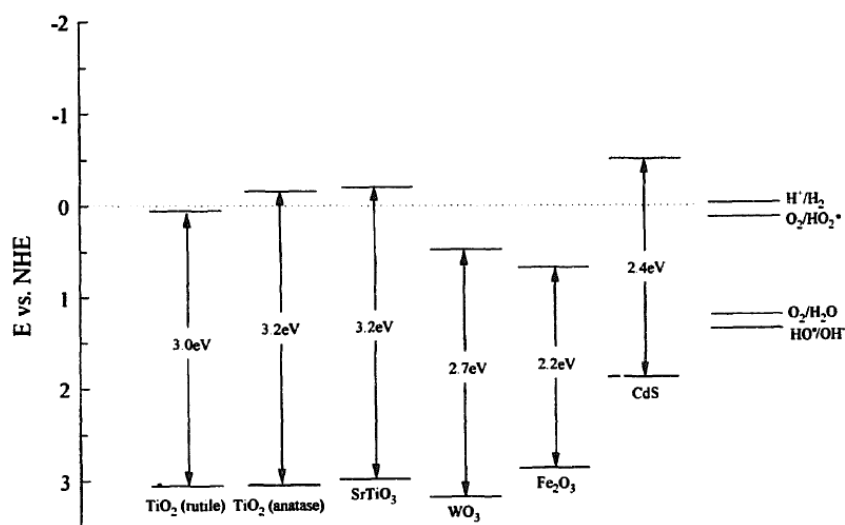


Fig. 3 Valence and conductance band positions for various semiconductors, and relevant redox couples at pH 0 [77]

TiO<sub>2</sub> seems to be the most promising material for photocatalytic degradation of organic pollutants. This semiconductor provides the best compromise between catalytic performance and stability. The anatase phase of titanium dioxide is the polymorph with the highest photocatalytic detoxification ability [78].

### 3.2.1. Titanium dioxide

Titanium dioxide (TiO<sub>2</sub>) is one of the basic materials in everyday life. It has been widely used in paints as white pigment, in cosmetics and in food industry. Generally, titanium dioxide is a semiconducting material which can be chemically activated by light. Although titanium dioxide has been known for approx. 60 years, its photocatalytic properties are still extensively investigated [5].

There are three types of crystal structures in natural titanium oxide: rutile type, anatase type and brookite type. All three are expressed using the same chemical formula (TiO<sub>2</sub>); however, their crystal structures are different. The building blocks of each modifications are shown in Fig. 4.

Titanium oxide absorbs light having an energy level higher than that of the band gap, and causes the excitation of electrons to the conduction band to create positive holes in the valence band. Despite the fact that the band gap value is 3.0 eV for the rutile type and 3.2 eV for the anatase type and 3.26 eV for the brookite, all of them absorb only ultraviolet light. The rutile type can absorb light that is slightly closer to visible-light region [79].

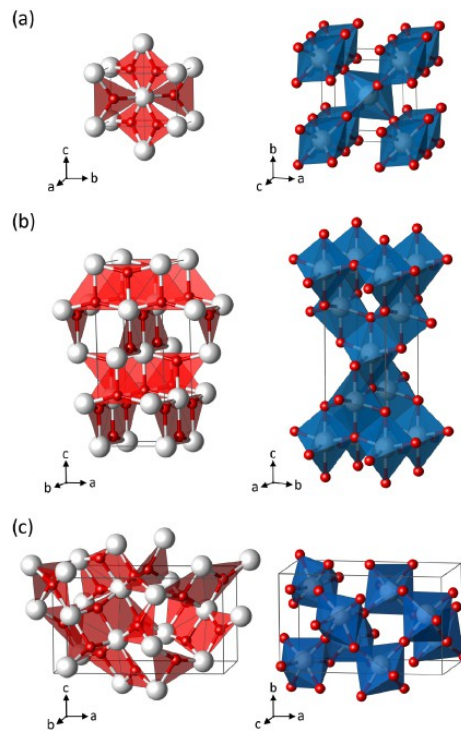


Fig. 4 Planar Ti<sub>3</sub>O building-block representation (left) and TiO<sub>6</sub> polyhedral (right) for the TiO<sub>2</sub> phases rutile (a), anatase (b) and brookite (c) (Ti (white); O (red)). [80]

As the rutile type can absorb light of a wider range, it seems logical to assume that the rutile type is more suitable to be used as a photocatalyst. In reality, the anatase type exhibits higher photocatalytic activity. One of the reasons for this is the difference in the energy structure between the two types. In both types, the position of the valence band is deep, and the resulting positive holes show sufficient oxidative power. It is known that the conduction band of anatase is placed more negatively than the conducting band of rutile. Thus, the reducing power of the anatase type is stronger than the reducing power of the rutile type [11].

Anatase titanium dioxide particles offer the highest photocatalytic activity under the UV light irradiation, but most of the anatase TiO<sub>2</sub> powders have quantum yield for most degradation processes less than 10%. Therefore, it becomes evident why novel materials have to be developed and investigated [11].

The photocatalytic efficiency of TiO<sub>2</sub> materials could be in principle increased by:

- enlarging the active surface area;
- technological optimization of known photocatalysts;

- the usage of transition or noble metal dopants (increasing possible use in visible light range [81]);
- the development and optimization of binary oxide nanostructured materials. Fu et al. proposed preparation two types of binary metal oxides:  $\text{TiO}_2/\text{SiO}_2$  and  $\text{TiO}_2/\text{ZrO}_2$ . This modification maintains the higher surface areas of the new systems even after sintering and also inhibits the anatase to rutile phase transformation [82].

Nanosized  $\text{TiO}_2$  semiconductor suspensions were found to be of high photocatalytic activity [83]. This is the reason for increased research activity in this area of photocatalysts.

### 3.2.1.1. *Nanosized $\text{TiO}_2$*

Nanosized photocatalysts are ultra small conductor particles which are a few nanometres in size. In the case of description of nanophotocatalysts, it is necessary to distinguish the term nanosized from the term nanocrystalline. Term nanosized means that the size of the whole particles is in the range of tens of nanometres but if we use the term nanocrystalline the meaning is that the particles contains crystals in the range of tens of nanometres but the particles can be in the range of hundreds of nanometres.

The interest in these small semiconductor particles originates from their unique photocatalytic properties. Some properties of nanosized particles are in fact different from those of bulk materials. Nanosized particles, with diameter ranging between 1 and 10 nm, possess properties which fall into the region of transition between the molecular and the bulk phases and they have unique photophysical and photocatalytic properties [83]. In the bulk material, the electron excited by light absorption finds a high density of states in the conduction band, where it can exist with different kinetic energies. In the case of nanoparticles, the particle size is the same or smaller than the size of the first excited state. Thus, the electron and the hole generated upon illumination cannot fit into such a particle unless they assume a state of higher kinetic energy [84].

Hence, as the size of the semiconductor particle is reduced below a critical diameter, the spatial confinement of the charge carriers within a potential well causes them to behave quantum mechanically. This means that the bands split into discrete electronic states and the nanoparticle behaves more and more like giant atom [83].

Nanosized semiconductor particles which exhibit size-dependent optical and electronic properties, so called quantum size effect, are quantized particles (Q-particles) or quantum dots [85]. In addition, nanosized semiconductors can possess enhanced photoredox behaviours, which are not possible in bulk materials [86]. As another advantage is that a fraction of atoms

located on the surface of nanoparticles is really high [83] and also these nanoparticles have also high surface area, which can improve their photocatalytic activity [87]. However, the nanosized particles have also disadvantages, as main one we can mention need for light with shorter wavelength for photocatalytic performance. That means that smaller amount of polychromatic light could be used for photocatalytic reaction.

### **3.2.1.2. *Quantum size effect***

Quantum size effect occurs when the size of the semiconductor particles becomes smaller than the Bohr radius of the first excitation state [88]. Size quantization in semiconductor particles leads to drastic changes in numerous important properties of the material.

Firstly, size quantization affects the electronic properties of the semiconductor particle, with the ultra small crystallites composed of a few molecular units maintaining their discrete highest occupied molecular orbitals and lowest unoccupied molecular orbitals.

Secondly, in the Q-size regime, the chemical and physical properties, which are related to electronic properties, strongly depend on the size of the nanoparticles [89]. The electronic properties relate to the solid state physics aspects of the particles, i.e., band structures and band gap, as well as the electrochemical positioning of the band gap edge potential with respect to the Nernst potential of the solution [88]. The band gap of the semiconductor becomes larger with decreasing particle size, and it is indicated by an absorption shift to shorter wavelengths [83]. The band edges shift to yield larger redox potentials. The levels of the valence band are moderately shifted to lower energies, while those of the conduction band are strongly shifted to higher energies.

For the absorption spectra of colloidal suspensions containing very small particles of titanium dioxide, as well as for other semiconductor materials, the exponential growth of absorbance from the specific wavelength is characteristic. For very small particles of semiconductor (nanometre size) this so-called spectral edge, compared with the same material of macroscopic dimensions, is shifted to shorter wavelengths in proportion to the reduction in particle size. The resulting spectral blue shift is one sign of the quantum size effect, which is characteristic for objects on the transition between isolated molecules and the macroscopic solid phase.

### **3.2.1.3. *Preparation of nanosized TiO<sub>2</sub>***

Many different methods for fabrication of nanosized TiO<sub>2</sub> particles were designed. The mainly investigated methods of preparation of TiO<sub>2</sub> nanostructures in liquid media are sol-gel method, sol methods, micelle and inverse micelle methods, hydrothermal and solvothermal method, and hydrolysis method.

Wide scale of nanosized TiO<sub>2</sub> has been prepared with sol-gel method, which is based on hydrolysis of a titanium molecular precursor [63, 90, 91]. This process usually proceeds by an acid-catalyzed hydrolysis of titanium(IV) alkoxide followed by condensation. When the sol-gel process is performed in the presence of tetramethylammonium, highly crystalline nanoparticles of anatase can be obtained [92]. Modification of sol-gel method is sol method. Sol method is nonhydrolytic sol-gel process. In this procedure usually titanium chloride reacts with an oxygen donor such as a metal alkoxide or an organic ether [93]. Micelles and inverse micelles (surfactants) are also commonly used for the synthesis of TiO<sub>2</sub> nanomaterials [60, 94, 95]. In these methods, the values of H<sub>2</sub>O/surfactant, H<sub>2</sub>O/titanium precursor, ammonia concentration, feed rate and reaction temperature are important in controlling size and shape of nanoparticles. However, TiO<sub>2</sub> nanoparticles prepared by this method do not show photocatalytic properties because they are often amorphous and in order to show photoactivity, it is necessary to use calcination at rather high temperature [95] or hydrothermal treatment [60] and form anatase crystalline structure. Inaba et al. [60] used reverse micelle system (or water-in-oil microemulsion) composed of water, Triton X-100 and isooctane followed by hydrothermal treatment. By this method the monodispersed TiO<sub>2</sub> nanoparticles (size, according the water content used, varied in range 5-11 nm) were prepared and their photoactivity was confirmed by the degradation of hexane. Hydrothermal and solvothermal methods are processes carried out in autoclaves under the controlled temperature and/or pressure. By the pressure control, the different size and shape of TiO<sub>2</sub> nanoparticles can be prepared [96]. In the case of hydrothermal method, the reaction is taking place in aqueous solutions [97]. Hydrothermal process used in [97] allowed the preparation of well crystallized anatase phase at quite low temperatures (80°C) with crystalline size around 8 nm. The solvothermal method is the using same principles as hydrothermal method but instead of water, nonaqueous solvents are used [51]. Supphasrirongjaroen et al. [51] used toluene as a solvent and prepared TiO<sub>2</sub> powders consisted of particles with size around 8-15 nm and their photoactivity was confirmed by degradation of ethylene. As another method, the hydrolysis of titanium chloride can be used [98-100]. Advantage of this method is that usually no organic solvents or surfactants are needed and it is possible to prepare different polymorphs of nanosized TiO<sub>2</sub> (rutile, brookite and anatase) with particle size about 5-20 nm. The photocatalytic activity of anatase prepared by this method was confirmed by the degradation of 4-CP [99].

### 3.2.1.4. Stability of colloidal suspensions

Colloidal suspension of nanoparticles can be used in many applications and in most of the cases it is necessary to keep suspension stable [101]. There are many different methods how to prevent coagulation; through the inter-particle repulsion, by increasing the viscosity of continuous phase or by creating network structure. Nanoparticles in colloidal suspension have a surface charge that attracts a thin layer of ions of opposite charge to the nanoparticle surface and forming the double layer. The electric potential at the boundary of the double layer is known as the zeta potential (Fig. 5) which is an important indicator of the stability of the colloidal system and has values that typically range from +100 mV to -100 mV.

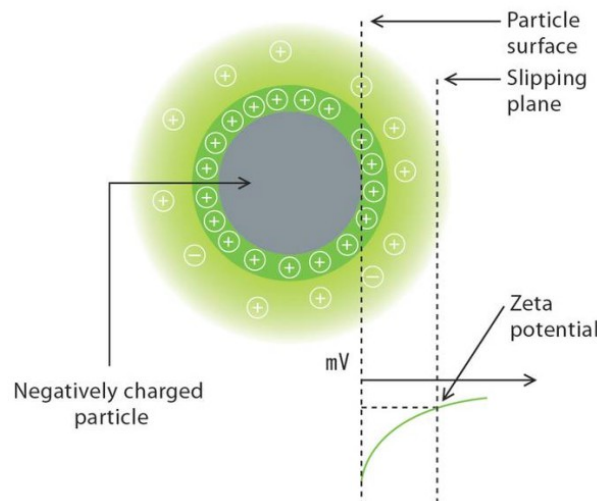


Fig. 5 The scheme of electric potential at the boundary of the double layer

The magnitude of the zeta potential is predictive of the colloidal stability. Table 2 shows the stability of colloids according to value of zeta potential [102, 103].

Table 2 Stability behaviour of the colloid according to zeta potential value

Zeta potential [mV]	Behaviour of the colloid suspension
from 0 to $\pm 5$ ,	Rapid coagulation or flocculation
from $\pm 10$ to $\pm 30$	Incipient instability
from $\pm 30$ to $\pm 40$	Moderate stability
from $\pm 40$ to $\pm 60$	Good stability
more than $\pm 61$	Excellent stability

Zeta potential is an important tool for understanding the state of the nanoparticle surface and predicting the long term stability of the nanoparticle suspensions.

### 3.2.2. Layered double hydroxides

Layered double hydroxides (LDH), also known as hydrotalcite-like compounds or anionic clays, have received much attention in the past decades due to their vast applicability. They are represented by the general formula:  $[M^{II}_{(1-x)} M^{III}_x (OH)_2] A^{n-} \cdot x/n \cdot mH_2O$ , where  $M^{II}$  includes:  $Mg^{2+}$ ,  $Co^{2+}$ ,  $Cu^{2+}$ ,  $Ni^{2+}$ ,  $Zn^{2+}$ , etc.;  $M^{III}$  may be  $Al^{3+}$ ,  $Cr^{3+}$ ,  $Ga^{3+}$ ,  $Fe^{3+}$ ; and  $A^{n-}$  might be any organic and/or inorganic anion. According to this formula, it is possible to obtain a wide variety of such compounds by changing the nature and proportions of the metallic cations in the hydroxide sheets and by intercalation of various solvated anions [104]. The LDH structure is based on  $M(OH)_6$  octahedral units sharing edges in order to build  $M(OH)_2$  brucite-like layers (Fig. 6). These  $M(OH)_6$  units contain divalent and trivalent metallic cations, the main layers are therefore positively charged.

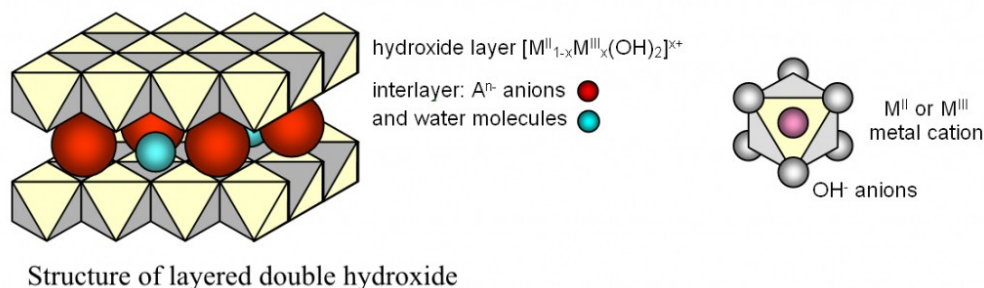


Fig. 6 Structure of layered double hydroxides

#### 3.2.2.1. Preparation of LDH

The layered double hydroxides can be prepared by different methods. The most common way of preparation is coprecipitation method. This method is based on the slow addition of a mixed solution of divalent and trivalent metals salts in adequate proportions in to the reactor containing water. A solution of alkaline compound is simultaneously added to the reactor to maintain the pH at selected value leading to the coprecipitation of both metallic salts. Another method is an induced hydrolysis, which is two step method. The trivalent metal hydroxide is

firstly precipitated by alkaline solution. The second step consists of a slow addition of this precipitate to the solution of the divalent metal salt at a constant pH. Other known method is salt-oxide method. This method was developed for the preparation of [Zn-Cr-Cl] LDH and it consists of preparation aqueous ZnO suspension and its reaction with aqueous solution of chromium chloride in excess. The reaction lasts for a few days. This method is particularly used for the preparation of [Zn-Cr-Cl], [Zn-Cr-NO<sub>3</sub>], [Zn-Al-Cl] and [Zn-Al-NO<sub>3</sub>]. These three methods are different, but the mechanism of the construction of the LDH seems to be the same [105].

As the LDH has lamellar structure based on a stacking of positive layers, which are trapping anionic species in the interlayer domains, it is highly favourable for anionic diffusion, and thus the LDH is perfect candidate for inorganic anionic exchanger. This property of LDH can be also used in order to prepare new types of LDH by anionic exchange reaction. Thermodynamically, the exchange of anions in LDH depends mainly on the electrostatic interactions between positively charged hydroxylated sheets and the exchanging anions and the free energy involved in the changes of hydration. Kinetically, the rate determination step is the diffusion of in-going anions within the interlayers [105]. The delamination process is another method for exchange of intercalated anions. This process is more difficult, since the layers are tightly bounded together. The delamination can be performed by the conversion of 2D solid into the protonic form and in this form it can further react with suitable molecule; this process is followed by restacking process to obtain final product [106]. The LDH was successfully delaminated in formamide into the transparent suspension containing sheets with average thickness of only few nanometres [107]. The delaminated LDH can be further restacked into the initial LDH structure [108], or it can be used for the preparation of new inorganic-inorganic [107] or organic-inorganic nanocomposites [109].

In some cases during the preparation by the coprecipitation method, the LDH is not obtained in well crystallized form and it is necessary to use the thermal treatment to improve the crystallinity of amorphous or badly crystallized phase. This thermal treatment is done by hydrothermal method. If the LDHs are heated in air they transform into the mixed oxides and due to their variable compositions the different composition and structures can be obtained [110, 111].

### 3.2.2.2. *Applications of LDH*

An increasing interest in the layered double hydroxides (LDH) has been developing because of their properties, which lead to the multiple applications as basic catalysts, catalyst supports, adsorbents, anion exchangers, enzyme immobilizers and medical oriented products among the others. However, the photocatalytic properties of these materials have been mostly ignored, and LDH were used only as a support of different kinds of photocatalysts. Guo et al.

[112] studied composite containing polyoxometalate (POM)  $[W_7O_{24}]^{6-}$  used for photocatalytic degradation of organic pollutants in homogeneous systems. POMs were reported as a very effective photocatalysts in homogeneous phase. In their study, they prepared  $Mg_{12}Al_6(OH)_{36}(W_7O_{24}) \cdot 4H_2O$ , and its photocatalytic activity was confirmed by the degradation of hexachlorocyclohexane. LDHs were also used as a support for nanoparticles of photocatalyst ( $TiO_2$ ,  $ZnO$ , etc.). The immobilization of nano- $ZnO$  led to increase of degradation rate of Acid Red G removal [113]. These materials are prepared to obtain a photocatalyst with bigger particles which is an important advantage of being more easily separated from the reaction system and also to enhance the adsorption of pollutant on highly adsorptive LDHs.

Recently, it was found that LDH containing Mg-Zn-Al have semiconducting properties and were able to photocatalytically degrade different organic compounds. Also as a one of the first type of LDH, photocatalytic properties of Zn-Al- $CO_3$  LDH were studied. Zn-Al- $CO_3$  LDH was prepared by coprecipitation method with the different cation ratio 1-4. This LDH was studied in noncalcined and calcined form by the degradation of the Methyl Orange and it was proved that all samples showed photocatalytic activity, which increased with increasing calcination temperature [114]. The same type of LDH was also tested by the degradation of Fast Green using noncalcined LDH. It was found that photodegradation of anionic dye was accelerated by its own photosensitization on the LDH layer [115]. Zn-Cr LDH exhibited the ability to photodegrade the Rhodamine B, Rhodamine 6G and 4-chloro 2-nitro phenol. In the work of Mohaparta [116], they proved that Zn-Cr LDH was able to photoproduce the  $HO^\bullet$  radicals. Another example of photocatalytic application of LDH is the synthesis of organic compounds. In the work of Ahmed [117], the methanol was prepared by the photocatalytic conversion of carbon dioxide using Zn-Cu- $M^{III}$  LDH, where  $M^{III}$  were Al or Ga. The selectivity of the reaction reached 68%. The photocatalytic activity of Zn-Cr LDH was also tested by the visible light photogeneration of oxygen.

By a controlled thermal decomposition of LDH containing Zn, the LDHs are transformed into mixed oxides with homogeneous interdispersion of the elements, showing high specific surface areas and high thermal stability. This method can be used for preparation of doped semiconductors, which can be further used as photocatalysts in UV and/or VIS photocatalysis [118]. In literature, thermal decomposition of Zn-Cr LDH was described [111]. It was found that during the calcination, part of  $Cr^{III}$  anions is oxidized to  $Cr^{VI}$ , when the temperature of thermal treatment is higher than 400 °C and when the temperature further exceed the temperature 750 °C, part of  $Cr^{VI}$  is again reduced to  $Cr^{III}$ . As the Zn-Cr LDH is calcined at temperature higher than 400 °C, ZnO can be detected in the structure together with spinel  $ZnCr_2O_4$ . The appearance of ZnO after the calcination can lead to the increase of photocatalytic activity as the ZnO alone is well known photocatalyst [119].

### 3.2.3. Composite materials

Usage of colloidal suspensions of TiO<sub>2</sub> is very limited. The removal of nanoparticles from reaction system is almost impossible with keeping same properties of TiO<sub>2</sub>. The preparation of TiO<sub>2</sub> nanocomposite seems to be a suitable solution of this problem.

Recently, the controlled fabrication of nanostructured materials with functional properties and its design has been an interest topic, for example the fact that the properties of nanoscale materials (optical, electrical, mechanical, chemical, etc.) are a function of the composition, size and structural order. So, it is important to create effective strategies to build tailored nanomaterials in a reliable and predictable way, in order to meet the increasing demands placed on materials synthesis and performance [120].

Colloidal particles represent attractive building blocks from which it is possible to create ordered and complex materials. In last decade, a big effort was dedicated to create core-shell colloidal composites with tailored structural, optical, and surface properties. The applicability of such colloids has stimulated the investigation of them in modern materials science, and by their technological importance, because they can be used in surface coatings, electronics, catalysis, separations, etc. [121]. The production of those core-shell particles is even an interest from fundamental and academic viewpoint, especially in the areas of colloid and interface science, as they can be used as model system to investigate factors governing colloidal interactions and stabilization and to gain valuable information on the properties of concentrated dispersions.

### 3.2.3.1. *TiO<sub>2</sub>/LDH composite*

TiO<sub>2</sub>/MgAl nanocomposites preparation was described by merely contacting LDH [122] or mechanical mixtures [10] with pre-synthesized TiO<sub>2</sub>. A special interest has been paid in recent years to the elaboration of Ti containing LDH materials as very promising materials in particular in adsorption [123], catalysis [124], photocatalysis [125] and dye-sensitized solar cells development [126]. Ti(IV)-Schiff base complex [127], Ti-Tartrate complex [125] and water soluble Ti-peroxide [128] can be intercalated in LDH structure leading to heterogeneous titanium catalysts efficient respectively in cyclohexene epoxidation, asymmetric sulfoxidation and selective oxidation of sulphide compounds. Even if it is still controversial [129], Ti(IV) salt or alkoxide can be directly coprecipitated with the other intralayer metal cations in presence of sodium hydroxide or urea as precipitant agents leading to ZnAlTi, MgAlTi, ZnTi,

NiTi, CoTi, CuTi based LDH compositions [130, 131]. Interestingly, after thermal decomposition these matrices give access to Ti based mixed oxide with specific semiconducting properties. In another approach, Carja et al. developed an elegant method to generate a TiO<sub>2</sub>/LDH nanocomposite efficient in the phenol photodegradation by reconstruction of calcined Zn-LDH phase in TiOSO<sub>4</sub> solution [132].

Indeed, further developments of nanostructured LDH based materials with tailor-made properties are allowed in using delaminated LDH suspension and the subsequent restacking of the LDH nanosheets by electrostatically derived self-assembly or layer-by-layer (LbL) process. For a long time, potential LDH delamination was considered impossible because of the unfavourable high charge density on the layers compared for instance to smectite clays. The ability to access to LDH nanosheets by delamination process was firstly highlighted by Forano and coll. [133], starting with a dodecylsulfate intercalated matrix stirred in hot butanol. Since, other procedures were described involving various LDH precursors and delamination medium. In particular, an efficient and easy-to-operate procedure involves nitrate based LDH particles and formamide as solvent [108, 134, 135]. Moreover, the presence of specific anions typically methoxide [136], lactate [137, 138], acetate [139] and formate [140] in the LDH interlayer domain favours the structure swelling and the subsequent delamination in pure water.

### 3.2.3.2. *TiO<sub>2</sub>/SiO<sub>2</sub> composite*

The synthesis of core-shell particles typically involves tailoring the surface properties of particles, often accomplished by coating or encapsulating them within a shell of a preferred material. The particle coating is carried out for a multiple reasons; for example, the shell can alter the charge, functionality, reactivity of the surface, and can enhance the stability and dispersibility of colloidal core. Depending on the coating, magnetic, optical or catalytic functions could be imparted easily to the dispersed colloidal matter. Encasing colloids in a shell of different composition may also protect the core from chemical and physical changes. The optimization of the surface characteristics of particles through coating processes is also of primary importance for the successful application of composite particles, since the controlled coating of colloids with organized layers is still a technical challenge because the particles can cause aggregation, being unusable for many purposes [120].

Concerning TiO<sub>2</sub>, fabrication of TiO<sub>2</sub>/SiO<sub>2</sub> core-shell composite photocatalyst, can improve its behaviour related to the decomposition of organic compounds in gaseous phase, since silica has excellent optical, electrical and thermal properties [141].

It has been shown that the composite exhibits photocatalytic activity for decomposition of relatively small substrates without remarkable reduction in intrinsic activity of bare TiO<sub>2</sub> [61]. These size-selective photocatalytic properties, which are different from the photocatalytic properties of the usual non-selective TiO<sub>2</sub> catalysis, will provide the composite a possible application for combination and incorporation in various organic products such as fibers or paints, since it will not react with the molecules of those products [61]. Although the composites obtained are supposed to have a tendency to decrease intrinsic photocatalytic activity of the medial TiO<sub>2</sub> (because of the silica surface coverage), the difference is negligible since the insulating nature of the porous SiO<sub>2</sub> increases surface resistance of the TiO<sub>2</sub> film and suppresses back the transfer of the photogenerated electrons to the electrolyte, in other words, it slows the recombination phenomenon [142, 143].

A variety of procedures have been employed in their fabrication, which fall into two classes: the precipitation and surface reaction [82], and the controlled deposition of preformed colloids [144].

### **3.3. Model compounds for photoactivity evaluation**

For the assessment of photocatalytic activity of photocatalysts different model compounds, which are or represent real pollutants, are used. The widespread water pollutants are dyes and pesticides. The following chapters describe the parameters influencing the degradation in aqueous phase and also the mechanism of their degradation. Important pollutants in gas phase are volatile organic compounds (VOC), therefore, those compounds are used as compounds for the determination of photoactivity in gas phase.

#### **3.3.1. Criteria for selection of model compounds**

During the decades of intensive study of photocatalysis many different compounds were used for the description of photocatalyst efficiency. However, not all of these compounds were really suitable as a model compound for such studies. The organic substances must meet certain criteria in order to be chosen as a suitable model compounds for the description of the photocatalyst activity. The criteria are:

- presence in environment;
- similarity of molecule to real pollutants;

- easy detection by available analytical methods;
- mechanism of degradation.

### 3.3.2. Parameters influencing degradation of organic compounds in liquid phase

The main operating parameters which influence the process of photocatalytic degradation of organic compounds are: pH of degraded solution, type of organic compound, oxidizing agent, photocatalyst calcination temperature, photocatalyst loading and content of dopants.

The description of pH influence on the efficiency of dye photodegradation process is a very difficult, because of its multiple roles [145]. pH is associated with the surface charge of the photocatalyst according to the following reactions:



as well as with reactant dyes and products such as acids and amines. Closely connected with adsorption is point of zero charge ( $pH_{zc}$ ) of photocatalyst. At this point, the surface charge of photocatalyst is zero which means that pH of the reaction solution can influence the adsorption of pollutants on the surface of  $TiO_2$ , which is important step for the photocatalytic oxidation, and also it can affect reactivity of positive holes and hydroxyl radicals [34]. Point zeta charge of  $TiO_2$  varies in interval of pH 4-6 depending on its structure and morphology. When  $pH > pH_{zc}$ , surface charge of  $TiO_2$  is negative and anionic dyes are adsorbed on its surface while cationic are not. Oppositely,  $pH < pH_{zc}$ ,  $TiO_2$  surface charge is positive and cationic dyes are adsorbed while anionic are not. It also has to be noted that  $TiO_2$  particles in the most of the cases agglomerates with decreasing pH (decrease to the range of pH 8-4 leads to instability of suspension [146, 147], the surface area decreases and thus the surface available for organic compound and photon adsorption also decreases.

### 3.3.3. Photodegradation of dyes

Baran et al. [148] studied the effect of UV radiation absorption of cationic and anionic dye solutions on their photocatalytic degradation in the presence of TiO<sub>2</sub> and they found that TiO<sub>2</sub> adsorbed almost only cationic dyes and simultaneously, their photocatalytic degradation is faster than that of anionic dyes. Another important fact is that the addition of oxidizing agent, such as hydrogen peroxide or ammonium persulphate, has great influence on photodegradation of dyes. It was found that the decolorization of dyes increase with increasing amount of H<sub>2</sub>O<sub>2</sub> added [149]. And the same behaviour was observed for addition of S<sub>2</sub>O<sub>8</sub><sup>2-</sup> [150]. Not only is the amount of added oxidizing agent affecting the reaction, but also the amount of photocatalyst used in reaction. The effect of photocatalyst loading on degradation of dyes was described in many studies [67, 150-152]. The most of the report shows that the optimum concentration is 0.4-0.5 g.L<sup>-1</sup> (this value is valid for most TiO<sub>2</sub> and TiO<sub>2</sub>-doped photocatalysts). When the concentration of photocatalyst increase above the optimal limit, the degradation rate does not increase but due to the interception of light, it is even decreasing [119]. Another effect of excessive photocatalyst loading can be the agglomeration of catalyst particles, hence the part of the catalyst surface become unavailable for photon absorption, and degradation rate decrease [149]. The optimum value does not depend only on the type of used dye but also on the type of used TiO<sub>2</sub> photocatalyst. Wide scale of preparation method of pure or doped TiO<sub>2</sub> exists. Dopant content has been also investigated [67, 152, 153]. Metal-TiO<sub>2</sub>-doping is always advantageous to the photocatalytic degradation of dyes, but not for the photocatalyst described in [153], where they found that transition metals TiO<sub>2</sub>-doping (Fe, Co, Cr) can be detrimental to the photocatalytic degradation of some dyes (Basic Blue 41). The calcination temperature during the catalyst preparation has significant influence on photoactivity of doped or non-doped photocatalyst [154-156]. For TiO<sub>2</sub>, calcination performed at 500°C was found in the most of the studies as an optimum temperature, with further increase of calcination temperature the transformation of anatase to rutile is promoted and thus the photocatalytic activity is decreasing.

#### *Acid Orange 7*

This anionic dye because of its huge commercial use and its easy detectability is used as a model compound for determination of photocatalytic activity [157]. Acid Orange 7 (AO7) is soluble in water and it is mainly used for silk and wool dyeing. It can be used for wool, silk and polyamide fibre fabric of direct printing, leather and paper colour, it can also be used in indicator and biological shading. It tasted can be used as a food dye, heavy metal salt used in organic pigments.

The formation of four by-products (benzene sulphonic acid, sulphanilic acid, 1,4-naphthoquinone and phthalic acid) by photocatalytic degradation of AO7 was reported by [157]. Bauer et al. [158] have identified in addition quinone and 4-hydroxybenzene sulphonic acid. Twenty-two transformation products were identified in total, including 2-naphthol, 2-hydroxy-1,4-naphthoquinone, smaller aromatic intermediates such as phthalic acid and phthalimide and aliphatic acids such as fumaric, succinic, maleic and malonic acids. The schema of photocatalytic degradation of AO7 is shown in Fig. 7.

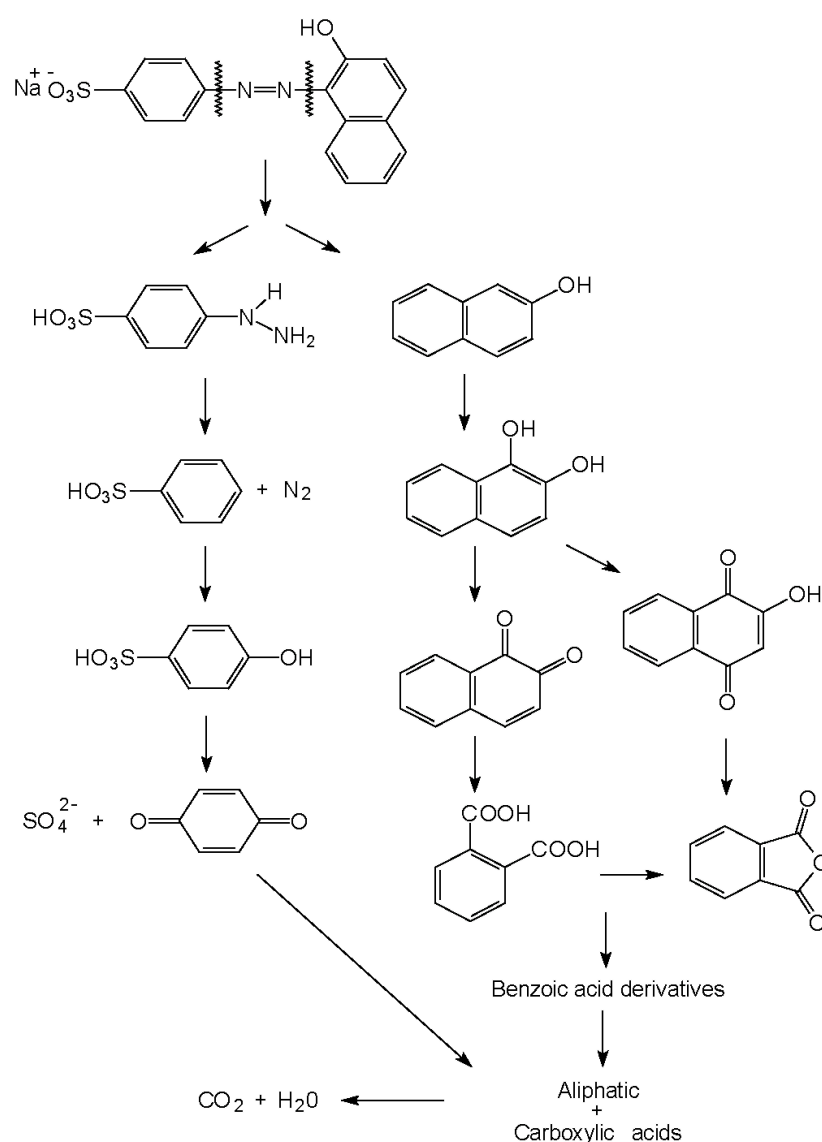


Fig. 7: Schema of photocatalytic degradation of Acid Orange 7 [145]

## *Methylene Blue*

Methylene Blue (MB) is a cationic dye and it has many uses in a range of different fields, such as biology (treatment of illnesses such as malaria and cancer) and chemistry (redox indicator, Peroxide generator etc.). MB is a compound which is also used as a standard testing molecule in ISO 10678:2010 (Determination of photocatalytic activity of surfaces in an aqueous medium by degradation of Methylene Blue) [[159](#)].

Concerning the degradation of MB, the first step of the decomposition is the cleavage of the bonds of the C-S-C followed by dissociation of the two benzenic rings. The aromatic ring then undergoes hydroxylations producing phenolic metabolites. Hydroxyhydroquinone was the last aromatic compound detected before the ring opening. The amino group can form ammonium ions, which are slowly oxidized into nitrate or can be directly oxidized into hydroxylamine leading also to nitrate. Many other hydroxylated intermediates could be formed but they are difficult to detect and the whole mechanism is not completely described. The schema of photocatalytic degradation of MB is shown in Fig. 8.

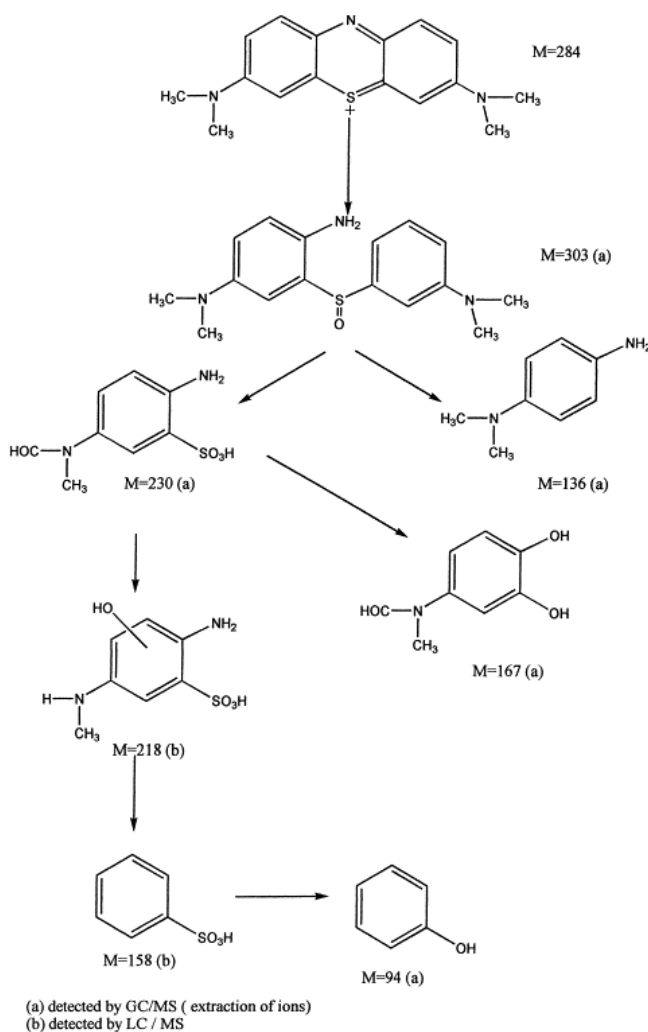


Fig. 8: Schema of photocatalytic degradation of Methylene Blue, destruction of main aromatic rings [160]

### 3.3.4. Photodegradation of pesticides

By the substituent group, the pesticides are divided to different pesticides families, organophosphates, carbamates, organohalogenes, pyrethroids and sulfonylurea pesticides. Due to the different substituents and different structures, degradation rate in the same reaction system differs for each pesticide. The influence of different halogen substituent on the photocatalytic degradation of the p-halophenols was performed by Lapertot et al. [161] They observed that the reaction rate decreases in the order as follows: p-fluorophenol  $\approx$  p-chlorophenol  $\approx$  phenol  $>$  p-bromophenol  $>$  p-iodophenol. This is related to the electron density in the aromatic ring, which varies with the halogen substituent. Another example is the pesticides containing different numbers of same substituent. In literature the example of phenol and polynitrophenols (4-NP, 2,4-DNP, 2,4,6-TNP). In the presence of either artificial

or solar light, the photocatalytic degradation of the tested compounds followed this order: 2,4,6-TNP > 2,4-DNP > 4-NP > Phenol [162].

More pesticides are better degradable at neutral or higher pH [163-166]. Addition of oxidants in all cases lead to the higher pesticide degradation rate, in the most of the cases the order of enhancement was  $UV/TiO_2/BrO_3^- > UV/TiO_2/S_2O_8^{2-} > UV/TiO_2/H_2O_2$  and the degradation efficiency increased with decreasing pH [167-169]. From the thermodynamic point of view both the additives should therefore be more efficient electron acceptors than molecular oxygen. Since the addition of bromate ions markedly enhanced the degradation of bromacil, the enhancement can be attributed to the increased number of electron involved. Another possible explanation might be a change in the reaction mechanism of the photocatalytic degradation, since the reduction of bromate ions by electrons did not lead directly to the formation of hydroxyl radicals, but rather to the formation of other reactive radicals or oxidizing reagents, e.g.  $BrO^{2-}$  and  $HBrO$ . Furthermore, bromate ions by themselves can act as oxidizing agents [168]. The deposition of metal ions on  $TiO_2$  can modify the photoconductive properties, but not in all the reported studies the effect of doping is positive [81]. Photocatalytic degradation of model pesticide 4-CP by  $TiO_2$  doped by different transition metals was tested by Kim et al. [170]. In this case the doping increased the efficiency of degradation.

#### ***4-chlorophenol***

4-chlorophenol (4-CP) is a model compound used as representative of pesticides commonly used for determination of the photocatalytic activity of the photocatalysts. Chlorophenols have been used as preservative agents for wood, paints, vegetable fibres and leather and as disinfectants. In addition, they are used as herbicides, fungicides and insecticides and as intermediates in the production of pharmaceuticals and dyes.

The degradation of 4-CP initially gives the 4-chlorodihydroxycyclohexadienyl radical, which further reacts and 4-chlorocatechol (4-CC), hydroquinone (HQ) and benzoquinone (BQ) are generated, as major intermediates. Under alkaline conditions, 4-CC is not produced in significant amounts and more hydroxylated species, such as hydroxyhydroquinone (HHQ), hydroxybenzoquinone (HBQ) and trihydroxybiphenyl (TBP) are appeared in significant amounts, in addition to HQ and BQ. Further mineralization then leads to production of HHQ, HBQ and aliphatic intermediates. The degradation of 4-chlorophenol was described for example in [171], its schema is shown on Fig. 9.

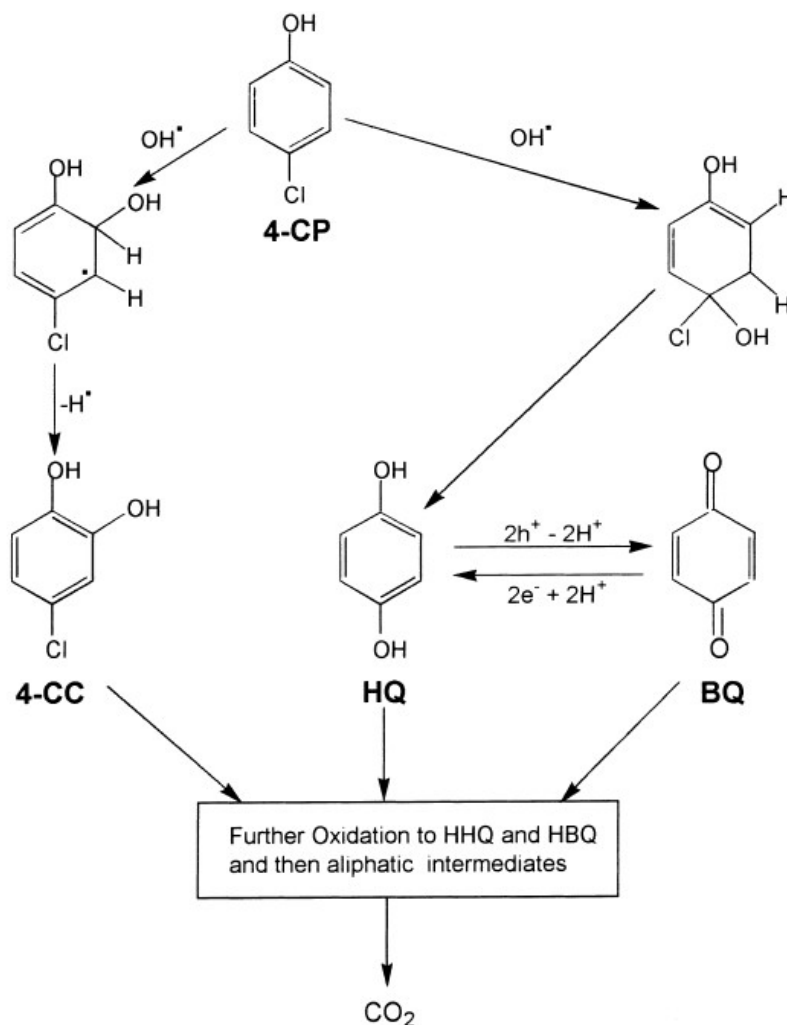


Fig. 9: Schema of photocatalytic degradation of 4-chlorophenol

### 3.3.5. Parameters influencing degradation of VOC in gas phase

Volatile organic compounds (VOC) belong to the group of the major indoor air pollutants. VOC are divided to several classes: aliphatic and cyclic hydrocarbons, aromatic hydrocarbons, aldehydes, terpenes, alcohols, esters, halocarbons, glycols, ketones, siloxanes, alkenes, organic acids, esters and others VOCs [172]. The choice of the good photocatalyst for VOC degradation depends strongly on the efficiency of electron-hole pair separation and the adsorption ability of gaseous compounds. TiO<sub>2</sub> is also commonly used photocatalyst in the case of gaseous pollutants [32, 37]. But many researchers focused on the preparation photocatalyst with improved photoactivity by the doping metal ions [14] or nitrogen [173] into TiO<sub>2</sub>, or the preparation of composite materials with adsorptive compounds (e.g. SiO<sub>2</sub> [46]), or hybrid photocatalysts (e.g. TiO<sub>2</sub> combined with ZnO [174] or activated carbon [175]). As in the case of reaction in aqueous phase, the reaction rate of VOC degradation is

also influenced by many different parameters as type and intensity of light source, pollutant concentration, humidity, and temperature.

### *Alkanes degradation*

Even though alkanes belong among the first studied gases in photocatalysis [176], they received relatively little attention in present period of time. First proposed mechanism of their degradation pointed that during the degradation partial oxidation to ketones and aldehydes occurs, rather than total oxidation [176]. But in 2001 another group [177] focused on degradation of ethane, propane, n-butane and n-hexane and they observed total oxidation and no photocatalyst deactivation for ethane and propane, and partial oxidation and carbonaceous products for n-butane and n-hexane. Later Twesme et al. [178] observed complete mineralization of alkanes (propane, n-butane isobutene) over the photocatalyst they used, which is in agreement with work of Boulamanti et al. [179].

Hexane is an important indoor and industrial air pollutant, and it was recommended as one of the eight representative indoor VOCs by a proposed ASHRAE test method for determining the effectiveness and capacity of gas-phase air filtration equipment for indoor air applications [180]. Zhang et al. [181] studied photocatalytic degradation of trace hexane in the gas phase with and without ozone addition in flow-through apparatus. They observed that relative humidity played a significant role in decomposing of hexane while using  $\text{TiO}_2/\text{UV}$  and  $\text{O}_3/\text{TiO}_2/\text{UV}$  and the reaction rate increased with increasing  $\text{O}_3$  concentration.

## 4. EXPERIMENTAL PART

### 4.1. Preparation of photocatalyst (composite) materials

#### 4.1.1. Preparation of layers from commercial TiO<sub>2</sub>

For layer preparation commercial powdered TiO<sub>2</sub> photocatalyst Aeroxide P25 (Evonic-Degussa) was used. Soda lime glasses (Marienfeld, 25 mm × 75 mm, 1 mm thickness) were used as substrates. The layers were prepared by sedimentation from suspension of known concentration (2.5 g.L<sup>-1</sup>) [57, 182]. The dried layers were calcined at 300 °C. The amount of TiO<sub>2</sub> in prepared films was 0.5 mg.cm<sup>-2</sup>. It was previously reported that for higher amounts of TiO<sub>2</sub> in the film its photoactivity do not further increase [57]. Layer with 0.5 mg TiO<sub>2</sub>.cm<sup>-2</sup> corresponds to layer thickness around 5 μm.

#### 4.1.2. Preparation of TiO<sub>2</sub> nanoparticles

The TiO<sub>2</sub> nanoparticles were prepared in the form of an aqueous suspension: 3.5 mL of pure TiCl<sub>4</sub> was added drop-wise under vigorous magnetic stirring to 900 mL of distilled water cooled to 1 °C. After 30 minutes of further slow stirring, the formed colloidal solution was dialyzed against distilled water until pH of the colloidal solution reached the value of 2.5. Then a necessary amount of distilled water was added to complete the total volume of the solution to 960 mL that corresponded to the final TiO<sub>2</sub> concentration of 33.3 mmol.dm<sup>-3</sup>. The size of prepared particles was around 7 nm [99].

The change of pH was performed in using two different alkaline reagents (KOH and NH<sub>4</sub>OH). The concentrations of KOH were 0.1, 0.2, 0.5, 1, and 2 mol.dm<sup>-3</sup>, the concentrations of NH<sub>4</sub>OH were 0.5 and 1 mol.dm<sup>-3</sup>. The defined volume of hydroxide was added to the acidic solution in one fast addition, under ultrasound. Then the solution was kept under ultrasound for 1 minute. The final pH of these solutions had value around 11. The solutions prepared from 0.2 and 1 mol.dm<sup>-3</sup> KOH, and 0.5 and 1 mol.dm<sup>-3</sup> NH<sub>4</sub>OH were used for the study [183].

#### 4.1.3. Preparation of layered double hydroxides

Mg<sub>2</sub>Al-NO<sub>3</sub> LDH phase was prepared by the coprecipitation method [108, 184]. An aqueous solution of metal salt (Mg and Al nitrate with Mg/Al = 2 and metal ion concentration of 1M)) was added dropwise to a flask containing 100 mL of deionised water. Simultaneously, a solution of NaOH (2 M) was added to maintain the pH of coprecipitation

medium at  $10.0 \pm 0.1$ . The reaction was performed under nitrogen atmosphere in order to avoid the contamination with atmospheric  $\text{CO}_2$  and under vigorous magnetic stirring to ensure the homogeneity of the reaction medium. After complete addition of the metal salt solution the slurry was aged during 12 h, washed by three dispersion/centrifugation cycles in deionised water, and finally air-dried.

A  $\text{Zn}_2\text{Cr}(\text{OH})_6\text{Cl}$  LDH phase was firstly prepared by the coprecipitation method. A  $1 \text{ mol.L}^{-1}$  mixed solution of metal chloride salts (Zn/Cr ratio of 2) was added dropwise into a reactor filled with deionized water under stirring. The pH value of the reactor solution was maintained constant at 5.5 by controlled NaOH (2M) addition. After complete addition of the salt solution, the precipitate was aged for 24 h, isolated by centrifugation, washed three times with deionized water and dried under ambient atmosphere. Then,  $[\text{Zn}_2\text{Cr}(\text{OH})_6]^+(\text{CO}_3^{2-})_{0.5}$  was obtained by anionic exchange from the  $[\text{Zn}_2\text{Cr}(\text{OH})_6]^+\text{Cl}^-$  phase. 5 g of chloride intercalated LDH solid was suspended in 500 mL of 0.1M  $\text{Na}_2\text{CO}_3$  solution and stirred for 12h. After this time, the solid was recovered by centrifugation, washed three times and air dried. Then the prepared LDH was calcined at different temperatures (300, 400, 500, 600, 800°C). The calcinations were done with temperature increase  $10^\circ\text{C}/\text{min}$ , the samples were calcined for 4 h and then left slowly cool down in furnace.

#### **4.1.4. Preparation of composite materials**

##### **4.1.4.1. *TiO<sub>2</sub>/LDH composites***

To perform the delamination of  $\text{Mg}_2\text{Al-NO}_3$  layered structure and access to a colloidal suspension, 0.1 g of LDH powder was soaked into 40 mL of formamide for 24h at room temperature [108]. Then,  $\text{TiO}_2/\text{Mg}_2\text{Al}$  nanocomposites were prepared by the mixing of the colloidal basic  $\text{TiO}_2$  solution and the  $2.5 \text{ g.L}^{-1}$  formamide suspension of  $\text{Mg}_2\text{Al-NO}_3$ . To vary the component proportions into the nanocomposite, different volumes of  $\text{TiO}_2$  were involved in the reaction. Typically, 65 mL, 21.5 mL or 5.4 mL of  $\text{TiO}_2$  were added to the delaminated LDH suspension, corresponding respectively to a theoretical LDH/ $\text{TiO}_2$  mass ratio of 1.5, 0.5 and 0.125, noted hereafter as  $\text{TiO}_2/(\text{Mg}_2\text{Al})_{1.5}$ ,  $\text{TiO}_2/(\text{Mg}_2\text{Al})_{0.5}$  and  $\text{TiO}_2/(\text{Mg}_2\text{Al})_{0.125}$ . Then, the mixture was left to stand for three days and centrifuged at 10 000 rpm for 15 min. The slurry was washed twice with 100 mL of distilled water and left to dry at room temperature.

##### **4.1.4.2. *TiO<sub>2</sub>/SiO<sub>2</sub> composites – colloidal suspensions***

Composites were prepared by mixing of stable one year old TiO<sub>2</sub> colloidal suspension (c = 2.661 g.L<sup>-1</sup>, preparation described in chapter 4.1.1) and SiO<sub>2</sub> colloidal suspension (the concentration of SiO<sub>2</sub> was set to achieve the ratio between TiO<sub>2</sub> and SiO<sub>2</sub> – 1:1; 1:5; and 1:10 while using the same volume of the solution). 30 mL of TiO<sub>2</sub> were added to 30 mL of SiO<sub>2</sub> solution (concentration 2.66, 13.3, or 26.6 g.L<sup>-1</sup>) under ultrasound. pH of solution was modified by adding HCl or NH<sub>4</sub>OH solution.

#### **4.1.4.3. TiO<sub>2</sub>/SiO<sub>2</sub> composites – powders**

TiO<sub>2</sub>/SiO<sub>2</sub> powders were prepared from freshly prepared TiO<sub>2</sub> suspension prepared by following way. TiO<sub>2</sub> suspension was prepared by dropwise addition of 10 mL of TiCl<sub>4</sub> to 180 mL of distilled water under the fast stirring at room temperature. After the addition the colloid suspension was left stirred for 1 hour. The concentration of prepared suspension was 0.5 mol.l<sup>-1</sup> and this suspension for further used for the composite material preparation. To prepare the composite two different methods were used:

- The first method was heterocoagulation by direct mixing of TiO<sub>2</sub> and SiO<sub>2</sub> suspension in ratios 1:1 and 1:10 (by weight) under the fast stirring (samples marked as D).
- Second method was based on the addition of TiO<sub>2</sub> powder to the suspension of SiO<sub>2</sub>. TiO<sub>2</sub> powder was prepared by coagulation of prepared TiO<sub>2</sub> suspension by addition of 20 mL of 3 M NaOH to 50 mL of TiO<sub>2</sub>. Prepared powder was then mixed under the fast stirring with SiO<sub>2</sub> suspension in ratios 1:1 and 1:10 (samples marked as P<sub>0</sub>). Second synthesis was performed with additional washing – before coagulation of composites, TiO<sub>2</sub> aggregates were centrifuged and 2 times washed with distilled water and dried at 60°C. Then again was mixed with SiO<sub>2</sub> suspension in ratios 1:1 and 1:10 (samples marked as P).

Composite suspensions were then centrifuged; four times washed with distilled water and dried at 60°C.

The layers were prepared by sedimentation from suspension of known amount of powder composite on the glass plate (14.9 x 18 cm). The layers were dried at room temperature. The amount of TiO<sub>2</sub> in prepared films was for all composites kept at 0.5 mg.cm<sup>-2</sup>.

## **4.2. Characterization methods**

#### **4.2.1. Particle size and zeta potential measurement**

Measurement of the particle size and zeta potential are performed on a Zetasizer Nano ZS (Malvern Instruments) working on the principle of dynamic light scattering [185]. The particle size of TiO<sub>2</sub> particles in suspensions was measured after different time periods and at different pH values. The standard deviation of the measured particle size in the range 5-50 nm was  $\pm 0.6$  nm.

#### **4.2.2. X-ray diffraction and fluorescence**

The powders were analysed by powder X-Ray diffraction (PXRD) using an X'Pert Pro Philips diffractometer with diffracted beam graphite monochromator using a Cu K $\alpha$  radiation source equipped with X'Pert HighScore Plus. Diffractograms were recorded in the  $2\theta$  range of 15-70° with a step of 0.013 ° and a counting time per step of 20 s.

X-ray fluorescence analysis were performed using XRF spectrometer ARL 9400 XP (THERMO ARL, Switzerland) equipped with Rh lamp, 4kW generator, 4 collimators, 6 crystals (AX 20, TLAP, PET, Ge 111, LiF 200, LiF 220), and 2 detectors – proportional and scintillation. Data were analysed by software UNIQUANT 4.

#### **4.2.3. FT-IR and Raman spectroscopy**

Attenuated Total Reflectance Fourier Transform infrared (FT-IR) spectra were measured in the range 400-4000 cm<sup>-1</sup> on a FTIR Nicolet 5700 spectrometer (Thermo Electron Corporation) equipped with a Smart Orbit accessory. Raman spectra were recorded at room temperature in air using a 514 nm laser line of an Ar<sup>+</sup>/Kr<sup>+</sup> laser and a JOBIN YVON T64000 triple spectrometer, equipped with an Olympus confocal microscope using a 50 magnifications and nitrogen-cooled CCD detector. Low-frequency Raman measurement were performed in backscattering geometry. Wavelength of the excitation source was 514.5 nm. Power of the excitation beam was fixed at 200 mW. Spectra were acquired (2 x 600 s) in the frequency range from 50 to 600 cm<sup>-1</sup> and 200 to 1800 cm<sup>-1</sup> using respectively a triple and single detector configuration.

Raman spectra were recorded at room temperature in air using a 514 nm laser line of an Ar<sup>+</sup>/Kr<sup>+</sup> laser and a JOBIN YVON T64000 triple spectrometer, equipped with an Olympus confocal microscope using x50 magnification and a nitrogen-cooled CCD detector. Low-frequency Raman measurement was performed in backscattering geometry. The wavelength of the excitation source was 514.5 nm. The power of the excitation beam was fixed at 200 mW. Spectra were acquired (2 x 600 s) in the frequency range 50 to 600 cm<sup>-1</sup> and 200 to 1800 cm<sup>-1</sup> using a triple and single detector configuration, respectively. Profile analysis of the Raman bands was performed using a Lorentzian function.

#### **4.2.4. Electron microscopy (FESEM, HRTEM, XPS)**

Field Emission Scanning Electron Microscopy (FESEM) characteristics of the samples were imaged by a Zeiss supra 55 FEG-VP operating at 3 keV. This apparatus was equipped with silicon drifted detector (SSD) Energy Dispersive X-ray Spectroscopy (EDS) for the elemental analysis. Specimens were mounted on conductive carbon adhesive tabs and imaged after gold sputter coating to make them conductive. High-resolution transmission electron microscopy (HRTEM) images were taken using a JEOL JEM- 2100F microscope operated at 200 kV and coupled with an energy X-Ray spectrometer (EDS). X-ray photoelectron spectroscopy (XPS) spectra of TiO<sub>2</sub>/(Mg<sub>2</sub>Al)<sub>1.5</sub> compound are collected using a Katros Axis Ultra DLD spectrometer, equipped with a standard Al K $\alpha$  excitation source (1486.6 eV). The binding energy (BE) was calibrated by measuring C 1s peak from the surface contamination at 285.1 eV. Samples were dispersed in ethanol and then one droplet of the suspension was applied to a 400 mesh holey carbon-coated copper grid and left to dry in air.

#### **4.2.5. Surface area measurement**

Nitrogen adsorption-desorption were performed at -196 °C with a Micromeritics ASAP 2020. Before analysis, samples were pre-treated at 80 °C under vacuum for 12 h. The surface areas were estimated using the Brunauer-Emmett-Teller method (BET).

#### **4.2.6. Thermogravimetry analysis**

Thermogravimetric analysis (TGA) and Differential thermal analysis (DTA) were performed on a Setaram TG-DTA 92 instrument in the temperature range of 25-1000 °C, with a heating rate of 5 °C/min.

#### 4.2.7. UV-VIS absorption spectroscopy and band gap energy determination

The measurement of UV-VIS spectra (in the range 200 to 800 nm) was performed on a Varian Cary 100 Scanning UV-VIS Spectrophotometer and a Perkin-Elmer Lambda 19.

In this work, the average band gap energies were determined on the basis of the absorption spectra of very small colloidal suspensions of semiconductor particles using a procedure described in the literature [186]. The original coordinates of the spectra (absorbance vs. wavelength) were transformed to Kubelka-Munk function (K) vs. photon energy (hv). The final plots of  $(K/h\nu)^{1/2}$  as a function of hv are in accordance with the theoretical equation [187],

$$h\nu\alpha = \text{const}^2 (h\nu - E_{bg}) \quad (4-2-0)$$

where  $\alpha$  is the absorption coefficient of the photocatalyst and  $E_{bg}$  the energy band gap. (The Kubelka-Munk function K calculated from the reflectance spectra is predetermined to be directly proportional to the absorption coefficient  $\alpha$ .) The values of the energy band gap are usually estimated by extrapolation of the linear part of the dependence.

#### 4.2.8. Measurement of AO7 adsorption on ZnCr-LDH

AO7 sorption experiments were carried out using a batch method at a controlled temperature. Typically 10 mg of sample in 8 mL of distilled water was stirred over night at constant temperature 20°C. Then the calculated volume of AO7 concentrated solution was added to obtain the desired concentration. The pH of solution was fixed at  $7.0 \pm 0.5$  and the distilled water was added to obtain the final volume of 10 mL. The suspensions were stirred at a constant speed for 12h and centrifuged at 4500 rpm. Dye concentration was estimated spectrophotometrically by monitoring the absorbance at 482 nm. The amount of AO7 adsorbed by the clays,  $q_e$ , was determined from the difference between the initial ( $C_i$ ) and equilibrium ( $C_e$ ) concentrations of the dye per gram of LDH:

$$q_e = \frac{(C_i - C_e)V}{m} \quad (4-2-0)$$

The adsorption isotherms were obtained by plotting  $q_e$  versus  $C_e$ .

### 4.3. Photocatalytical measurements

#### 4.3.1. Photodegradation in aqueous media, system for the test of suitability of model compounds

Photoactivity of prepared layers was measured in the set of four batch reactors. Each reactor is made of glass which transmits light of wavelengths higher than 330 nm. Mixing of model compound solution (25 mL) in each photoreactor is ensured by magnetic stirrer. Temperature of the solution was kept at 20 °C by circular thermostat. Samples with TiO<sub>2</sub> layers are fixed in the cup of the reactor. The schema of one batch reactor is shown in Fig. 10. As a light source two 11 W fluorescent lamps were used. Sylvania Lynx-S BLB, with broad maximum at 365 nm and Sylvania Lynx S BL350 with broad maximum at 355 nm and small irradiation in visible region. UV/Vis absorption spectroscopy was performed using a Cecil Instruments CE 2021 UV/Vis spectrophotometer. HPLC analysis was carried out using a Shimadzu chromatographic system with LC-10ADvp pump and SPD-M10Avp diode array detector (wavelength range of 200-800 nm). A mobile phase methanol/water (50:50, v/v) with a flow rate 1 ml min<sup>-1</sup> and LiChrospher 100 RP-18 column (type LiChroCART 125-4, Merck, Germany) was used.

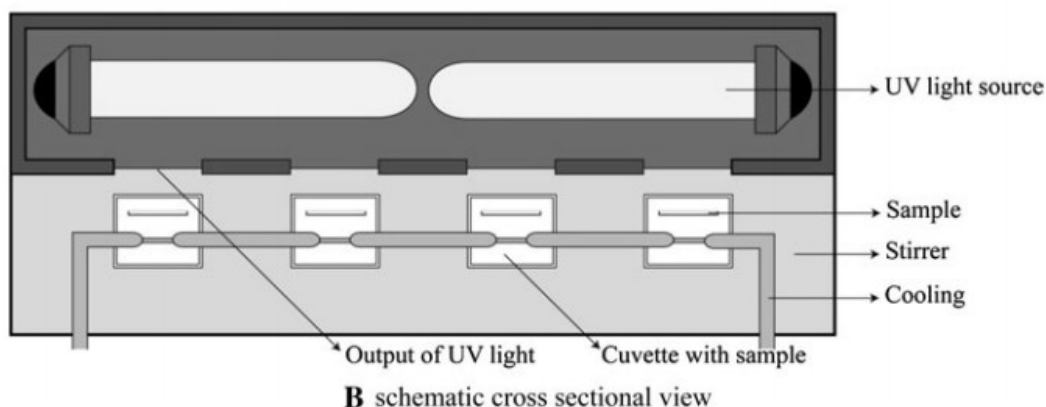


Fig. 10 The schema of batch photoreactor for determination of photoactivity of thin films – cross sectional view

#### 4.3.2. Photodegradation of model compounds in aqueous media, system for the evaluation of synthesized photocatalysts

The photocatalytic efficiency of prepared photocatalysts were studied using 4-chlorophenol (4-CP), Acid Orange 7 (AO7) and Methylene Blue (MB) as model compounds. The

concentration of the pollutant involved in the reaction was  $5 \cdot 10^{-5} \text{ mol} \cdot \text{L}^{-1}$  while the amount of photocatalyst was calculated to correspond to a fixed  $\text{TiO}_2$  concentration of  $0.5 \text{ g} \cdot \text{L}^{-1}$  or fixed concentration of  $0.5 \text{ g} \cdot \text{L}^{-1}$  of LDH in the case of ZnCr-LDH, if it is not mentioned differently. The temperature during the measurement was kept at  $15 \text{ }^\circ\text{C}$ . The irradiation setup consisting of an elliptical stainless steel container, was used for both kinetic and analytical experiments. A high-pressure mercury lamp (Philips HPW type 125 W) was located at a focal axis of the elliptical cylinder. An inner filter permits to select a main emission at 365 nm (93%). A water-jacketed Pyrex tube (diameter = 1.8 cm) was used as reactor and centred at the other focal axis. The solution was continuously stirred using a magnetic stirrer. The schema of the apparatus is shown in Fig. 11. Method of the analytical determination of 4-CP and AO7 are in detail described in chapter 5.1.1. The disappearance of 4-chlorophenol and the formation of the by-products were followed by high performance liquid chromatography using a Waters 2695 HPLC chromatograph system equipped with a Waters 2998 photodiode array detector, while the AO7 and MB disappearance was directly measured by UV-Vis spectroscopy (Varian Cary 100 Scanning UV-VIS Spectrophotometer).

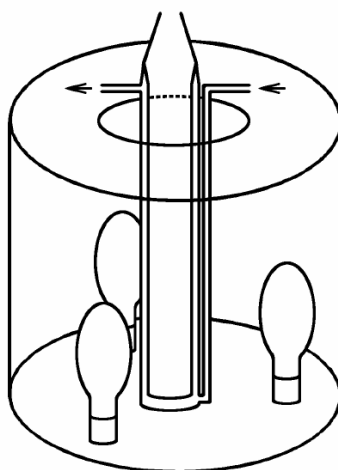


Fig. 11 Schema of batch photoreactor

#### 4.3.3. Photodegradation of model compound in gaseous media

The photocatalytic activity of prepared  $\text{SiO}_2/\text{TiO}_2$  composite films was tested in a flow through apparatus, which includes a reactor with a source of UV radiation. Three 11 W lamps Sylvania BLB with emission maximum at 367 nm were used as external UV sources; the average light intensity was  $2 \text{ mW} \cdot \text{cm}^{-2}$ . The reactor was supplied with a calibration gas (499 ppm of hexane in  $\text{N}_2$ ) diluted by technical air so that the initial concentration of hexane was 4 ppm. The flow of technical air on inlet of apparatus was  $1 \text{ L} \cdot \text{min}^{-1}$  and the flow of

calibration gas was  $8 \text{ mL}\cdot\text{min}^{-1}$ . The schema of the apparatus is shown in Fig. 12 and schema of photoreactor part is in Fig. 13.

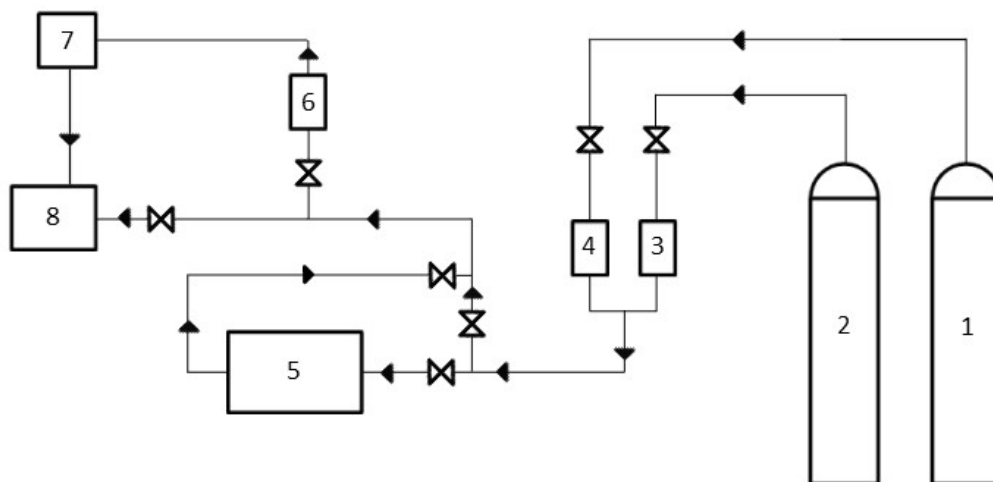


Fig. 12 The schema of flow through apparatus for gas pollutants degradation; 1 – hexane in  $N_2$ , 2 – air, 3 and 4 – mass flow meter, 5 – reactor, 6 – sampling pump, 7 – GC-FID, 8 – outlet

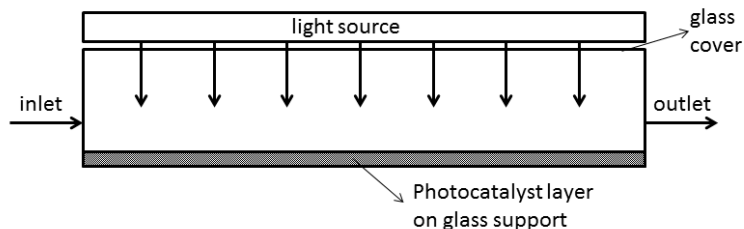


Fig. 13 The schema of cross section of photoreactor for gas pollutants degradation (length 18 cm and width 15 cm)

The degradation process was divided into four steps:

1. **Bypass of the reactor:** The flow of the model compound mixed with air bypasses the reactor, thus it is not influenced by the photocatalyst.
2. **Reactor UV lights OFF:** The model compound goes through the reactor but with the UV light turned off. Model compound is in contact with the layer.

3. **Reactor UV lights ON:** The model compound goes through the reactor with the UV lights turned on. Model compound is in contact with the layer.
4. **Reactor UV lights OFF:** The flow goes again through the reactor with the UV light turned off.

Concentration of individual pollutants and possible intermediates was determined by gas chromatograph Varian CP-3800 with capillary column CP-Sil 5 CB 15 × 0.25 (0.25) and flame ionization detector.

#### 4.3.4. HO<sup>•</sup> radical photoproduction rate measurement

To measure the photoproduction rate of HO<sup>•</sup> by LDH photocatalyst, terephthalic acid (TA) was used [188]. TA is oxidized by HO<sup>•</sup> radicals to 2-hydroxyterephthalic acid (TAOH) which is then analysed. Reaction of TA with HO<sup>•</sup> radical is shown in Fig. 14. 3 mL of TA solution ( $c=5 \times 10^{-5} \text{ mol.L}^{-1}$ ) were irradiated in a stirred quartz cuvette under monochromatic light of different wavelengths (296, 313, 340, 365, 380, 400 and 450 nm) by monochromator equipped with a Xe 1000 W lamp (ORIEL) at room temperature. The concentration of photocatalyst was kept constant at  $c = 0.5 \text{ g.L}^{-1}$ . At fixed times during irradiation, the cuvette was removed and the suspension was centrifuged to remove the photocatalyst from the system, filtrate was then transferred into measurement cuvette and the concentration of 2-hydroxyterephthalic acid (TAOH) using Perkin-Elmer MPF 3 L spectrofluorimeter was evaluated. The formation of HO<sup>•</sup> was calculated from the determined concentration of TAOH (fluorescence of TAOH -  $\lambda_{\text{exc}} = 320 \text{ nm}$ ,  $\lambda_{\text{em}} = 420 \text{ nm}$ ).

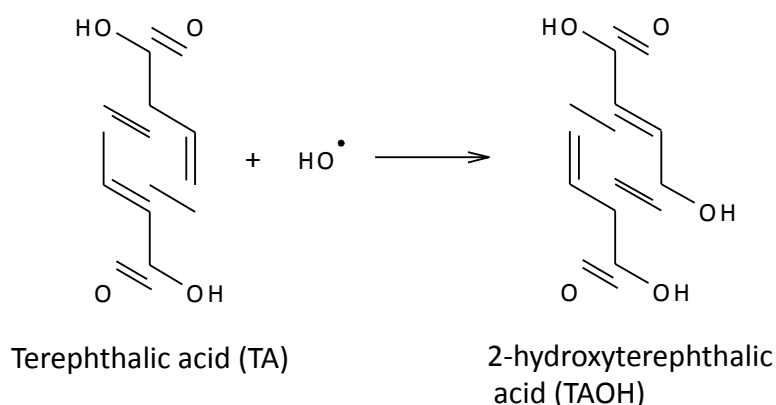
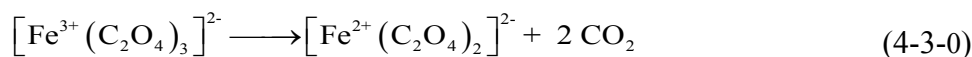
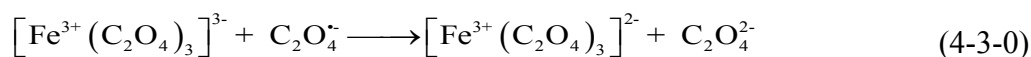
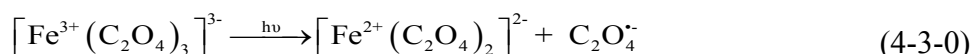


Fig. 14 Reaction of terephthalic acid with HO<sup>•</sup>

### 4.3.5. Liquid-Phase Actinometry Using Potassium Ferrioxalate

The light intensity  $I_0$  was measured by ferrioxalate potassium ( $K_3Fe(C_2O_4)_3$ ) actinometry developed by Parker and Hatchard [189]. It is very sensitive over wide range of wavelengths, and it is very simple to use. This method depends on the photochemical reactivity of ( $K_3Fe(C_2O_4)_3$ ) in the acidic solution. Under irradiation,  $Fe^{3+}$  was reduced to  $Fe^{2+}$  and oxalate ion was oxidized to  $CO_2$ . The reactions of reduction are:



The produced ferrous ion and its oxalate complex in these solutions do not absorb the incident radiation measurably during the photolysis, but after the exposure the ferrous ion is made to be highly absorbing and easy to be analysed by formation of red-coloured 1,10-phenanthroline- $Fe^{2+}$  complex. The  $Fe^{2+}$  concentration was determined by complexometry.

To determine the light intensity in a photochemical reaction cell, the ferrioxalate solution of the appropriate concentration ( $0.006 \text{ mol.L}^{-1}$ ) is added to the cell of volume  $V_1$  and length  $l_{irr}$ , and then irradiated for the time  $t$ . After irradiation we took 2 ml ( $V_2$ ) of irradiated solution, then added 1 ml of acetate buffer, and 0.5 ml of 1,10-phenanthroline. Solution was then filled with distilled water to volume 5 ml ( $V_3$ ). After mixing, the solution was kept in the dark for 1 h and then UV-VIS measurement was carried out at 510 nm (absorption maximum,  $\epsilon_{510} = 1.118 \times 10^2 \text{ dm}^3 \cdot \text{mol}^{-1} \cdot \text{cm}^{-1}$ ) in a cell with optical path ( $l_{510} = 2 \text{ cm}$ ). Then an identical but unirradiated solution was prepared for use as the blank. From these data, we can calculate the number of ions of  $Fe^{2+}$  formed during the photolysis by using following formula:

$$n_{Fe^{2+}} = \frac{N_A \cdot V_1 \cdot V_3 \cdot \log_{10}(I_0/I)}{V_2 \cdot l_{510} \cdot \epsilon_{510}} = \frac{6.023 \cdot 10^{23} \cdot V_1 \cdot V_3 \cdot OD_{510}}{V_2 \cdot l_{510} \cdot \epsilon_{510}} \quad (4-3-0)$$

where  $OD_{510} = (OD_{solution} - OD_{blank})$  (4-3-0)

and  $N_A$  is Avogadro constant ( $N_A = 6.023 \cdot 10^{23} \text{ mol}^{-1}$ ) and  $\epsilon_{510}$  is extinction coefficient at 510 nm ( $1.118 \times 10^2 \text{ dm}^3 \cdot \text{mol}^{-1} \cdot \text{cm}^{-1}$ ).  $OD_{solution}$  is the value of absorbance of irradiated solution at 510 nm and  $OD_{blank}$  is value of absorbance of blank sample.

The photon flux  $I_0$  can be calculated as follows [190]. The number of  $Fe^{2+}$  formed is proportional to the fraction of absorbed light by the solution during time  $t$ . So photon flux emitted by this system,  $I_0$ , expressed in photon per second for volume  $V_1$  ( $\text{photon} \cdot \text{s}^{-1}$ ), is equal to:

$$I_0 = \frac{n_{Fe^{2+}}}{\phi_{Fe^{2+}} \cdot t \cdot (1 - 10^{-OD})} \quad (4-3-0)$$

where  $(1 - 10^{-OD})$  is the percentage of photons absorbed by the solution at the wavelength 510 nm at time zero.

Then:

$$I_0 = \frac{6.023 \cdot 10^{23} \cdot V_1 \cdot V_3 \cdot OD_{510}}{V_2 \cdot l_{510} \cdot \epsilon_{510} \cdot \phi_{Fe^{2+}} \cdot t \cdot (1 - 10^{-OD})} \quad (4-3-0)$$

The photon flux intensity,  $J_{hv}$ , ( $\text{photons} \cdot \text{s}^{-1} \cdot \text{cm}^{-2}$ ) can be obtained as follows:

$$J_{hv} = \frac{I_0}{A} = \frac{6.023 \cdot 10^{23} \cdot l_{irr} \cdot V_3 \cdot OD_{510}}{V_2 \cdot l_{510} \cdot \epsilon_{510} \cdot \phi_{Fe^{2+}} \cdot t \cdot (1 - 10^{-OD})} \quad (4-3-0)$$

$V_1$  can be expressed:

$$V_1 = l_{irr} \cdot A \quad (4-3-0)$$

where  $l_{irr}$  is the length of optical path of the cell,  $V_1$  is the volume of the cell and  $A$  is irradiated geometrical area.

#### 4.3.6. Measurement of quantum yield of 4-CP photocatalytic degradation

The quantum yield represents the photocatalytic activity of a photocatalyst. This measurement reflects the efficiency of the photochemical process. In terms of photochemistry, it is very important to control the change in quantum yield during aging of the nanoparticles. In our case we measured the quantum yields of photocatalytic degradation of 4-chlorophenol. These measurements were performed in 2 cm (path length -  $l_{irr}$ ) cylindrical quartz cells. The light source was a high-pressure mercury lamp (Osram HBO 1000W) equipped with monochromator (Jobin Yvon). The monochromatic irradiations were carried out at a wavelength of 365 nm. The intensity of the light source was measured by actinometry ( $2.18 \times 10^{14}$  photons. $s^{-1}$ . $cm^{-2}$ ). Quantum yields were calculated by the equation (4-5-37) reported previously [16].

$$\Phi = \frac{\frac{\Delta C}{\Delta t} \cdot 6.023 \cdot 10^{20} \cdot l_{irr} \cdot A}{I_0 \cdot (1 - 10^{-OD_{\lambda_{irr}}})} \quad (4-5-0)$$

where  $(1 - 10^{-OD_{\lambda_{irr}}})$  represents the percentage of light absorbed by the solution when  $t = 0$ ,  $I_0$  is the intensity of the light source (determined by actinometry),  $\lambda_{irr}$  is the irradiation wavelength,  $\Delta C$  is the change in concentration with time in  $mol.L^{-1}$ , and  $l_{irr}$  is the length of the irradiation cell in cm.

The change in concentration of the 4-chlorophenol during the measurement of quantum yield was measured by high-performance liquid chromatography (HPLC), the starting 4-CP concentration being  $10^{-4}$   $mol.L^{-1}$ . The measurement was performed on an Alliance<sup>®</sup> HPLC

System chromatograph. The flow rate was  $1 \text{ mL}\cdot\text{min}^{-1}$  and the eluent was a mixture of pure water and methanol (50/50, v/v). The column used was a Lichrosphere (Merck) RP18 (reverse phase) of  $125 \text{ mm} \times 4.6 \text{ mm}$  with a particle diameter of  $5 \text{ }\mu\text{m}$  and a pore diameter of  $100 \text{ \AA}$ . Every sample was injected a minimum of two times and the obtained error was less than 10%.

## 5. RESULTS AND DISCUSSION

### 5.1. Photocatalytic evaluation of TiO<sub>2</sub> photocatalysts using model compounds

In this chapter, the applicability of two commonly used model compounds (AO7 and 4-CP) for the determination of photocatalytic activity (as described in chapter 3.3.1) will be studied. Particular interest will be given to the influence of initial concentration and mass transfer on the degradation rate.

#### 5.1.1. Using of UV-VIS spectroscopy to determine 4-CP and AO7 concentration

4-CP absorbs light in the UV region below 300 nm, the 4-CP absorption spectrum is shown in Fig. 15, but the primary products of its degradation (hydroquinone, benzoquinone and 4-chlorocatechol) absorb in a similar wavelengths region [64]. That means that UV spectroscopy gives higher values for the concentration of 4-CP due to the presence of absorbing intermediates, indicating that UV spectrophotometry can be used only for rough estimate of 4-CP concentration during its photocatalytic degradation but for its precise determination, analysis by HPLC is necessary.

AO7 has absorption band with a maximum at 485 nm and absorption minimum at irradiation wavelengths around 350 nm. Therefore, AO7 absorbs only a small part of the emitted radiation while the majority of it is absorbed by the photocatalyst. The absorption spectrum of AO7 is shown in Fig. 15.

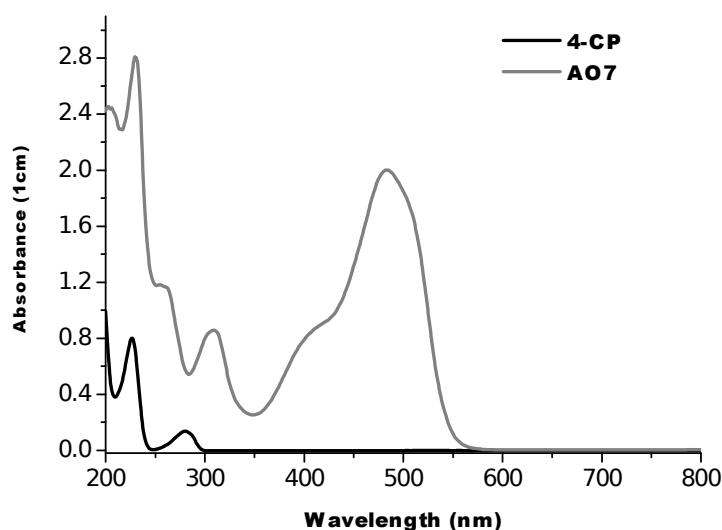


Fig. 15 Absorption spectra of 4-CP and AO7, concentration  $10^{-4}$  mol.L<sup>-1</sup>

Using AO7 as a model compound has a main advantage in the simple measurement of its concentration by visible absorption spectrophotometry. There are only few papers reporting the use of HPLC for monitoring the photocatalytic destruction of AO7 and its intermediates [191, 192]. However, since the photocatalytic degradation of the azo dye most likely involves cleavage of the azo bond in the first step [191], i.e. the production of largely colourless intermediates, such degradation intermediates should not interfere with the measurement of AO7 concentration via visible absorption spectroscopy.

To illustrate the above point, we compared the time course of absorbance at 485 nm during a typical photocatalytic destruction of AO7 with that of the concentration of AO7 as determined by HPLC (Fig. 16) under the same conditions. The excellent agreement of both data sets confirms that, unlike the photocatalytic degradation of 4-CP, UV/Visible absorption spectrophotometry is indeed suitable for analysing the photocatalytic degradation of AO7. Indeed, no products of AO7 degradation absorbing around 485 nm could be detected by HPLC and all detected products were found to absorb at wavelengths shorter than 300 nm.

Moreover, none of the stable degradation intermediates of AO7 absorbs at wavelengths longer than 300 nm. That is why the absorption spectroscopy method can be used for precise determination of the concentration changes of AO7 during the whole photocatalytic degradation process [193].

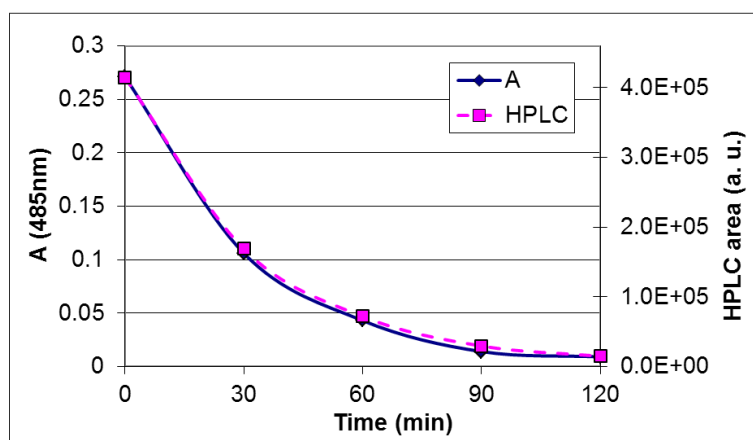


Fig. 16 Comparison of absorbance by VIS spectroscopy (in 5 cm cuvette) and HPLC peak area of AO7 at 485 nm, initial concentrations of AO7 was  $2.5 \times 10^{-5} \text{ mol.L}^{-1}$ , amount of  $\text{TiO}_2$   $0.5 \text{ m.g}^{-2}$ .

### 5.1.2. Influence of initial concentration

Fig. 17a and Fig. 17b shows the dependence of AO7 (and 4-CP) concentration on irradiation time for various initial concentrations of model compound. In both cases for a typical irradiation, the concentration of the test pollutant (AO7 or 4-CP) decreases exponentially with time which suggests apparent first order kinetics. However, the experimental first order rate constants for the degradation of AO7,  $k_{\text{exp}}$ , (shown in Table 3) decrease significantly with increasing initial AO7 concentration, whereas for the photocatalytic destruction of 4-CP the decrease of  $k_{\text{exp}}$  with increasing initial 4-CP concentration is much smaller.

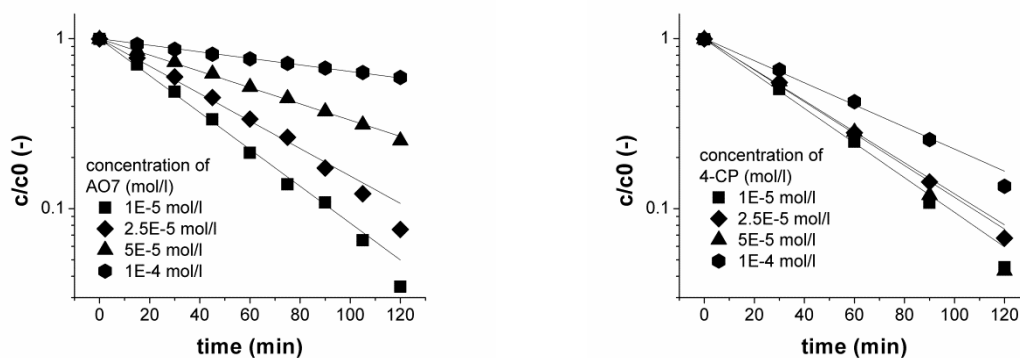


Fig. 17 Kinetics of photocatalytic degradation of a) AO 7 (left) and b) 4-CP (right) on P25 layer - different initial concentrations, speed of stirring 890 rpm

Table 3 Experimental first order rate constants,  $k_{\text{exp}}$ , and initial degradation rates,  $R_i$ , for the degradation of AO7 and 4-CP, rate of stirring 890 rpm

Concentration	AO7		4CP	
	$k_{\text{exp}}$ ( $\text{min}^{-1}$ )	$R_i$ ( $\text{mol} \cdot \text{min}^{-1} \cdot \text{cm}^{-2}$ )	$k_{\text{exp}}$ ( $\text{min}^{-1}$ )	$R_i$ ( $\text{mol} \cdot \text{min}^{-1} \cdot \text{cm}^{-2}$ )

$1.0 \times 10^{-5}$	0.0271	$-7.74 \times 10^{-10}$	0.0255	$-7.29 \times 10^{-10}$
$2.5 \times 10^{-5}$	0.0209	$-1.49 \times 10^{-9}$	0.0225	$-1.61 \times 10^{-9}$
$5.0 \times 10^{-5}$	0.0113	$-1.61 \times 10^{-9}$	0.0261	$-3.73 \times 10^{-9}$
$1.0 \times 10^{-4}$	0.0043	$-1.23 \times 10^{-9}$	0.0163	$-4.66 \times 10^{-9}$

For the evaluation of photocatalytic degradation of these two model compounds the initial degradation rate  $R_i$  (eq. 5-1-38) was used. This initial rate is calculated from the initial slope (first 30 minutes of irradiation) of the model compound concentration dependence on time. Assuming the apparent first order kinetics the initial slope of model compound is equal to  $k_{exp}$  multiplied by an initial compound concentration. Involving reaction volume  $V$  and irradiated geometrical area of photocatalyst layer  $A$ , we obtain  $R_i$  as a number of moles of model compound degraded per time and irradiated area [ $\text{mol} \cdot \text{min}^{-1} \cdot \text{cm}^{-2}$ ] (Table 3):

$$R_i = \frac{V}{A} r_i = -\frac{V}{A} \left( \frac{dc_{org}}{dt} \right)_i = -\frac{V}{A} k_{exp} \cdot c_{org}^0 \quad (5-1-0)$$

where  $r_i$  is the initial reaction rate [ $\text{mol} \cdot \text{min}^{-1} \cdot \text{dm}^{-3}$ ],  $(dc_{org}/dt)_i$  is the initial slope of AO7 (4-CP) concentration dependence on irradiation time (first 30 min) [ $\text{mol} \cdot \text{min}^{-1}$ ],  $c_{org}^0$  is the initial concentration of AO7 (4-CP) [ $\text{mol} \cdot \text{L}^{-1}$ ],  $A$  is the geometrical area of the irradiated photocatalyst layer [ $\text{cm}^2$ ] and  $V$  is the volume of the reaction mixture [L].

The initial reaction rate of photocatalytic degradation of a single model compound as a function of its initial concentration has been often described using Langmuir-Hinshelwood type (LH) expression (eq. 5-1-39) [[18](#), [194](#), [195](#)].

$$r_i = -\left(\frac{dc_{org}}{dt}\right)_i = k_{org} \frac{K_{org} c_{org}^0}{1 + K_{org} c_{org}^0} \quad (5-1-0)$$

where  $K_{org}$  is an apparent adsorption constant [ $L \cdot mol^{-1}$ ] and  $k_{org}$  is a LH rate constant [ $mol \cdot dm^{-3} \cdot min^{-1}$ ]. That the LH mechanism itself and its underlying assumptions, rather than the form of the kinetic equation (5-1-39), is not applicable to most examples of semiconductor photocatalysis, is illustrated by the fact that in most photocatalytic studies the apparent adsorption constants are invariably smaller than those obtained from a linearized form of eq. (5-1-39), namely, a plot of  $1/r_i$  vs.  $1/c^0$  [196]. Indeed, Ollis [197] showed recently that for some photocatalytic reactions, adsorption/desorption equilibrium are not established during reaction and that this can be the underlying cause for the saturation type kinetics associated with the L-H type equation (5-1-39) often found with semiconductor photocatalyst systems.

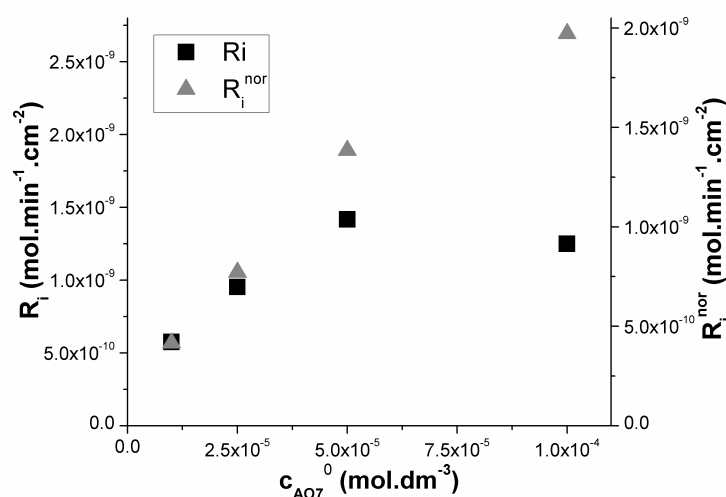


Fig. 18 Dependence of initial degradation rate and normalized initial degradation rate on initial concentration of AO7, stirring speed 1200 rpm

The dependence of the initial degradation rate  $R_i$  on AO7 initial concentration for a constant stirring speed 1200 rpm is shown in Fig. 18 (rectangles). It can be seen that for the highest concentration ( $1 \times 10^{-4} mol \cdot L^{-1}$ ) there is a significant decrease of the initial degradation rate. Similar behaviour has been observed by others in the photocatalytic destruction of Gentian Violet (initial concentration  $\geq 2.5 \times 10^{-4} mol \cdot L^{-1}$  [198]) and acid brown 14 (initial concentration  $\geq 5 \times 10^{-4} mol \cdot L^{-1}$  [53]). This feature of a plateau in rate at high pollutant concentration may not only be due to complete active site coverage by the AO7 but also UV

screening of the photocatalyst by the AO7. In the latter case at high AO7 concentrations a significant amount of UV may be absorbed by the AO7 molecules rather than by the TiO<sub>2</sub> particles. Thus, the incident light intensity  $I_i$  (at the TiO<sub>2</sub> surface) decreases with increasing AO7 concentration. Other authors [199-204] have also proposed this cause for a decrease in rate with increasing pollutant concentration and there has been an attempt to correct the observed rates based on this effect [204]. Egerton et al [204] observed a first order constant for nitrophenol degradation in a TiO<sub>2</sub> slurry system as a function of UV intensity incident on the reactor, absorption coefficient and concentration of nitrophenol. Using a model which ignores scattering and absorption by the titania particles they were able to support the conclusion that UV absorption by the nitrophenol is the major cause of the observed decrease in pseudo-first order rate constant with increasing concentration of nitrophenol.

The present study deals with TiO<sub>2</sub> films which makes possible to directly correct observed degradation rates. In order to make such a correction, a “normalized” initial AO7 degradation rate  $R_i^{nor}$  can be calculated using incident light intensity  $I_i$  (eq. 5-1-41). The incident light intensity,  $I_i$ , is schematically shown in Fig. 19.

$$R_i^{nor} = \frac{R_i}{I_i} \cdot I_0 \quad (5-1-0)$$

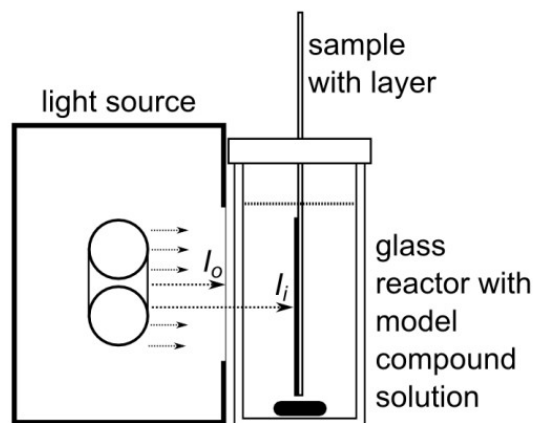


Fig. 19 The schema of batch photoreactor for determination of photoactivity of thin films – side view

Where the incident light intensity,  $I_i$ , is calculated according to:

$$I_i = I_o \cdot \text{corr}_{pos} \cdot T_{glass}^{367nm} \cdot T_{AO7}^{367nm} \quad (5-1-0)$$

where  $I_o$  is the intensity measured at the output of UV light source,  $\text{corr}_{pos}$  is calculated as the fraction by which  $I_o$  has decreased over the distance from light source to sample and  $T_{glass}^{367nm}$  is the transmittance of the reactor glass wall at 367 nm,  $T_{AO7}^{367nm}$  is the fractional transmittance of the AO7 solution at 367 nm, (which depends on AO7 concentration). The wavelength 367 nm was chosen as it corresponded to the emission maximum of BLB UV tubes used in this work. From Table 4 it can be seen that the amount of incident UV light absorbed by the AO7 solution ( $I - T_{AO7}^{367nm}$ ) increases almost linearly with AO7 concentration. In contrast, the fractional transmittance of 4-CP solution at 367 nm is ca. 1 for 4-CP concentration values used in this work, so the incorporation of a correction factor due to UV screening by the 4-CP in the calculation of a normalised degradation rate is not necessary.

The approach used for the calculation of normalized initial degradation rates assumes that the degradation rate is linearly proportional to the incident light intensity. Obviously this would not be the case at very high absorbed light intensities, under which conditions the rate of photocatalytic destruction would be expected to depend upon the square root of the absorbed light intensity, as the process of electron-hole pair recombination dominates the process [62]. It might be tempting to conclude the apparent saturation kinetics observed for the photocatalytic destruction of AO7 is due to compete surface coverage of the photocatalyst and use the data illustrated in figure 5 and eq. (5-1-39) to extract out values for  $K_{org}$  and  $k_{org}$ . However, when the rates are corrected for the fraction of UV light absorbed by the AO7, the degree of UV screening exhibited by the AO7, the results in Fig. 18 (triangles) indicate that the rate of AO7 is directly dependent upon AO7, which is expected when AO7 concentration  $K_{org}$  is  $\ll 1$  in eqn (5-1-39). Thus, the apparent (uncorrected) saturation kinetics illustrated in Table 4 for AO7 are an illusion, attributable directly to UV screening by the AO7.

Table 4 Values for calculation of  $I_i$  from measured  $I_o$

$c_{AO7} (mol.L^{-1})$	$T_{AO7}^{367}$	$T_{glass}^{367}$	$\text{corr}_{pos}$	$I_o (mW.cm^{-2})$	$I_i (mW.cm^{-2})$
$1.0 \times 10^{-5}$	0.94	0.89	0.605	2.74	1.38

$2.5 \times 10^{-5}$	0.84	0.89	0.605	2.74	1.23
$5.0 \times 10^{-5}$	0.69	0.89	0.605	2.74	1.02
$1.0 \times 10^{-4}$	0.43	0.89	0.605	2.74	0.63

### 5.1.3. Influence of mass transfer

The effect of the mass transport of the reactants (oxygen and model pollutants) to the photocatalyst on the rate of photocatalysis is another important parameter influencing the reaction. During heterogeneous catalysis involving simultaneous reactions at a catalytic surface, the apparent rate of reaction (the measured rate) can be dominated by the surface kinetics, transport kinetics or by a combination of both. As noted earlier, other work shows that the rate of photocatalytic reaction involving  $\text{TiO}_2$  particles which are uniformly distributed as freely suspended particles in the solution is completely controlled by the intrinsic reaction rate on the catalyst surface [187]. In contrast, experiments involving active particles coated on tubular surfaces or large glass beds frequently exhibit kinetics that are heavily influenced by mass transfer [194].

A simple test of mass transfer control is the observation that the rate of photocatalysis depends on the reaction solution flow rate [205-207]. Thus, in this work the effect of stirring speed on the kinetics of the photocatalytic degradation AO7 was studied ( $[\text{AO7}] = 1 \times 10^{-5} \text{ mol.L}^{-1}$ ) and the results are illustrated in Fig. 20. It can be seen that the experimental rate constant for the photocatalytic degradation of AO7 on  $\text{TiO}_2$  layers,  $k_{\text{exp}}$ , increases with increasing speed of stirring over the range 0-890 rpm. These findings indicate that the reaction rate is controlled by the mass transfer of either dissolved AO7 or dissolved oxygen to the surface of  $\text{TiO}_2$ . The observation that stirring has no effect on the photocatalytic rate of degradation of AO7 over the range 890-1160 rpm indicates that in this region, mass transfer is not the slowest step in the photocatalytic degradation, and the process can be considered to be activation controlled. A positive effect of stirring in combination with a flowing stream on the photocatalytic conversion of AO7 was reported previously but the values of stirring speed were not shown [208]. The present results are important for helping to suggest the choice of suitable stirring conditions for thin film photoactivity determinations in a mixed batch photoreactor.

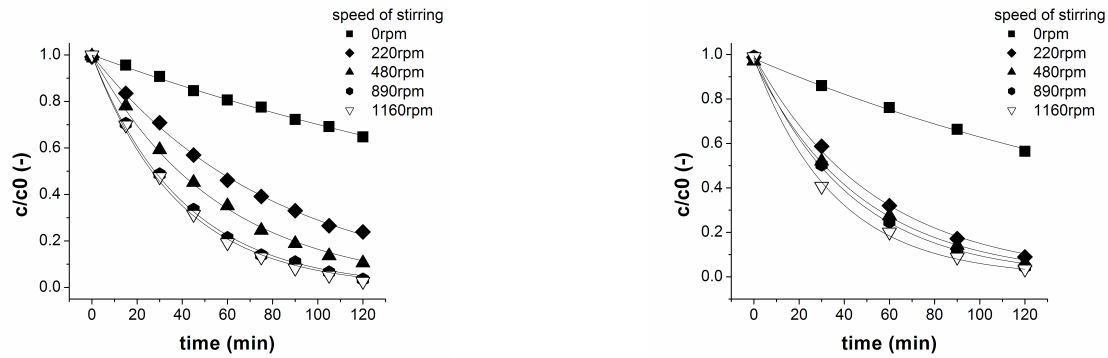


Fig. 20 Kinetics of photocatalytic degradation of a) AO7 (left) and b) 4-CP (right) on P25 layer - different speed of stirring, initial concentrations  $1 \times 10^{-5} \text{ mol.L}^{-1}$

The effect of stirring speed on the photocatalysed degradation kinetics of 4-CP (initial concentration  $1 \times 10^{-5} \text{ mol.L}^{-1}$ ) are shown in Fig. 20b and, as observed for AO7, the 4-CP concentration vs. time profiles all exhibited exponential decays. Although there is strong increase in experimental rate constant when stirring is applied (220 rpm), further increases in stirring speed (from 220 to 1160 rpm) did not produce a significant change in photocatalytic reaction rate constant, in marked contrast to that observed for AO7 (see Fig. 20a). This work indicates that only at low stirring speeds ( $< 220 \text{ rpm}$ ) the reaction rate of 4-CP is controlled either by the mass transfer of 4-CP or oxygen to the surface of  $\text{TiO}_2$ .

It is worthwhile at this point to determine if the rate of photocatalytic destruction of AO7 or 4-CP in the mass-transfer zone of stirring, are controlled by the slow transport of organic compound or slow transport of oxygen. Thus, stirring promotes mixing and decreases the boundary layer thickness  $\delta$ , thus leading to the increase of mass transfer. The flux density of oxygen or organic compound to the surface of  $\text{TiO}_2$  can be described by the first Fick's law (eq. 5-1-41):

$$J_i = -D_i \frac{c_i^0 - c_i^s}{\delta} \quad (5-1-0)$$

where  $J_i$  is the diffusion flux density of organic compound (AO7, 4-CP) or oxygen to  $\text{TiO}_2$  layer,  $D_i$  is the diffusion coefficient of AO7, 4-CP or oxygen,  $c^0$  is the concentration in the bulk and  $c^s$  is the concentration on the  $\text{TiO}_2$  surface. The limiting flux density of species 'i' is

defined for the case, when the concentration of species 'i' (oxygen or organic compound) at the surface of TiO<sub>2</sub> layer is zero.

The bulk concentration of dissolved oxygen in the aqueous solution in equilibrium with air is ca.  $0.25 \times 10^{-3} \text{ mol.L}^{-1}$  [4] and so 2.5-25 times (depending on AO7 and 4-CP concentrations used) higher than the bulk concentrations of AO7 and 4CP. Furthermore, the batch reactor was not closed and thus the bulk concentration of oxygen in aqueous solution does not decrease significantly during irradiation. The diffusion coefficient of oxygen in water is ca.  $2.34 \times 10^{-5} \text{ cm}^2.\text{s}^{-1}$  [209]. The diffusion coefficients of AO7 and 4-chlorophenol were estimated using the Wilke–Chang equation [118], which is an empirical modification of the Stokes–Einstein relation [210]. The calculated diffusion coefficient for AO7 in water ( $6.7 \times 10^{-6} \text{ cm}^2.\text{s}^{-1}$ ) was similar to that the azo dye AO8 ( $6.5 \times 10^{-6} \text{ cm}^2.\text{s}^{-1}$ , calculated also from Wilke–Chang equation [210]) which is not surprising given the similar size structure and molecular weight. The Wilke–Chang eqn. was also used to calculate the diffusion coefficient for 4-CP as  $8.2 \times 10^{-6} \text{ cm}^2.\text{s}^{-1}$ . Because both diffusion coefficients and bulk concentrations of AO7 and 4-CP are about three times lower than those for oxygen it would appear that at the conditions used in this work for the photocatalytic destruction of AO7 and 4-CP, i.e. constant light intensity and concentration of dissolved oxygen, the limiting flux density of organic compound is about an order smaller than that for oxygen. This finding suggests that the photocatalytic degradation of AO7 and 4-CP in this work – under low stirring rate conditions - would be controlled by the transport of the organic compound (AO7 or 4-CP) from the bulk solution to the TiO<sub>2</sub> layer.

## 5.2. Titanium dioxide nanoparticles

This chapter describes the behaviour of TiO<sub>2</sub> colloidal suspension. The colloidal TiO<sub>2</sub> suspensions were prepared and deeply studied to understand their behaviour under different condition as these colloidal particles will be further used for the preparation of different nanocomposite materials. The prepared TiO<sub>2</sub> suspensions had strongly acidic pH which is not compatible with all types of components used for composite preparation (which are stable only in alkaline pH) so it was necessary to increase the pH while keeping the size of particles in the range of tens of nanometres.

### 5.2.1. Influence of pH

One of the most important properties of the TiO<sub>2</sub> colloidal suspensions is the particle size. Because in the nanometre range dispersed particles display specific physico-chemical properties and lead to transparent suspensions, specific attention must be paid to the change in particle size under various conditions. In used synthetic process (described in chapter 4.1.2), the colloidal TiO<sub>2</sub> suspension obtained had a strongly acidic pH (around 2.5). For environmental applications, the stability of the TiO<sub>2</sub> colloidal suspension under basic conditions is of great interest. Thus, a series of titrations was performed using two types of alkaline reagent KOH and NH<sub>4</sub>OH at different concentrations, 0.2 and 1 mol.L<sup>-1</sup> for KOH and 0.5 and 1 mol.L<sup>-1</sup> for NH<sub>4</sub>OH. It should be emphasized that the particle size in acidic suspension was 7 nm which compares well with other sources, where sizes of 20 [205] and 4 nm [211] were reported. The differences in size are caused by slight differences in the method of preparation (different concentration and temperature).

In a preliminary step, the pH was changed to the alkaline region for two different starting concentrations of freshly prepared TiO<sub>2</sub> colloidal suspensions, namely 33.3 and 6.3 mmol.L<sup>-1</sup>. Using the most concentrated colloidal TiO<sub>2</sub>, the particle size obtained after titration was systematically bigger than that obtained from dilute suspension whatever the titrating agent. Thus in the following, only results obtained from dilute TiO<sub>2</sub> will be presented. Upon titration, it was systematically found that the colloidal suspension coagulates for pH values in the range 4-8 (Table 5).

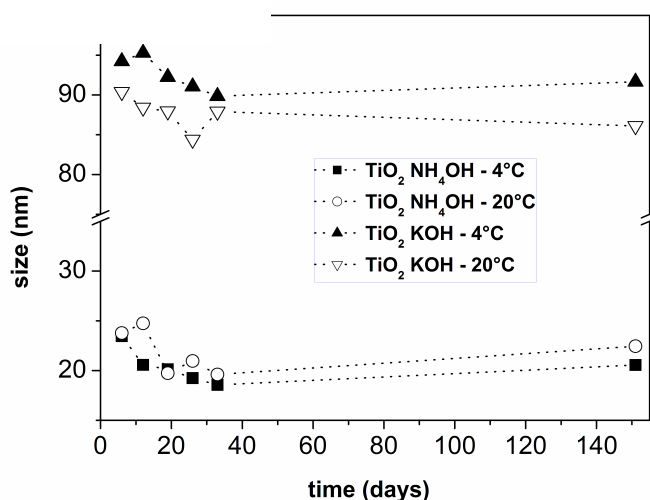
Table 5 Titration of acidic TiO<sub>2</sub> colloidal suspension by NH<sub>4</sub>OH and KOH solutions

V NH <sub>3</sub> (ml) c= 1 mol.L <sup>-1</sup>	pH	average size	appearance
0	2.43	12	clear solution
0.1	3.52	271	white turbidity
0.5	9.51	79	white turbidity
0.6	10.8	27	Almost without turbidity
V KOH (ml) c = 0.2 mol.L <sup>-1</sup>	pH	average size	appearance
0	2.43	12	clear solution
0.05	2.97	154	white turbidity
0.10	9.34	103	mild white turbidity
0.20	10.99	95	almost without turbidity

This phenomenon totally hampers any measurement of the particle size. Solutions were highly turbid (at pH either 3.5 or 10) and at pH 6 particles began settling due to precipitation. The point of zero charge ( $\text{pH}_{\text{zpc}} = 5 \pm 1$ ) of TiO<sub>2</sub> being in this range, the surface charge of the particles decreased strongly leading to aggregation, in agreement with other studies [212, 213]. However, when the pH reached values higher than 10, the change in particle size was limited. Titration up to  $\text{pH } 11.0 \pm 0.2$  led to clear basic colloidal suspensions of TiO<sub>2</sub>. It appears that titration using NH<sub>4</sub>OH solutions induces a smaller increase in particle size compared to KOH (Erreur : source de la référence non trouvéeA). Indeed, a particle size of 25 nm was obtained using 1 mol.L<sup>-1</sup> NH<sub>4</sub>OH, whereas the use of 1 mol.L<sup>-1</sup> KOH led to a size of 42 nm. In parallel the use of dilute alkaline solutions led to opposite effects, particles of 27

nm and 93 nm, respectively, were prepared for 0.5 mol.L<sup>-1</sup> NH<sub>4</sub>OH and 0.2 mol.L<sup>-1</sup> KOH. These results highlight the strong influence of the nature and concentration of the titrating agents used to modify the surface charge of TiO<sub>2</sub> particles. In all these experiments the increase in particle size arises mainly from the Ostwald ripening process [214], coalescence or aggregation.

A)



B)

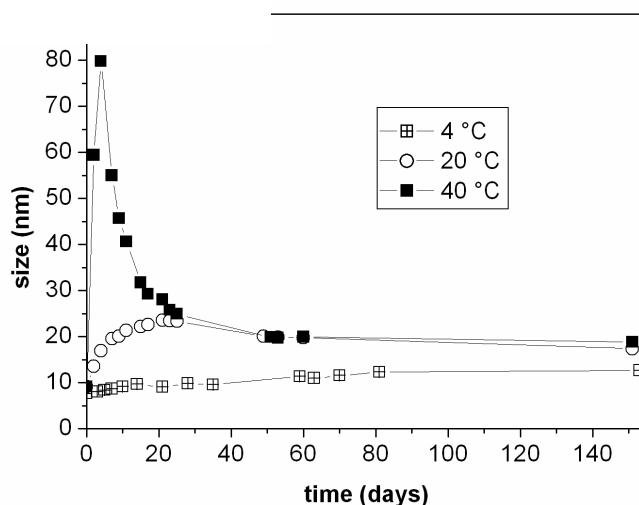


Fig. 21 A) Dependence of particle size on age of basic colloidal suspension (6.3 mmol.L<sup>-1</sup> TiO<sub>2</sub>), pH = 11.0 ± 0.3, B) Dependence of the size of TiO<sub>2</sub> particles on the age of acidic colloidal suspension (6.3 mmol.L<sup>-1</sup> TiO<sub>2</sub>), pH = 2.5 ± 0.3

The preparation of alkaline TiO<sub>2</sub> colloidal suspensions was described in [213]. However, the preparation method is too different from ours and the particles produced were less homogeneous in size. Particles prepared at pH 10 had a size of ~50 nm and contained aggregates of ~120 nm; at pH 12 the particle size was ~20 nm and the suspension also contained aggregates of size ~80 nm.

To obtain better insight into the structure of the TiO<sub>2</sub> upon titration, X-ray powder diffraction and Raman spectroscopy experiments were performed on both acidic and basic TiO<sub>2</sub> suspensions (Fig. 22). The X-ray patterns show rather large peaks of low intensity which correspond mainly to the diffraction lines of the anatase phase. The titration clearly induces an enlargement of the reflection lines, probably due to partial amorphisation of the particles under basic conditions.

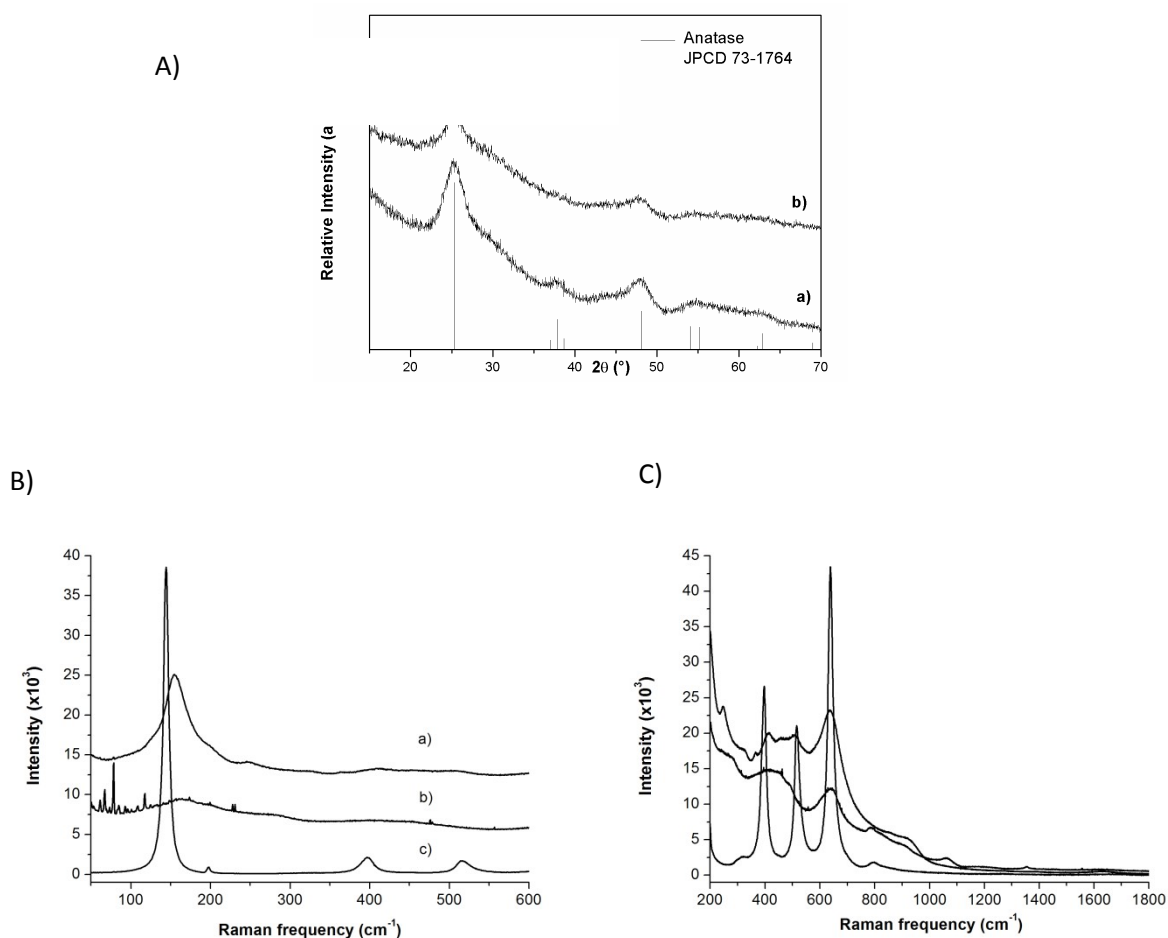


Fig. 22 A) PXRD and B) and C) Raman spectra in two different frequency ranges of TiO<sub>2</sub> obtained by drying of a) an acidic colloidal suspension, b) a basic colloidal suspension (NH<sub>4</sub>OH, 1 mol.L<sup>-1</sup>), c) TiO<sub>2</sub> anatase

The Raman spectra of the freshly prepared acidic and basic TiO<sub>2</sub> nanoparticles were compared with the spectrum of anatase TiO<sub>2</sub> from Degussa. This reference material corresponds to the anatase phase (tetragonal, I41) whose Raman vibrations appear at 144 cm<sup>-1</sup>, 197 cm<sup>-1</sup>, 396 cm<sup>-1</sup>, 514 cm<sup>-1</sup> and 640 cm<sup>-1</sup> corresponding, respectively, to the Eg(1), Eg(2), B1g(1), A1g et Eg(3) active modes [90]. Raman spectra of the acidic TiO<sub>2</sub> display large vibration bands (155 cm<sup>-1</sup>, 413 cm<sup>-1</sup>, 504 cm<sup>-1</sup>, 635 cm<sup>-1</sup>) characteristic of the anatase structure

with low crystallinity. A slight shift in the peak positions occurs compared to the Degussa TiO<sub>2</sub> compound. However, in the 200 cm<sup>-1</sup> – 600 cm<sup>-1</sup> frequency region, additional peaks are observed at 245 cm<sup>-1</sup>, 323 cm<sup>-1</sup>, 364 cm<sup>-1</sup> and 459 cm<sup>-1</sup>. These peaks may be associated with the presence of Brookite (orthorhombic, Pbcn), another polymorph of TiO<sub>2</sub>, whose Raman modes are reported to appear at 156 cm<sup>-1</sup> (A1g), 245 cm<sup>-1</sup> (A1g), 287 cm<sup>-1</sup> (B3g), 320 cm<sup>-1</sup> (B1g), 365 cm<sup>-1</sup> (B2g), 637 cm<sup>-1</sup> (A1g) [215]. After basic titration, a clear enlargement of the Raman peaks simultaneously with a deep decrease in the band intensities is observed due to a large decrease in the crystallinity. Even though some spectral features of anatase remain, the occurrence of the amorphous TiO<sub>2</sub> phase seems to prevail.

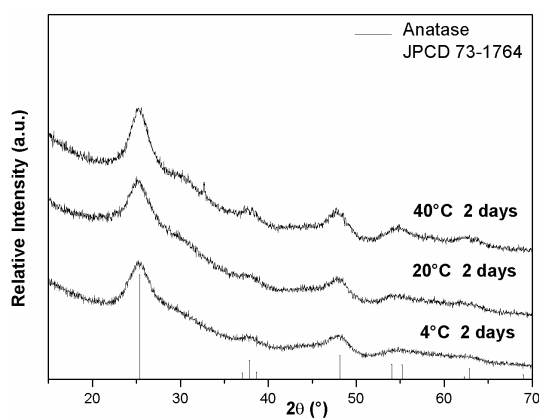
### 5.2.2. Influence of temperature and aging

Previous studies have demonstrated that aqueous TiO<sub>2</sub> colloidal suspensions undergo structural changes with time due to an increase in the average particle size [99]. Therefore, the aging of both acidic and basic colloidal suspensions of TiO<sub>2</sub> was studied at three different temperatures of storage 4 °C, 20 °C, and 40 °C to determine the best way of keeping the particles for long time periods. Erreur : source de la référence non trouvée A and B show the particle size dependence of TiO<sub>2</sub> colloidal solutions, kept at different temperatures, versus the aging time.

For the acidic suspension pH = 2.5 (Erreur : source de la référence non trouvéeB), the change in particle size is the slowest at 4 °C. After five months, the size increase does not exceed 5 nm and the suspension retains its transparency. In the first 10 days, there is only a slight increase in particle diameter from 7 to 9 nm. After three months, the average particle size remains stable at 12 nm. At 20 °C, the increase is faster; in the first 20 days the size increases from 9 nm to 24 nm. Then the particle size starts to slowly decrease and appears to be stabilized at 17 nm after five months. Note that the suspension in these conditions was slightly turbid after less than 10 days and this appearance did not disappear after an extended period of storage. The biggest increase in particle size was observed for a temperature of 40 °C. Initially, a rapid increase up to 80 nm is observed and then a continuous decrease to 20 nm occurs. This fast size increase can be explained by the formation of agglomerates as a consequence of the moderate thermal treatment. However, these agglomerates were not stable and broke down with time. In this case the suspension was very turbid after two days of storing at 40 °C. This white turbidity did not decrease, even after more than 50 days, whereas the particle size was almost the same as for temperature maintained at 20 °C, showing that the suspension still contained large agglomerates.

For the basic TiO<sub>2</sub> colloidal suspensions obtained using 0.5 mol.L<sup>-1</sup> NH<sub>4</sub>OH and 0.2 mol.L<sup>-1</sup> KOH, only aging at 4 and 20 °C was followed because we found that aging at 40 °C does not allow storage of the colloidal suspensions. Indeed, such a high temperature induced precipitation of the nanoparticles. As shown in Erreur : source de la référence non trouvée A, the particle size was measured just after synthesis and titration and then periodically up to five months. The particle size decreased slightly with time. However, it should be underlined that after titration with NH<sub>4</sub>OH and storage at 4 and 20 °C the particle size remained approximately constant and comparable with that of a freshly prepared acidic suspension of TiO<sub>2</sub>.

The structural changes of the TiO<sub>2</sub> particles under different conditions of storage were investigated in acidic suspensions. The samples used for PXRD measurement were carefully prepared by the evaporation of each suspension at room temperature to as much as possible to prevent changes of size during the evaporation process. The PXRD patterns clearly show a net increase in the crystallinity of the phases induced by both temperature and time of aging (Fig. 23).



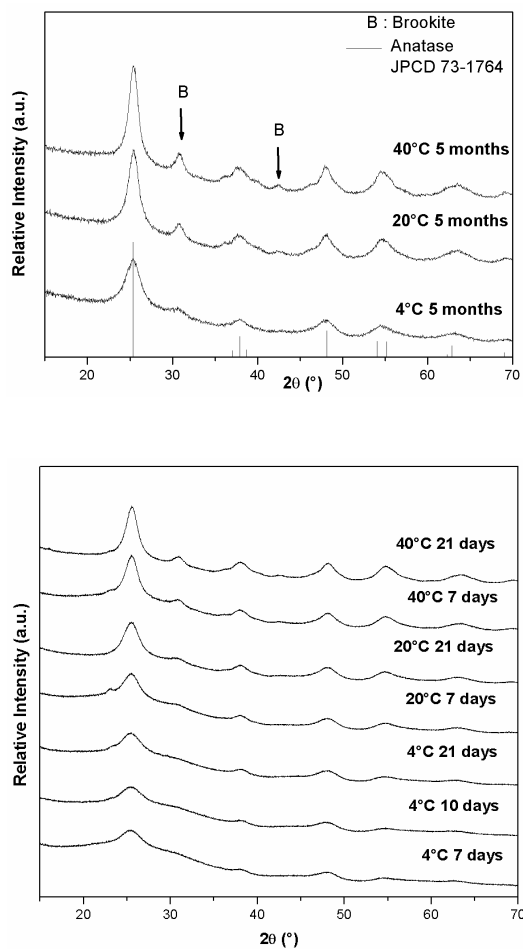


Fig. 23 PXRD of TiO<sub>2</sub> from acidic suspension after different times of storage at 4 °C, 20 °C.

The reflection lines are typically those of the anatase phase, regardless of the conditions used for storing. However, simultaneously with the increase in the crystalline anatase phase, the formation of Brookite is observed. From the PXRD diagrams, the size of the coherent domains have been estimated in applying the Scherrer formula to the 101 line width at half maximum and these results are displayed in Table 6. The values clearly indicate an increase in the coherent domain size when the temperature of storage is higher. Systematically values calculated from XRD give smaller particle sizes than those measured by dynamic light scattering, suggesting either the formation of polycrystalline particles or the presence of an amorphous phase [216].

Table 6 Size of the coherent domains determined from the 101 diffraction line width and position of the Eg band from Raman spectra.

TiO <sub>2</sub> Sample	XRD	Raman spectroscopy
	D <sub>101</sub> (nm ± 0.5)	Band position (cm <sup>-1</sup> )
4 °C – 7 days	2.3	-
4 °C – 10 days	3.0	-
4 °C – 21 days	3.2	-
4 °C – 5 months	4.7	154.8
20 °C – 7 days	4.6	-
20 °C - 21days	5.0	-
20 °C – 5 months	6.7	153.2
40 °C – 7 days	6.0	-
40 °C – 21 days	6.2	-
40 °C – 5 months	8.2	151.8

After 2 days of aging of acidic suspensions, the Raman peaks are large (Fig. 24). The low temperature treatment shows mainly the anatase Raman feature, with broad lines pointed at 417 cm<sup>-1</sup> (B1g(1)), 514 cm<sup>-1</sup> (A1g) and 637 cm<sup>-1</sup> (Eg(3)). However the bands of Brookite also contribute to the general spectrum and appear more clearly when the storing temperature is

raised at 40°C. The effect of longer aging time clearly affects the structure as shown on the Raman spectra (Fig. 25). The band widths decrease, the relative intensities change and the number of peaks increases as observed for colloidal TiO<sub>2</sub> aged for 5 months at 40 °C (Fig. 25 d) compared to colloidal TiO<sub>2</sub> aged for 2 days at 40°C (Fig. 24 d).

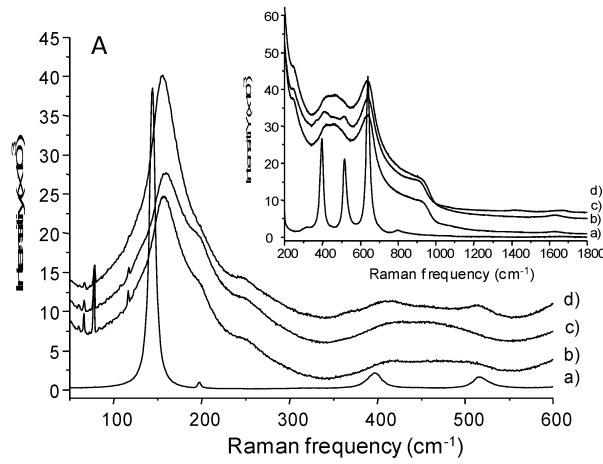


Fig. 24: Raman spectra of TiO<sub>2</sub> anatase (a) and acidic colloidal TiO<sub>2</sub> aged 2 days at 4 °C (b), 20 °C (c) and 40 °C (d).

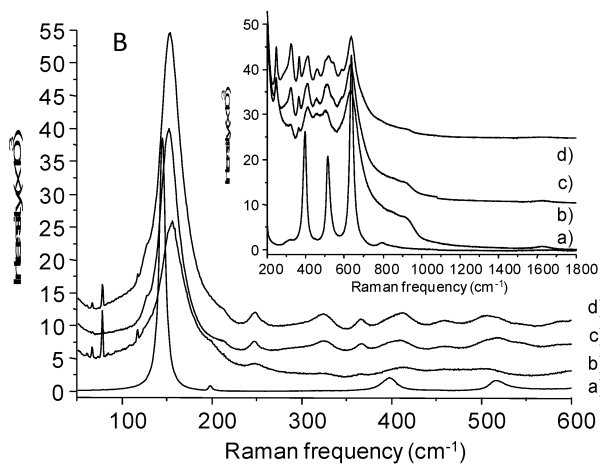


Fig. 25: Raman spectra of TiO<sub>2</sub> anatase (a) and acidic colloidal TiO<sub>2</sub> aged 5 months at 4 °C (b), 20 °C (c) and 40 °C (d).

Both anatase and brookite are present, the former being the major phase (Table 7). According to thermodynamic considerations the phase stability for the three polymorphs of TiO<sub>2</sub> decreases in the sequence: rutile > brookite > anatase. Then the phase transition from anatase to Brookite may occur [217]. Anatase-Brookite phase transition is dependent on the nanoparticle size. Anatase has been reported to be more stable than Brookite with

nanocrystals of size smaller than 11 nm [211] due to the favourable surface energy. However, with changes in grain size, anatase may be transformed to the Brookite polymorph by nanoparticle aggregation.

Table 7 Identification of Raman vibrations for colloidal TiO<sub>2</sub> aged 5 months at 40 °C.

Bands (cm <sup>-1</sup> )	Eg	A1g	Eg	A1g	B3g		B1g	B2g	B1g	A1g						A1g
Colloid. TiO <sub>2</sub> 5 months 40 °C		152	211	247	287		324	367		411	460	502	519	541	587	635
TiO <sub>2</sub> anatase	144		197			318			396				514			640
TiO <sub>2</sub> Brookite		156		245	287		320	365								637

Colloidal suspensions display Raman peaks shifted and broadened in comparison with Raman spectra of crystallized Degussa TiO<sub>2</sub>. This is clear for the most intense Eg peak (140 – 150 cm<sup>-1</sup>). This phenomenon is due to the nanosize properties of the colloidal TiO<sub>2</sub> which induces breakdown of the k=0 Raman selection rule and the subsequent Raman activation of phonons far from the centre of the Brillouin zone [218]. The ratio of the full width at half maximum (FWHM) of the Eg band (144 cm<sup>-1</sup>) of TiO<sub>2</sub> nanoparticles over TiO<sub>2</sub> anatase (Degussa) was plotted versus the corresponding Raman frequency shift (%) (Fig. 26). Values of FWHM were determined by profile analysis using a Lorentzian function. The change follows the same tendency as that reported by Kelly et al. [219] showing the dependency of the FWHM-frequency on the particle grain size.

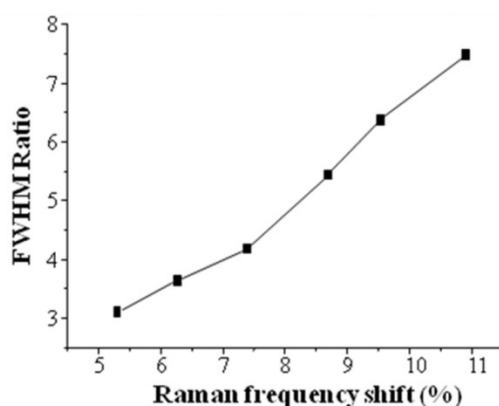


Fig. 26 FWHM ratio versus Raman frequency shift for the Eg(1) mode. Reference material is TiO<sub>2</sub> P25 Evonik.

### 5.2.3. Evolution of the band gap energy and photocatalytic activity

Another important property of TiO<sub>2</sub> nanoparticles is their band gap energy. The change in band gap energy ( $E_g$ ) with time of aging was determined from the absorbance spectra. The  $E_g$  was calculated from absorbance spectra of TiO<sub>2</sub> suspensions. The sample of the calculation is described for freshly prepared TiO<sub>2</sub> suspension. As a first step, influence of water was eliminated by subtraction of absorbance of pure water (named as Difference in Fig. 27). Then the extrapolation by exponential function in the region 450-800 nm was performed to reach the zero absorbance of measured spectrum in mentioned region and this extrapolation was then subtracted from whole spectrum, marked as Corrected. The result of this treatment is shown in Fig. 27. The spectrum marked as Corrected was transformed to Kubelka-Munk function and the linear part of this function was used for determination of band gap energy. Result of this transformation is shown in Fig. 28. Band gap energy was then obtained at  $\ln(\alpha) = 6.5$  (anatase has  $E_g = 3.2$  eV at  $\ln(\alpha) = 6.5$  [186]). The same calculation was performed for all samples.

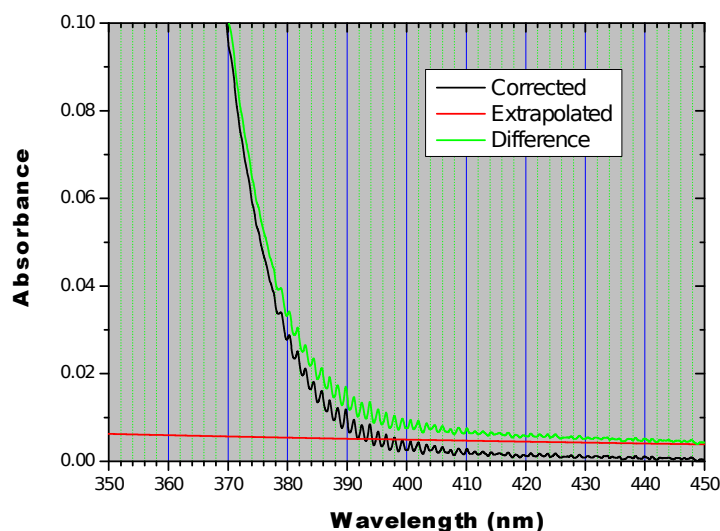


Fig. 27 Calculation of band gap energy – treatment of measured absorbance spectrum of freshly prepared TiO<sub>2</sub> suspension

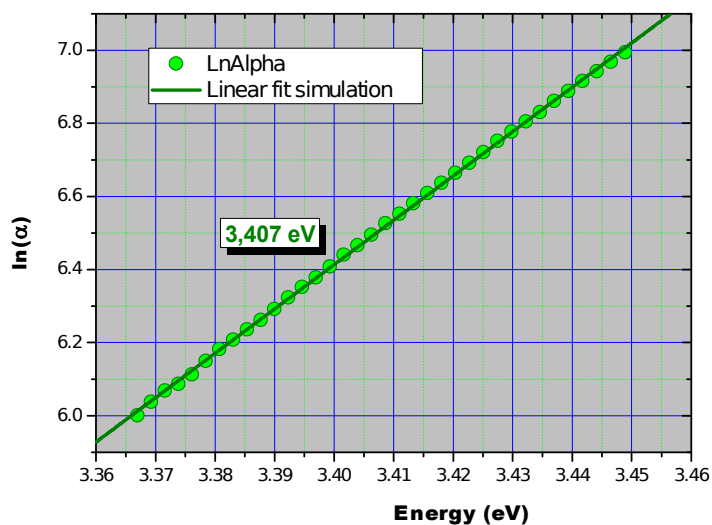


Fig. 28 Calculation of band gap energy – linear part of Kubelka-Munk function of freshly prepared TiO<sub>2</sub> suspension

$E_g$  for freshly prepared suspensions was about 3.4 eV. The increase in value of the band gap comparing to 3.2 eV reported for anatase solid phase is due to the so called quantum sized effect causing a blue shift in the UV-VIS spectra. For all acidic colloidal suspensions, the band gap energy decreased with time, the fastest decrease being observed for the suspension kept at 40 °C, and the slowest for that kept at 4 °C. All the values for the band gap energy are summarized in Fig. 29A.

In contrast to acidic suspensions of TiO<sub>2</sub>, almost no change in band gap energy was observed under alkaline conditions (Fig. 29B) with time. This is in agreement with the finding that the size of particles in alkaline suspensions decreased very slowly with time. However, it is noteworthy that titration from freshly prepared acidic suspensions caused an immediate decrease of band gap energy on all occasions. In the case of KOH this decrease was higher (from 3.40 to 3.30 eV) than for NH<sub>4</sub>OH (from 3.40 to 3.37 eV).

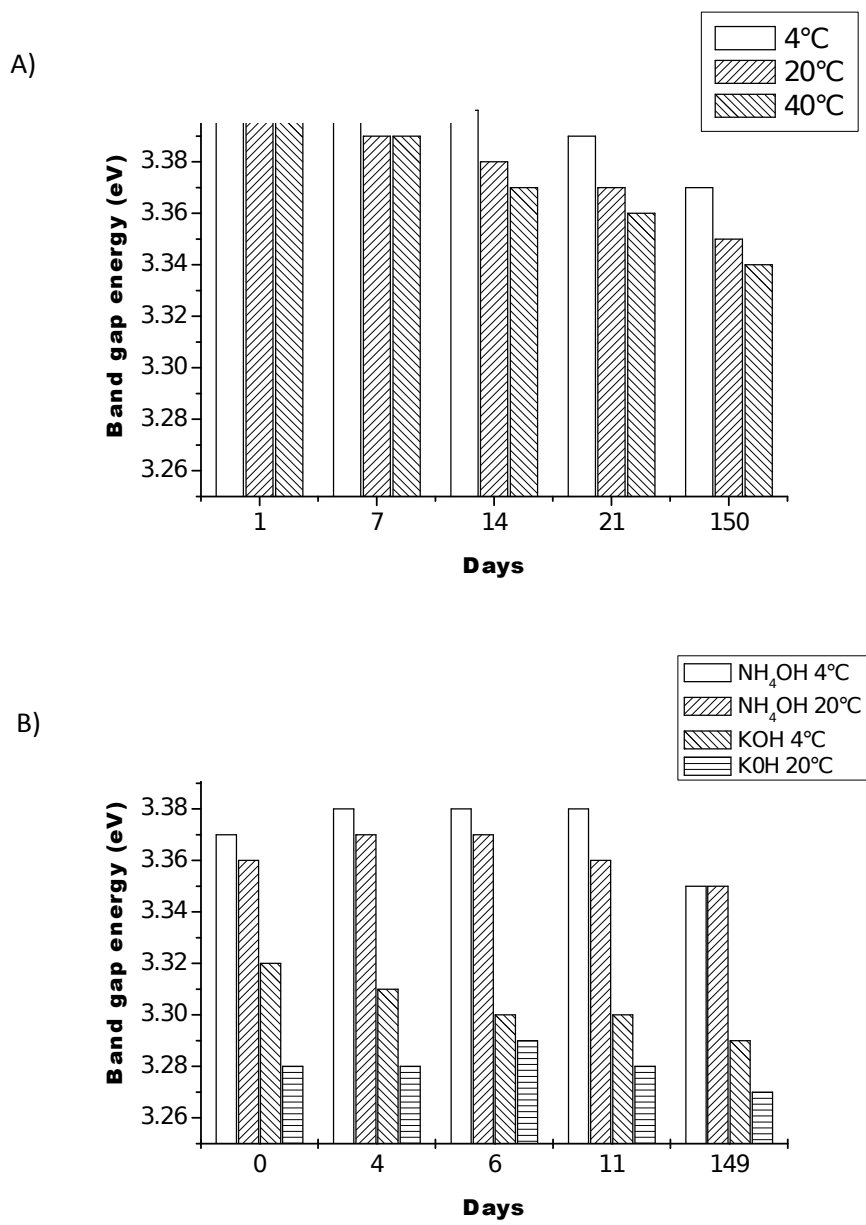


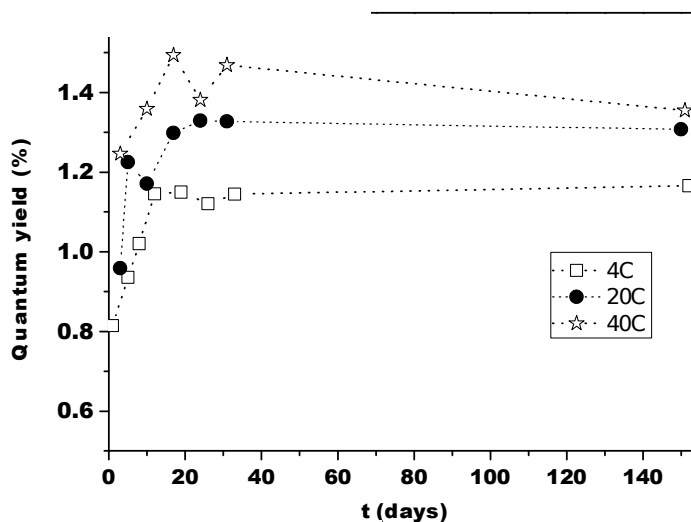
Fig. 29 Band gap energy values after different periods of storage A) at different temperatures, B) after titration with 0.2 mol.L<sup>-1</sup> KOH or 1 mol.L<sup>-1</sup> NH<sub>4</sub>OH.

The photocatalytic activity was measured using 4-chlorophenol as a model pollutant. In Fig. 30, the quantum yields of the photocatalytic degradation of 4-chlorophenol are shown. The quantum yields were calculated by the equation 4-5-37.

For the freshly prepared suspension the starting value of the quantum yield of 4-chlorophenol degradation was 0.8 %. When the suspension was kept at 4 °C, after 15 days the value increased to 1.1 % and it remained almost unchanged for longer aging. For the

suspensions stored at 20 °C and 40 °C, the quantum yield increased up to 1.3 % and 1.4%, respectively, and then kept constant. The quantum yield for 4-CP photocatalytic degradation increased in the course of aging to reach a limiting value after about 30 days at all investigated temperatures. An analogous increase was observed in the mean particle size.

A)



B)

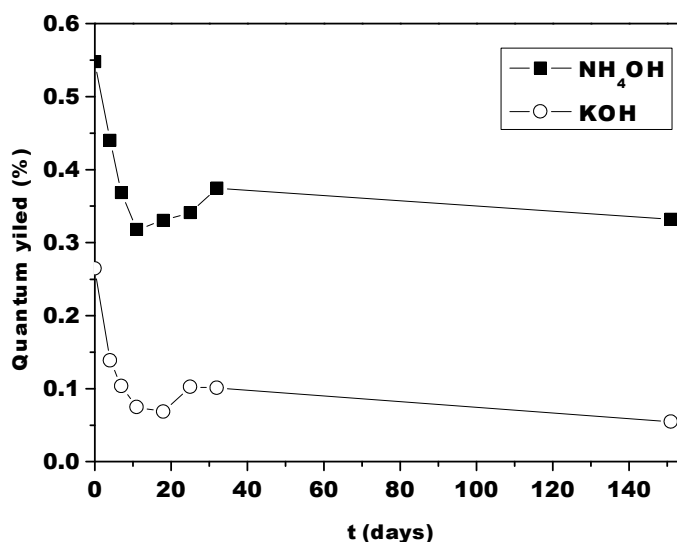


Fig. 30 Dependence of quantum yield of photocatalytic degradation of 4-chlorophenol on age of colloidal suspension A) for storage at various temperatures B) after titration with 0.2 mol.L<sup>-1</sup> KOH or 1 mol.L<sup>-1</sup> NH<sub>4</sub>OH and storage at 4 °C.

The quantum yields of the degradation of organic compounds obtained with a basic suspension of  $\text{TiO}_2$  were always lower than those obtained with acidic  $\text{TiO}_2$  suspensions. In contrast to the quantum yield obtained with acidic  $\text{TiO}_2$  suspension, that obtained with basic suspensions decreased with time. The titration of colloidal suspensions from acidic to alkaline is connected with partial aggregation. This phenomenon is more pronounced with KOH, the starting average size being between 90 to 95 nm, while with  $\text{NH}_4\text{OH}$  it was only about 25 nm. The average size decreased slightly with time, probably due to partial deaggregation. Parallel to the deaggregation the quantum yield decreased slightly. This partial deaggregation is connected with synchronous amorphisation of the phase and decrease in the quantum yield.

### 5.3. TiO<sub>2</sub>/LDH composites

For the preparation of new composite materials based on TiO<sub>2</sub>/LDH materials, colloidal suspensions of TiO<sub>2</sub>, which were carefully described in chapter 5.2, and Mg<sub>2</sub>Al-LDH were used. The commercial product Ludox AS30 was used as a source of SiO<sub>2</sub>. The stability of SiO<sub>2</sub> and prepared composite materials is described in following chapters.

#### 5.3.1. Nanocomposite elaboration and characterization

The process used for preparing TiO<sub>2</sub>/LDH nanocomposites is based on the self-assembly by electrostatic interaction of TiO<sub>2</sub> nanoparticles on the surface of LDH nanosheets. In one hand, pure Mg<sub>2</sub>Al-NO<sub>3</sub> LDH phase prepared by classical coprecipitation was delaminated by suspension in formamide. After one day, a translucent colloidal solution of LDH nanosheets was obtained as evidenced by the Tyndall light scattering effect observed in Fig. 31a). TEM image also confirms the presence of thin LDH platelets in the range of 20-140 nm into the solution (Fig. 31). Note that a zeta potential ( $\zeta$ ) of + 25.2 mV was measured for LDH precursor in water evidencing the positively charged LDH surface. In another hand, TiO<sub>2</sub> nanoparticles were prepared by controlled TiCl<sub>4</sub> hydrolysis in water [183] and let to stabilize during three months in acidic solution [220] (pH ~2.5). After this time, dynamic light scattering measurements performed on the stable transparent solution evidenced the presence of 11 nm TiO<sub>2</sub> nanoparticles with a zeta potential of + 39 mV. To promote the self-assembly process with LDH nanosheet, the charge inversion of the TiO<sub>2</sub> surface was carried out by controlled basic titration leading to a  $\zeta$  value of -41 mV. Despite a slight increase of the TiO<sub>2</sub> particle size from 11 to 26 nm, a basic TiO<sub>2</sub> colloidal suspension was yielded (Fig. 31B and C). TEM image (Fig. 31E) clearly shows the presence of particles in the nanometre range which tend to aggregate.

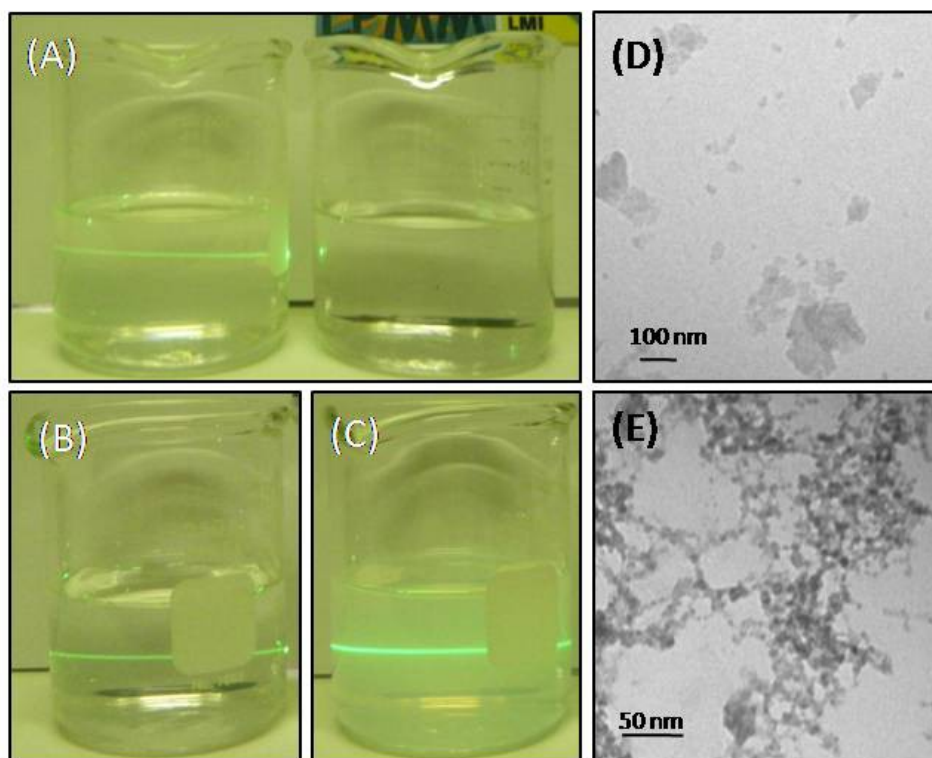


Fig. 31 Pictures of the colloidal suspensions of A)  $\text{Mg}_2\text{Al-LDH}$  in formamide compared to pure water, B) acidic  $\text{TiO}_2$  nanoparticles in water, C) basic aqueous solution of  $\text{TiO}_2$  nanoparticles, D) TEM images of  $\text{MgAl-NO}_3$  nanosheet and E) TEM images of basic  $\text{TiO}_2$  nanoparticles.

Subsequently,  $\text{TiO}_2/\text{Mg}_2\text{Al}$  nanocomposites were obtained by spontaneous flocculation after mixing  $\text{Mg}_2\text{Al}$  nanosheet delaminated in formamide and  $\text{TiO}_2$  nanoparticles in water. Interestingly, by changing the  $\text{TiO}_2$  volume in the procedure it was possible to investigate the interactions between the both components. A progressive increase of  $\text{TiO}_2$  volume, typically 5.4 mL, 21.5 mL or 65 mL (corresponding to a theoretical  $\text{TiO}_2/\text{LDH}$  mass ratio of 0.125, 0.5 and 1.5), considerably improved the yield of recovered flocculated materials i.e. 22.2%, 58.6% and 65.2% respectively. Larger the  $\text{TiO}_2$  volume involved, better the destabilization of the colloidal solution is.

Elemental analysis of the materials (Table 8) indicated a slight increase of the  $\text{Mg}/\text{Al}$  ratio after the delamination-restacking process compared to the  $\text{Mg}_2\text{Al-NO}_3$  precursor.

Table 8 Elemental analysis results, amount of water, BET surface area and pore volume

Sample	Mg/Al	Ti/Al	nH <sub>2</sub> O*	Total Weight* loss%	BET surface area (m <sup>2</sup> .g <sup>-1</sup> )	Vp (cm <sup>3</sup> .g <sup>-1</sup> )
Mg <sub>2</sub> Al-NO <sub>3</sub>	2.0	-	1.7	51	266	0.107
TiO <sub>2</sub> /Mg <sub>2</sub> Al <sub>1.5</sub>	2.2	2.82	3.7	28	24	0.272

\*Calculated from TGA analysis

This modification may be correlated to a partial dissolution/reprecipitation of the Mg<sub>2</sub>Al matrix. In parallel, the atomic Ti/Al ratio can be compared to the theoretical one of 5.2 deduced from the respective amount of each compounds involved in the process. Then, the amount of TiO<sub>2</sub> successfully immobilized at the surface of Mg<sub>2</sub>Al- was estimated at 53%. The water amount estimated by thermogravimetric analysis, is larger in the nanocomposite than in the precursor materials. This trend may be explained by the modification of the intergranular and intercrystalline porosity during the delamination-restacking process. Moreover, the total weight loss of the TiO<sub>2</sub>/MgAl<sub>1.5</sub> nanocomposite is much smaller than that of the precursor materials, which is in good agreement with the presence of almost 39% in weight of TiO<sub>2</sub> in the materials.

Fig. 32 shows the powder X-Ray diffractograms (PXRD) of the TiO<sub>2</sub>/MgAl nanocomposites obtained for different amounts of TiO<sub>2</sub>. The comparison with the starting materials that is nitrate intercalated MgAl-LDH and basic TiO<sub>2</sub> samples clearly evidence the presence of both components into the recovered samples. Indeed the LDH characteristic diffraction lines are systematically observed on the nanocomposite patterns, especially the 001, 120, 110 and 113. In addition, the wide diffraction lines of relatively low intensity belonging to the anatase TiO<sub>2</sub> nanoparticles are also present.

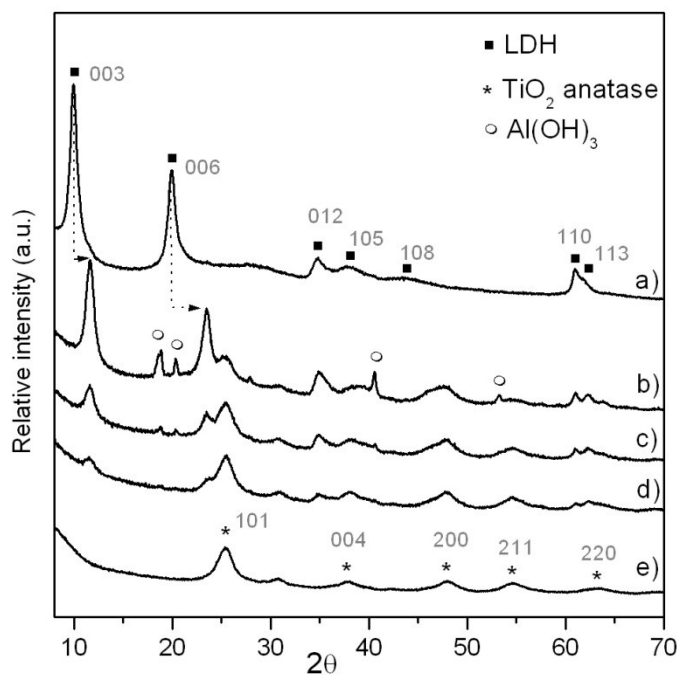


Fig. 32 XRD patterns of a) pristine  $\text{Mg}_2\text{Al-NO}_3$ ,  $\text{TiO}_2/\text{Mg}_2\text{Al}$  nanocomposites with different ratios b)  $\text{TiO}_2/\text{Mg}_2\text{Al}_{0.125}$ , c)  $\text{TiO}_2/\text{Mg}_2\text{Al}_{0.5}$ , d)  $\text{TiO}_2/\text{Mg}_2\text{Al}_{1.5}$  and e) pure anatase  $\text{TiO}_2$  from Degussa.

Note that the ratio of the  $\text{TiO}_2$  101 and  $\text{Mg}_2\text{Al}$  LDH 003 peak intensities varies according to the respective proportions of each component involved initially into the delamination-restacking process. Larger the  $\text{TiO}_2$  amount, higher the intensity ratio is. Additional diffraction lines of low intensity also appeared on the diagram at  $18.7^\circ$ ,  $20.4^\circ$ ,  $40.5^\circ$  and  $53.2^\circ$  which correspond to a side  $\text{Al}(\text{OH})_3$  phase. This latter is formed through a partial dissolution of the  $\text{Mg}_2\text{Al}$ -matrix during the delamination phenomenon, as previously underlined by Sasaki and coll. [134]. Interestingly, at high  $\text{TiO}_2$  loading, the LDH 001 line intensity decreases noticeably compared to the 110 diffraction line, evidencing the loss of stacking periodicity in the  $\text{TiO}_2/\text{Mg}_2\text{Al}_{1.5}$  material. It is also noteworthy the shift of the 001 lines to higher 2 theta values from  $11.6^\circ$  (0.88 nm) to  $9.9^\circ$  (0.76 nm) which correspond to a decrease of the interlayer spacing due to the replacement of nitrate anions by carbonate, since no precaution was taken to prevent the contamination with atmospheric  $\text{CO}_2$ . Such interlayer anion modification is further confirmed by the IR and Raman spectroscopy analysis. Fig. 33 displays the comparison between pristine  $\text{Mg}_2\text{Al-NO}_3$  and  $\text{TiO}_2/\text{Mg}_2\text{Al}_{1.5}$  nanocomposite, which will be mainly studied in the following of the study. Into the nanocomposite, the net decrease of the absorption bands at  $1387\text{ cm}^{-1}$  and  $828\text{ cm}^{-1}$  provides evidence about the anionic exchange of the nitrate anion during the self-assembly process. The band centred at  $1358\text{ cm}^{-1}$  is characteristic of the  $\nu_3$  carbonate anion. However, the low intensity of this band seems indicate that the LDH charge balance is mostly ensure by the negatively charged surface of  $\text{TiO}_2$ . In addition, all the typical vibration bands of  $\text{Mg}_2\text{Al}$  are also present on the

spectra ( $\nu(\text{OH})$ :  $3440\text{ cm}^{-1}$ ,  $\nu(\text{HOH})$ :  $1619\text{ cm}^{-1}$ ,  $\nu(\text{MO})$ :  $676\text{ cm}^{-1}$ ,  $\nu(\text{MO})$ :  $445\text{ cm}^{-1}$ ). Note that the enlargement of the absorption band in the low wavenumber region (below  $1000\text{ cm}^{-1}$ ) is associated with the O-Ti-O vibration bands. Concomitant flocculation of  $\text{TiO}_2$  during the LDH delamination-restacking process is further evidenced by the presence of its characteristic Raman vibration at  $154\text{ cm}^{-1}$ ,  $406\text{ cm}^{-1}$ ,  $516\text{ cm}^{-1}$  and  $638\text{ cm}^{-1}$  corresponding respectively, to the  $\text{E}_g(1)$ ,  $\text{B}_{1g}(1)$ ,  $\text{A}_{1g}$  and  $\text{E}_g(3)$  active modes Fig. 34.

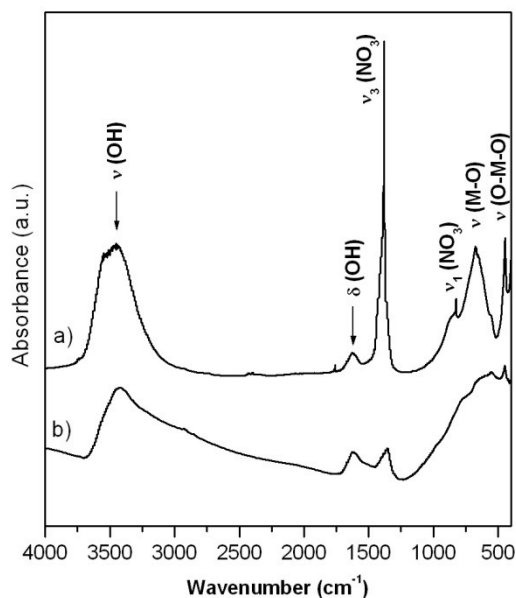


Fig. 33 FTIR spectra of a) pristine  $\text{Mg}_2\text{Al-NO}_3$  and b)  $\text{TiO}_2/\text{Mg}_2\text{Al}_{1.5}$  nanocomposite

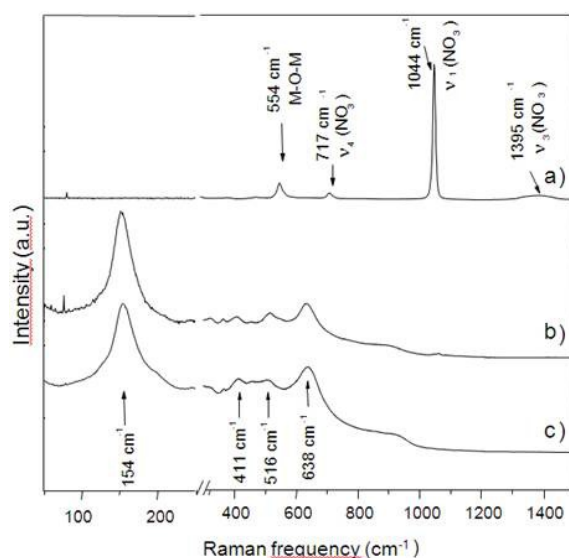


Fig. 34 Raman spectra of a) pristine  $\text{Mg}_2\text{Al-NO}_3$ , b)  $\text{TiO}_2/\text{Mg}_2\text{Al}_{1.5}$  nanocomposite and c)  $\text{TiO}_2$  recovered after evaporation of the water.

Furthermore, as underlined above in IR spectroscopy the intense band around  $1044\text{ cm}^{-1}$  corresponding to interlayer nitrate anions  $\nu_1$  is observed in the Raman spectra for the pristine LDH matrix whereas in this region, no band is observed in the nanocomposite spectra, evidencing the nitrate anionic exchange and the absence of carbonate anions.

To get better insight on the surface properties of the  $\text{TiO}_2/\text{Mg}_2\text{Al}_{1.5}$ , X-ray photoelectron spectrum was also recorded Fig. 35. Thanks to the quantification based on the peak area (Ti (11.06%), Al (4.09%), Mg (8.99%), O (72.63%) in atomic concentration) it was permitted to corroborate the chemical composition previously described. Furthermore the Ti 2p core level region is analysed into two symmetrical peaks located at 462.2 eV (Ti  $2p_{1/2}$ ) and at 456.5 eV (Ti $2p_{3/2}$ ) with a typical difference of 5.7 eV, in agreement with the presence of  $\text{Ti}^{4+}$ .

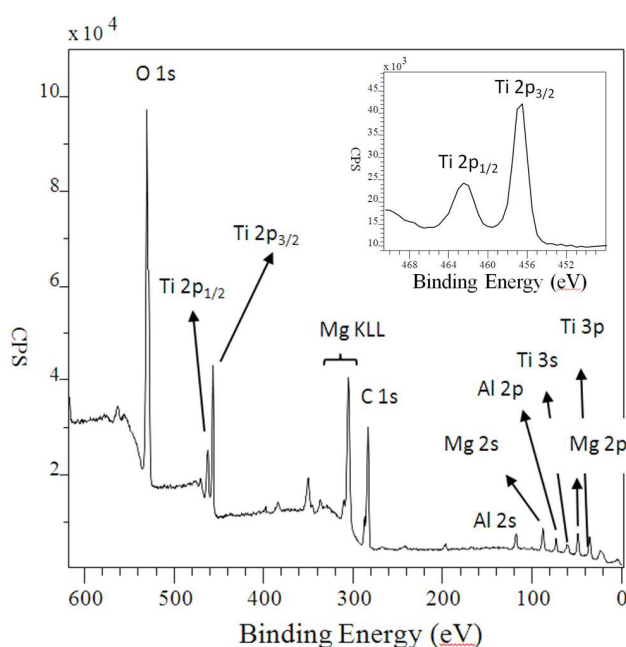


Fig. 35  $\text{TiO}_2/\text{MgAl}_{1.5}$  a) X-ray photoelectron spectrum. The peaks corresponding to O 1s, Ti  $2p_{1/2}$ , Ti $2p_{3/2}$ , C 1s, Al 2s, Mg 2s, Al 2p, Ti 3s, Mg 2p and Ti 3p core levels and the Auger structure (Mg KLL) are indicated. In inset, high resolution XPS spectra in the Ti 2p region.

The morphology of the flocculated  $\text{TiO}_2/\text{MgAl}_{1.5}$  nanocomposite was monitored by FESEM and TEM analysis as shown in Fig. 36a and b. On the FESEM image, the materials appear as the stacking of ill-defined particles in which  $\text{TiO}_2$  nanoparticles cannot be distinguished. On the contrary, TEM images clearly evidences that the LDH nanosheets are entirely covered by  $\text{TiO}_2$  nanoparticles. Image analysis permitted to calculate an average size of  $10\text{ nm} \pm 1.5\text{ nm}$  comparable to the size obtained by dynamic light scattering. It is

interesting to underline that no  $\text{TiO}_2$ -free LDH particles have been observed by TEM, which confirmed the good affinity between the two types of particles. EDX analysis of several ultra-thin particles Fig. 36c) confirmed the presence of the different elements that is Mg, Al and Ti into the sample with a Mg/Al ratio of 2.2 comparable to that previously obtained by ICP-AES, whereas a Ti/Al ratio in the range of 2.2 and 2.9 was measured according to the zone of analysis. This highlights a quite homogeneous repartition of the  $\text{TiO}_2$  nanoparticles at the surface of the  $\text{Mg}_2\text{Al}$  nanosheets.

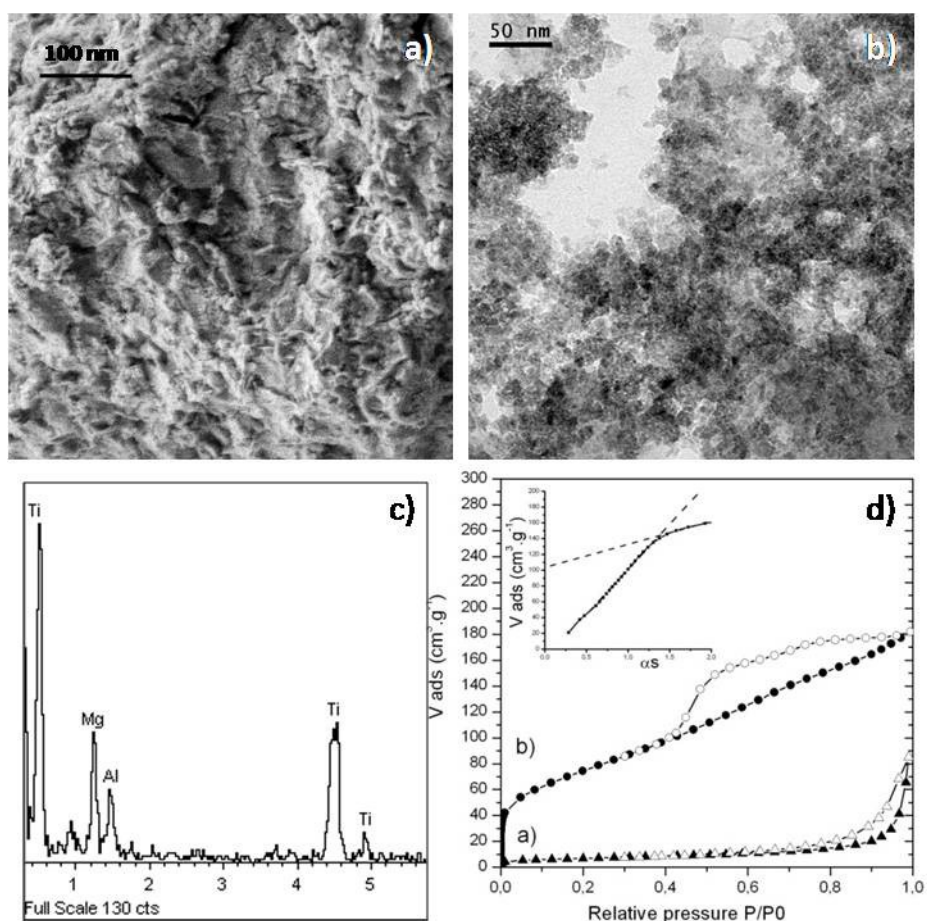


Fig. 36 a) FE-SEM image, b) TEM image, c) EDX spectrum of  $\text{TiO}_2/\text{MgAl}_{1.5}$  and d)  $\text{N}_2$  adsorption/desorption isotherms of a)  $\text{Mg}_2\text{Al-NO}_3$  and b)  $\text{TiO}_2/\text{MgAl}_{1.5}$ ,  $\alpha_s$  plot is reported in inset

$\text{N}_2$  adsorption-desorption experiments were also carried out to better characterize the modification induced by the  $\text{TiO}_2$  immobilization on the textural properties of the  $\text{TiO}_2/\text{MgAl}_{1.5}$  nanocomposite. Strikingly, an important modification of the isotherm shape was evidenced for the  $\text{TiO}_2/\text{MgAl}_{1.5}$  nanocomposite compared to the  $\text{MgAl-NO}_3$ . Indeed, as expected the LDH precursor displays a typical IV isotherm with a H3 type hysteresis loop while after  $\text{TiO}_2$  immobilization, the material exhibits a H4 type hysteresis loop Fig. 36d). Such change is associated with a net increase of the surface area from  $24 \text{ m}^2/\text{g}$  to  $266 \text{ m}^2/\text{g}$

mainly due to microporosity creation as evidenced by the  $\alpha_s$ -plot method (Fig. 36d inset). This suggests that the anchorage of TiO<sub>2</sub> nanoparticle on the surface of the Mg<sub>2</sub>Al- nanosheets induced modification in interparticle texture.

TiO<sub>2</sub>/MgAl<sub>1.5</sub> nanocomposite band gap was calculated by treatment of the diffuse reflectance UV/vis spectra. A value of 3.19 eV was found which is slightly smaller than the value of 3.29 eV measured for pure TiO<sub>2</sub> after titration.

### 5.3.2. Photocatalytic activity

Then, the photocatalytic activity of TiO<sub>2</sub> nanoparticles immobilized on Mg<sub>2</sub>Al nanosheets was evaluated. The TiO<sub>2</sub> nanoparticles display high photocatalytic activity which is of great interest in the degradation of organic pollutants such as dyes [79] and pesticides [183]. But nanoparticles are very difficult to recover from aqueous solutions. There is a great need to immobilize these nanoparticles for further environmental applications. The evaluation of photocatalytic efficiency of TiO<sub>2</sub>/Mg<sub>2</sub>Al<sub>1.5</sub> nanocomposite was performed using both Acid Orange 7 and 4-chlorophenol as model compounds. The results of photocatalytic degradation of AO7 are reported in Fig. 37. As clearly shown, the degradation of Acid Orange 7 was lower for prepared TiO<sub>2</sub>/Mg<sub>2</sub>Al<sub>1.5</sub> nanocomposite than for acidic TiO<sub>2</sub> nanoparticles. The decrease of photoactivity of TiO<sub>2</sub>/Mg<sub>2</sub>Al<sub>1.5</sub> nanocomposite can be caused by screening effect. The nanoparticles of TiO<sub>2</sub> are transparent but prepared nanocomposite is a white powder so it can scatter the light and disable its passage through whole volume of reaction system. In comparison with basic TiO<sub>2</sub> nanoparticles, the immobilization slightly increases photocatalytic activity of TiO<sub>2</sub> incorporated in nanocomposite. Acid Orange 7 is an anionic dye, so oppositely charged surface of LDH leads to higher adsorption of dye on the nanocomposite surface and better accessibility of reactive species directly to dye molecules. Because of the AO7 adsorption, it was necessary to dissolve the composite material in concentrated HNO<sub>3</sub> to remove dye from its surface and obtain the total concentration of unreacted AO7. The decrease of the starting high performance of TiO<sub>2</sub>/Mg<sub>2</sub>Al<sub>1.5</sub> nanocomposite can be explained by adsorption of intermediates.

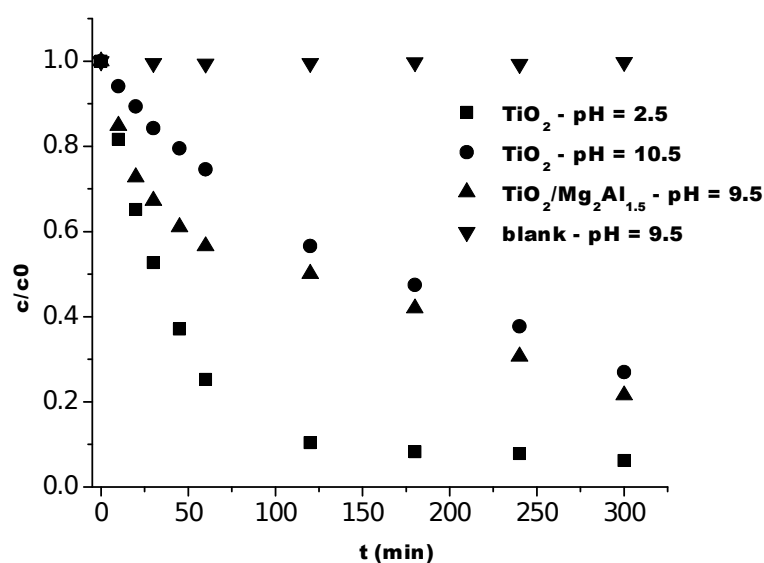


Fig. 37 Dependence of  $c/c_0$  of Acid Orange 7 on time of irradiation for pure  $\text{TiO}_2$  nanoparticles and  $\text{TiO}_2/\text{Mg}_2\text{Al}_{1.5}$  nanocomposite – starting concentration of AO7 =  $5.10^{-5} \text{ mol.L}^{-1}$  and concentration of  $\text{TiO}_2$   $0.5 \text{ g.L}^{-1}$  for all samples

Similar results were obtained for the model compound 4-chlorophenol. The results of its degradation are shown in Fig. 38. The degradation of 4-chlorophenol was slower than degradation of Acid Orange 7 for all the types of used photocatalysts which can be caused by attractive forces between azo dye and photocatalyst. On the other hand, 4-chlorophenol is repulsed by negatively charged surface [221] and 4-CP was not adsorbed on composite surface and the solution was analysed directly after the removal of photocatalyst from the reaction system. The surface of  $\text{TiO}_2$  nanoparticles is stabilized by electrical double layer, in acidic pH the  $\text{TiO}_2$  surface is negatively charged and in basic pH positively charge. By the electrical double layer stabilization, the layer with opposite charge is created on the surface of  $\text{TiO}_2$  and charged particles can repulse 4-chlorophenol which leads to the decrease of degradation rate.

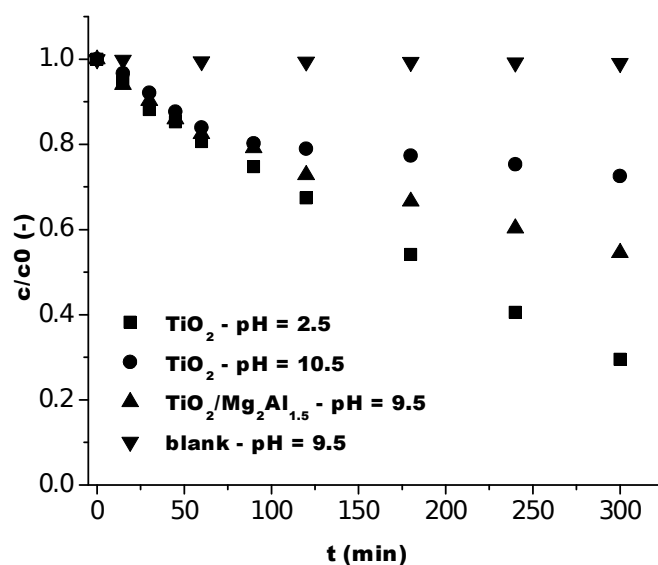


Fig. 38 Dependence of  $c/c_0$  of 4-chlorophenol on time of irradiation for pure  $\text{TiO}_2$  nanoparticles and  $\text{TiO}_2/\text{Mg}_2\text{Al}_{1.5}$  nanocomposite – starting concentration of 4-CP =  $5.10^{-5} \text{ mol.L}^{-1}$  and concentration of  $\text{TiO}_2$   $0.5 \text{ g.L}^{-1}$  for all samples

In Table 9, the degradation rate  $r_i$  in first hour of irradiation is reported for the two organic compounds. The degradation rate  $r_i$  was calculated similarly to degradation rate in chapter 5.1, the calculation was just modified for suspension and  $r_i$  was calculated according following equation:

$$r_i = \left( \frac{dc_{org}}{dt} \right)_i \cdot V \quad (5-3-0)$$

where  $dc_{org}$  is change of concentration in first 60 min,  $dt$  is time period and  $V$  is volume of irradiated solution. It is obvious that Acid Orange 7 is degraded faster in all cases. This can be explained by higher adsorption of AO7 on the surface of photocatalysts and thus its easier accessibility to reactive species. The degradation rate of azo dyes increases with decrease in pH. At  $\text{pH} < 6$ , a strong adsorption of the dye on the  $\text{TiO}_2$  particles is observed as a result of the electrostatic attraction of the positively charged  $\text{TiO}_2$  with the dye [145]. Degradation rate of AO7 on  $\text{TiO}_2$  nanoparticles at pH 2.5 was almost 3 times higher than at pH 10.5.

Table 9 Rate of degradation of model compounds in first 60 minutes of irradiation

Photocatalyst		TiO <sub>2</sub> pH = 2.5	TiO <sub>2</sub> pH = 10.5	TiO <sub>2</sub> /Mg <sub>2</sub> Al <sub>1.5</sub> pH = 9.5
r <sub>i</sub> (mol.min <sup>-1</sup> )	4-chlorophenol	9.46×10 <sup>-9</sup>	8.18×10 <sup>-9</sup>	9.04×10 <sup>-9</sup>
	Acid Orange 7	3.11×10 <sup>-8</sup>	1.27×10 <sup>-8</sup>	1.93×10 <sup>-8</sup>

## 5.4. TiO<sub>2</sub>/SiO<sub>2</sub> composites

For the preparation of new composite materials based on TiO<sub>2</sub>/SiO<sub>2</sub> combination, colloidal suspensions of TiO<sub>2</sub>, which were deeply studied in chapter 5.2, were used. The commercial product Ludox AS30 was used as a source of SiO<sub>2</sub>. The stability of SiO<sub>2</sub> and prepared composite materials is described in following chapters. The prepared composite materials were further characterized and their photocatalytic activity was determined in aqueous and gaseous phase.

### 5.4.1. Stability of colloidal suspensions

#### 5.4.1.1. SiO<sub>2</sub>

As a first step short stability study of commercial SiO<sub>2</sub> colloidal suspension was done similarly as reported in section 5.2. The suspension was diluted to concentration 0.5 g.L<sup>-1</sup> (starting concentration 360 g.L<sup>-1</sup>) in a solution of ammonia (concentration 0.1 mol.L<sup>-1</sup>) to reach the same concentration as for TiO<sub>2</sub> suspension used during the degradation process. This less concentrated suspension was then titrated by HCl (1 or 0.1 mol.L<sup>-1</sup>) to see the influence of different pH on the size, zeta potential of nanoparticles and colloidal stability of suspension. The titration was done every time by fast addition of fixed volume of HCl under ultrasound. Then the pH, size and zeta potential were measured one day and 4 days after addition. The results are shown in Table 10.

We can underline that the simple dilution step induces after 4 days slight aggregation of SiO<sub>2</sub> nanoparticles leading to change of particle size from 21 to 279 nm. It was found that SiO<sub>2</sub> suspension is losing its stability even at low pH (in the range from 2.9 to 1-.9). In all the cases immediately after the HCl addition part of nanoparticles formed agglomerates and after four days aging these agglomerates disintegrated but did not disappear completely. According to the value of zeta potential, the suspension with the highest pH (9.4 and 8.2) should be the most stable but even zeta potential reached value around - 30 mV, colloidal particles at pH 9.4 and 8.2 started to form agglomerates, which means that diluted SiO<sub>2</sub> has to be used immediately for the composite preparation and it cannot be stored in diluted form.

Table 10: Titration of colloidal SiO<sub>2</sub> nanoparticles by HCl 1 and 0.1 mol.L<sup>-1</sup> and its influence on the size and zeta potential of SiO<sub>2</sub> nanoparticles.

titration by 1 mol.L <sup>-1</sup> HCl		day 1			day 4		
		Size		ζ	Size		ζ
V (mL)	pH	(nm)	represented	(mV)	(nm)	represented	(mV)
0	9.4	21	100%	-31	279	4%	-35
0.025	2.9	202	25%	-1	242	15%	-3
		20	75%		22	85%	
0.05	2.5	not possible to measure		-6	194	27%	-7
					18	73%	
0.1	2.2	337	17%	2	308	17%	0
		31	83%		23	83%	
0.2	1.9	not possible to measure		4	349	12%	3
					22	88%	
titration by 0.1 mol.L <sup>-1</sup> HCl		day 1			day 4		
		Size		ζ	Size		ζ
V (mL)	pH	(nm)	represented	(mV)	(nm)	represented	(mV)
0.01	8.2	258	34%	-31	not possible to measure		-33
		20	66%				

0.02	6.2	261	50%	-26	302	40%	-19
		20	50%		21	60%	
0.1	5.0	365	36%	-13	358	38%	-10
		20	64%		21	62%	
0.2	3.5	338	50%	-5	255	30%	-5
		21	50%		22	70%	

#### 5.4.1.2. $TiO_2/SiO_2$ composites

The stability test was also performed on suspension obtained by mixing  $SiO_2$  and  $TiO_2$  (preparation described in chapter 4.1.4.2). During the preparation the pH changed according to the concentration of  $SiO_2$  added to  $TiO_2$  suspension. Results are shown in Table 11.

Table 11:  $TiO_2/SiO_2$  nanocomposites colloidal suspensions: pH, size, and zeta potential measurement

Aging at room temperature				0 day			7 days		
$TiO_2/SiO_2$	pH	c ( $SiO_2$ )	c ( $TiO_2$ )	Size		$\zeta$	Size		$\zeta$
		(g.L <sup>-1</sup> )		(nm)	represented	(mV)	(nm)	represented	(mV)
1:0	2.9	0	0.5	14	100%	44	14	100%	43
1:1	4.6	0.25	0.25	too large particles		14	too large particles		-13
1:2	6.6	0.33	0.17	127	100%	-31	too large particles		-19
1:5	8.0	0.42	0.08	59	100%	-37	too large particles		-23
1:10	8.6	0.45	0.05	27	40%	-45	too large particles		-15

				110	60%				
0:1	9.4	0.5	0	21	100%	-31	289	4%	-33
							22	96%	

The results show that the higher the  $\text{TiO}_2/\text{SiO}_2$  ratio the lower the pH value. All the mixing led to a particle size increase and aggregation just after addition and also after aging of the suspension. To limit this phenomenon, the preparation of the composite suspension with higher concentration of both components was carried out. For the establishing the optimal way of preparation the ratio of  $\text{TiO}_2/\text{SiO}_2$  1:1 was chosen as this ratio had the lowest stability in previous test. The different ways of mixing were tested. Nine different samples were prepared, the differences in preparation way and final pH are shown in Table 12.

Table 12 TiO<sub>2</sub>/SiO<sub>2</sub> 1:1 composites prepared by modified ways

label	TiO <sub>2</sub> /SiO <sub>2</sub> 1:1 - sample description	pH
1	5 mL SiO <sub>2</sub> + 5 mL TiO <sub>2</sub> , sonication only during addition (used in Table 11)	3.5
2	5 mL TiO <sub>2</sub> + 5 mL SiO <sub>2</sub> , sonication only during addition	3.6
3	5 mL SiO <sub>2</sub> + 5 mL TiO <sub>2</sub> (pH - 1, V of HCl 1 M added 0.2 mL), sonication only during addition	1.8
4	5 mL SiO <sub>2</sub> (pH - 1.2, V HCl 1M added 0.3 mL) + 5 mL TiO <sub>2</sub> , sonication only during addition	2.1
5	5 mL SiO <sub>2</sub> + 5 mL TiO <sub>2</sub> (pH - 11.2, V of NH <sub>3</sub> 2 M added 0.2 mL), sonication only during addition	11.2
6	5 mL SiO <sub>2</sub> + 5 mL TiO <sub>2</sub> , sonication 1 min	3.5
7	5 mL SiO <sub>2</sub> + 5 mL TiO <sub>2</sub> , sonication 5 min	3.5
8	5 mL SiO <sub>2</sub> + 5 mL TiO <sub>2</sub> , sonication 10 min	3.6
9	5 mL SiO <sub>2</sub> + 5 mL TiO <sub>2</sub> , without sonication	3.5

It has to be noted that pH of these composite suspensions did not changed during aging. The size and zeta potential of each prepared composite are summarized in Appendix 1. For the preparation of nanocomposites used for photocatalytic tests, method number 1 was chosen. Interestingly, all composites prepared from suspension of higher concentration showed good stability, changes of particle size and zeta potential were negligible and the suspensions remained clear and transparent whatever the TiO<sub>2</sub>/SiO<sub>2</sub> ratio (Table 13). A slight increase in particles size in suspension is observed – 46, 58 and 65 nm for TiO<sub>2</sub>/SiO<sub>2</sub> ratio of 1:1, 1:5 and 1:10, respectively. In parallel, for the lowest amount of SiO<sub>2</sub> a positive value of zeta potential as for pure TiO<sub>2</sub> is obtained, while the increase of SiO<sub>2</sub> concentration induces an inversion of zeta potential to negative values. Note that aging of the suspension at such concentration (concentration of nanoparticles in suspension higher than 1 g.L<sup>-1</sup>) neither modifies the colloidal stability nor the particle size.

Table 13 Measurement of particle size and zeta potential – composite prepared by addition of SiO<sub>2</sub> to TiO<sub>2</sub>

Aging at room temperature				0 day		7 days		15 days	
TiO <sub>2</sub> /SiO <sub>2</sub>	pH	c (TiO <sub>2</sub> )	c (SiO <sub>2</sub> )	Size	ζ	Size	ζ	Size	ζ
		(g.L <sup>-1</sup> )		(nm)	(mV)	(nm)	(mV)	(nm)	(mV)
1:1	4.0	0.63	0.63	46	26	50	32	48	32
1:5	6.6	0.63	3.15	58	-34	57	-33	62	-28
1:10	8.5	0.63	6.30	65	-38	60	-39	63	-41

#### 5.4.2. Photocatalytic test of prepared composite suspensions

The measurement of photocatalytic activity of prepared composite material was done by determination of degradation of two model compounds, Acid Orange 7 and Methylene Blue. Results of composite materials were compared with results of pure TiO<sub>2</sub>.

##### 5.4.2.1. Degradation of AO7

The results of AO7 degradation are shown in Fig. 39 for alkaline pH and in Fig. 40 for acidic pH. For the photocatalytic tests, two different pHs were chosen – 3.5 and 8.5. pH 3.5 was chosen because it was the acidic pH at which all composites were still stable and this pH allowed an approximate comparison with TiO<sub>2</sub> used for synthesis (pH of TiO<sub>2</sub> 2.5 – at higher pH TiO<sub>2</sub> starts to agglomerate). However, this pH is too low and the pH of water in nature varies from 5-9, pH 8.5 was as a pH closer to conditions in nature. For the comparison of photoactivity of composites at alkaline pH TiO<sub>2</sub> at pH 10.5 was used, at lower pH TiO<sub>2</sub> is losing its stability and starts to agglomerate. Then, TiO<sub>2</sub>/SiO<sub>2</sub> 1:1 appears as a versatile composite efficient for AO7 degradation at both acidic and basic pH. The initial degradation

rate in first 60 minutes,  $r_1$ , is shown in Table 14. It was found that the increasing amount of  $\text{SiO}_2$  in the mixed solution leads to the decrease of photocatalytic activity; the same trend appears for both used pH. This can be explained by the increasing coverage of  $\text{TiO}_2$  surface by  $\text{SiO}_2$  which lead to the decrease of active surface. The increase of pH (from 8.5 to 3.5) leads to decrease of photoactivity too. This could be explained by the lower adsorption of AO7 on the surface of photocatalyst at neutral pH [222]. AO7 is negatively charged and as the zeta potential changes to negative values, the amount of AO7 adsorbed decreases.

$\text{TiO}_2:\text{SiO}_2$  1:1 showed faster degradation rate at alkaline pH than pure  $\text{TiO}_2$  (pH 10.5), the other samples showed lower photoactivity at alkaline pH. Similarly, for acidic pH,  $\text{TiO}_2:\text{SiO}_2$  1:1 had the same activity as pure  $\text{TiO}_2$  (pH 2.5), with higher amount of  $\text{SiO}_2$  the rate of reaction decreased.  $\text{SiO}_2$  probably increased the adsorption of dye on the photocatalyst surface and with ratio  $\text{TiO}_2:\text{SiO}_2$  1:1, surface of  $\text{TiO}_2$  was not fully covered, so the presence of  $\text{SiO}_2$  increases the degradation, but with increasing ratio the coverage of  $\text{TiO}_2$  surface increases a thus the degradation of AO7 decreases.

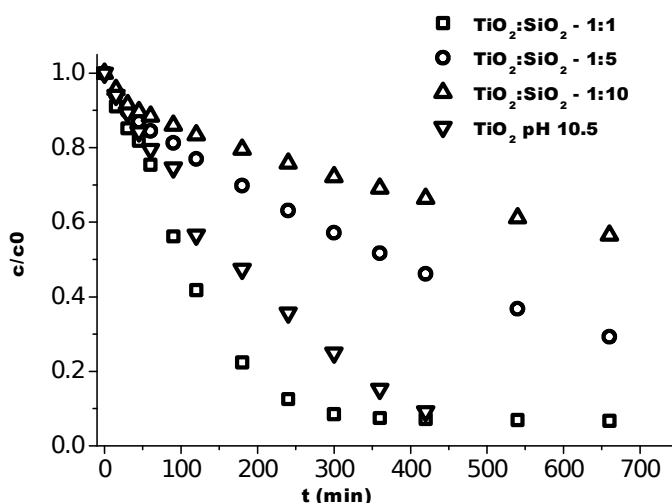


Fig. 39 AO7 degradation by  $\text{TiO}_2/\text{SiO}_2$  composites; pH 8.5,  $\text{TiO}_2$  concentration  $0.5 \text{ g.L}^{-1}$ , initial concentration of AO7  $5 \times 10^{-5} \text{ mol.dm}^{-3}$

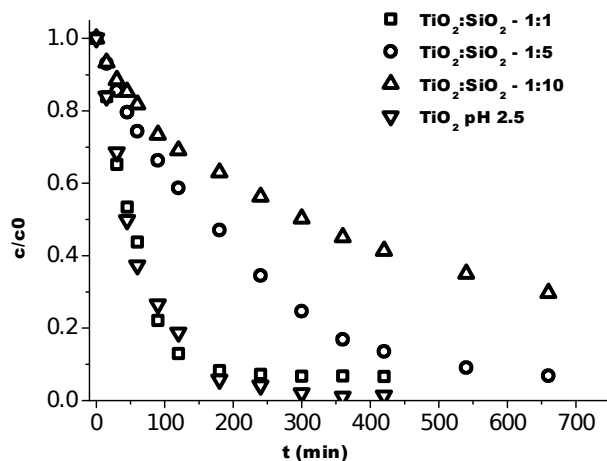


Fig. 40 AO7 degradation by TiO<sub>2</sub>/SiO<sub>2</sub> composites; pH 3.5, TiO<sub>2</sub> concentration 0.5 g.L<sup>-1</sup>, pure TiO<sub>2</sub> – pH 2.5 (not stable at pH 3.5)

#### 5.4.2.2. Degradation of MB

The same measurement was performed for Methylene Blue with the concentration  $5 \times 10^{-5}$  mol.L<sup>-1</sup> (Fig. 41 and Fig. 42). The initial degradation rate in first 30 minutes,  $r_i$ , is shown in Table 14. The degradation of MB was faster than the degradation of AO7. In the case of pure TiO<sub>2</sub> the change of pH from acidic to alkaline region had a strong positive effect on MB degradation which can be explained by an increasing adsorption of cationic MB dye on negatively charged TiO<sub>2</sub> in alkaline solutions. In the case of TiO<sub>2</sub>/SiO<sub>2</sub> composites the change of pH had not such influence on the photoactivity. At both pH values, all composites, except ratio TiO<sub>2</sub>:SiO<sub>2</sub> 1:10 in acidic conditions, showed almost the same photoactivity. MB totally disappeared within about 6 hours.

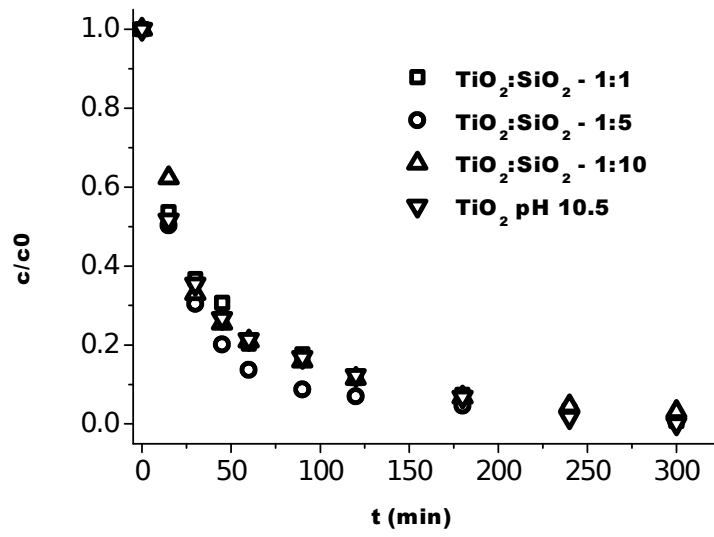


Fig. 41 MB photocatalytic degradation in TiO<sub>2</sub>/SiO<sub>2</sub> composite colloids; TiO<sub>2</sub> concentration 0.5 g.L<sup>-1</sup> pH 8.5

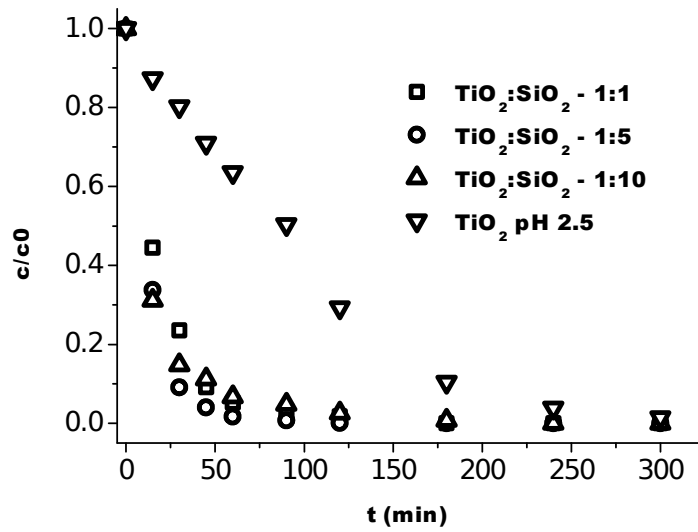


Fig. 42 MB photocatalytic degradation in TiO<sub>2</sub>/SiO<sub>2</sub> composite colloids; TiO<sub>2</sub> concentration 0.5 g.L<sup>-1</sup>, pH 3.5

Table 14 Initial rate of degradation of model compounds in first 60 minutes of irradiation for AO7 and in first 30 minutes for MB

pH	sample	$r_i$ (mol.min <sup>-1</sup> )	
		AO7 in first 60 min	MB in first 30 min
3.5	Pure TiO <sub>2</sub>	$2.82 \times 10^{-8}$	$7.25 \times 10^{-8}$
	TiO <sub>2</sub> /SiO <sub>2</sub> 1:1	$2.66 \times 10^{-8}$	$8.06 \times 10^{-8}$
	TiO <sub>2</sub> /SiO <sub>2</sub> 1:5	$1.28 \times 10^{-8}$	$9.20 \times 10^{-8}$
	TiO <sub>2</sub> /SiO <sub>2</sub> 1:10	$8.66 \times 10^{-8}$	$8.27 \times 10^{-8}$
8.5	Pure TiO <sub>2</sub>	$1.47 \times 10^{-8}$	$1.08 \times 10^{-8}$
	TiO <sub>2</sub> /SiO <sub>2</sub> 1:1	$1.22 \times 10^{-8}$	$5.57 \times 10^{-8}$
	TiO <sub>2</sub> /SiO <sub>2</sub> 1:5	$7.48 \times 10^{-9}$	$7.15 \times 10^{-9}$
	TiO <sub>2</sub> /SiO <sub>2</sub> 1:10	$6.10 \times 10^{-9}$	$7.00 \times 10^{-9}$

In Table 14 shows the values of initial degradation rates of AO7 and MB by all prepared composites at 2 different pHs. We can see that the degradation rate of MB is all cases higher than the one of AO7. This can be caused by higher adsorption of MB on the composite nanoparticles. The degradation rate of AO7, unlike MB, is influenced by the content of SiO<sub>2</sub> in the composite and its value is decreasing with increasing amount of SiO<sub>2</sub>. In this part, it appears that addition of a low amount of SiO<sub>2</sub> in TiO<sub>2</sub> colloidal suspension leads to an efficient composite with interesting photoactivity in both acidic and basic conditions.

#### 5.4.3. Immobilisation of TiO<sub>2</sub>/SiO<sub>2</sub> composites

Further four different powders of TiO<sub>2</sub>/SiO<sub>2</sub> composite materials were prepared:

- TiO<sub>2</sub>/SiO<sub>2</sub> 1:1 (D),
- TiO<sub>2</sub>/SiO<sub>2</sub> 1:10 (D),
- TiO<sub>2</sub>/SiO<sub>2</sub> 1:1 (P),
- TiO<sub>2</sub>/SiO<sub>2</sub> 1:10 (P),

where D means samples prepared by direct coagulation of mixed precursor suspensions, and P means samples prepared from TiO<sub>2</sub> dried powder and SiO<sub>2</sub> suspension. The method of powders of TiO<sub>2</sub>/SiO<sub>2</sub> composite preparation is described in chapter 4.1.4.3.

#### 5.4.3.1. Characterization of prepared powder TiO<sub>2</sub>/SiO<sub>2</sub> composites

Composition analysis of all prepared composites was performed by XRF measurement; the results are shown in Table 15. It was found that composite prepared from not washed TiO<sub>2</sub> powder (samples marked as P<sub>0</sub>) contains high amount of Na in their structure. This amount can strongly influence the required properties. XRD confirmed that in samples prepared from powder TiO<sub>2</sub>, Na is in the form of crystalline NaCl (see Fig. 43). The presence of NaCl in the sample had not any influence on the resulting structure and crystallinity of composite, in both cases samples contained only amorphous phase and no crystalline TiO<sub>2</sub> was observed. However, Na presence can lead to the decrease of the photocatalytic activity of photocatalyst because it causes the faster recombination of the electron and the positive hole [223] so it is necessary to remove it. The synthesis was thus repeated to obtain the composite without the NaCl contamination. The step of washing of coagulated TiO<sub>2</sub> before the synthesis was thus included in the preparation and the Na content was significantly decreased in the composites marked (P).

Table 15 Composition of composites prepared by direct coagulation measured by XRF

Sample	TiO <sub>2</sub> content (wt.%)	SiO <sub>2</sub> content (wt.%)	Na content (wt.%)	Ratio TiO <sub>2</sub> /SiO <sub>2</sub>
Pure TiO <sub>2</sub>	98.22	-	1.71	1:0
TiO <sub>2</sub> /SiO <sub>2</sub> 1:1 (P <sub>0</sub> )	25.08	27.60	18.91	1:1.10
TiO <sub>2</sub> /SiO <sub>2</sub> 1:10 (P <sub>0</sub> )	8.47	66.58	9.65	1:7.86
TiO <sub>2</sub> /SiO <sub>2</sub> 1:1 (P)	50.21	48.17	1.56	1:0.96
TiO <sub>2</sub> /SiO <sub>2</sub> 1:10 (P)	10.97	86.88	1.73	1:7.92
TiO <sub>2</sub> /SiO <sub>2</sub> 1:1 (D)	60.63	38.40	0.84	1:0.63
TiO <sub>2</sub> /SiO <sub>2</sub> 1:10 (D)	17.06	82.27	0.41	1:4.82

The method of preparation from the TiO<sub>2</sub> powder (P) leads to the composite with higher SiO<sub>2</sub> content. These composites contain SiO<sub>2</sub> in the amount which is very close to the theoretical ratios - 1:1 and 1:10. In the case of direct coagulation, the final ratio TiO<sub>2</sub>/SiO<sub>2</sub> in the composites is about half of a theoretical value. To obtain better insight into the structure of TiO<sub>2</sub> and TiO<sub>2</sub>/SiO<sub>2</sub> composites, XRD analyses was performed (see Fig. 43 and Fig. 44). The X-ray patterns show that pure TiO<sub>2</sub> as well as composite prepared from dried TiO<sub>2</sub> powder are amorphous. The presence of TiO<sub>2</sub> in anatase modification was found only in two samples - TiO<sub>2</sub>/SiO<sub>2</sub> 1:1 (D) and TiO<sub>2</sub>/SiO<sub>2</sub> 1:10 (D) – which were prepared by direct coagulation of composites from colloidal suspensions of both precursors. The size of anatase crystals in samples (D) was about 3 nm in both cases. The results of XRD analysis are summarized in Table 16.

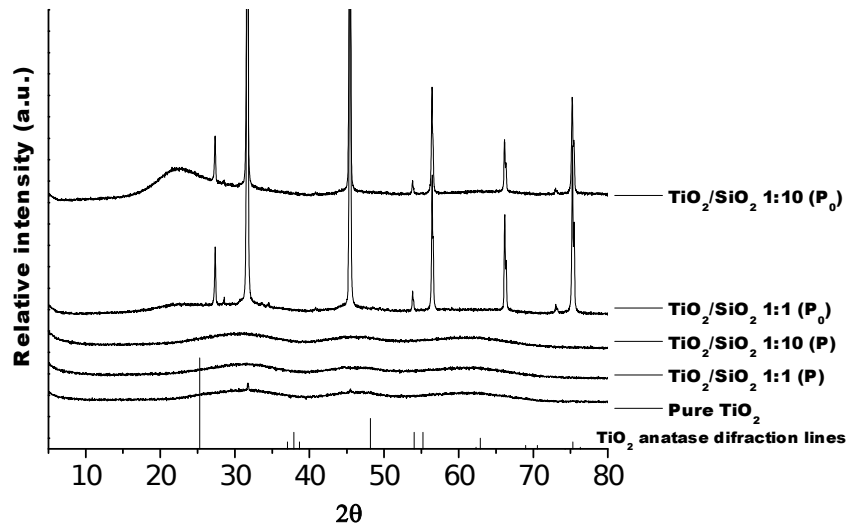


Fig. 43 XRD results of prepared  $\text{TiO}_2$  powder and  $\text{TiO}_2/\text{SiO}_2$  composites

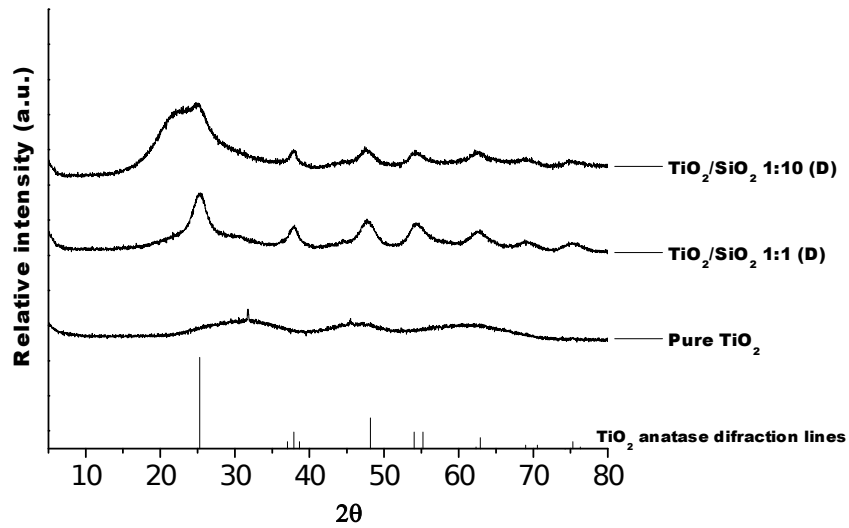


Fig. 44 XRD results of prepared  $\text{TiO}_2$  powder and  $\text{TiO}_2/\text{SiO}_2$  composites

Table 16 XRD results of prepared  $\text{TiO}_2$  powder and  $\text{TiO}_2/\text{SiO}_2$  composites with different mass ratio.

Sample	XRD analysis	Crystal size (nm)
Pure $\text{TiO}_2$	Amorphous $\text{TiO}_2$	-
$\text{TiO}_2/\text{SiO}_2$ 1:1 (P)	Amorphous $\text{TiO}_2$	-
$\text{TiO}_2/\text{SiO}_2$ 1:10 (P)	Amorphous $\text{TiO}_2$	-
$\text{TiO}_2/\text{SiO}_2$ 1:1 (D)	$\text{TiO}_2$ in anatase modification	$3.4 \pm 1$
$\text{TiO}_2/\text{SiO}_2$ 1:10 (D)	$\text{TiO}_2$ in anatase modification	$2.6 \pm 0.8$

#### 5.4.3.2. Photocatalytic activity of composite layers

The photocatalytic activity of the prepared TiO<sub>2</sub>/SiO<sub>2</sub> was measured by the degradation of a gaseous model compound, hexane. Gas flowing through apparatus was periodically analysed using gas chromatograph. Fig. 45 shows photocatalytic degradation of hexane (in fact hexane concentration in the flowing gas as a function of time when there are several regimes) using pure TiO<sub>2</sub> powder layer.

It was found that hexane is slightly adsorbed on TiO<sub>2</sub> surface in dark. However, the decrease of hexane concentration seems to be permanent when the layer is present in reactor, the 7% decrease is constant for 20 minutes. Another measurement in dark was performed and it was found that even after 100 min the concentration of hexane in reactor outlet is lower than inlet concentration. This can mean that the direct chemical reaction of hexane with photocatalyst of large surface area (291 m<sup>2</sup>.g<sup>-1</sup>) takes place in our system. The test of photocatalytic activity was started when the concentration of hexane was stable at outlet of the reactor (regime UV on). When the irradiation is started, the concentration of hexane in the outlet is observed. Prepared pure TiO<sub>2</sub> exhibited 30 % of total decrease of hexane concentration. However, this total decrease of hexane concentration consists of the two parts: i) photocatalytic degradation and ii) adsorption and chemical reaction of hexane on the photocatalyst surface. It can be concluded that 7 % of hexane is adsorbed or react chemically on the TiO<sub>2</sub> surface and remaining 23 % is photocatalytically degraded. Table 17 summarises the decrease of hexane concentration and various photocatalytic degradation rate related to irradiated surface area. The degradation rate was calculated according following formula:

$$r_i = \frac{\dot{V} \cdot c}{V_m \cdot A} \quad (5-4-0)$$

where  $\dot{V}$  is flow of gas through the reactor [L.s<sup>-1</sup>], c is concentration of hexane in ppm, A is the geometrical area of the irradiated photocatalyst layer [cm<sup>2</sup>] and V<sub>m</sub> is the molar volume of the 1 mol of hexane [L].

Table 17 Decrease of hexane concentration during gas phase photocatalytic experiments

Sample	Total decrease of hexane (%)	Adsorption or chemical reaction of hexane (%)	Photocatalytically degraded hexane (%)	r <sub>i</sub> (mol.cm <sup>-2</sup> .s <sup>-1</sup> )
Pure TiO <sub>2</sub>	30	7	23	3.2×10 <sup>-12</sup>
TiO <sub>2</sub> /SiO <sub>2</sub> 1:1 (P)	16	13	~ 3	< 3.9 ×10 <sup>-13</sup>
TiO <sub>2</sub> /SiO <sub>2</sub> 1:10 (P)	27	24	~ 3	< 3.8 ×10 <sup>-13</sup>
TiO <sub>2</sub> /SiO <sub>2</sub> 1:1 (D)	35	5	30	4.0×10 <sup>-12</sup>
TiO <sub>2</sub> /SiO <sub>2</sub> 1:10 (D)	26	3	23	3.1×10 <sup>-12</sup>

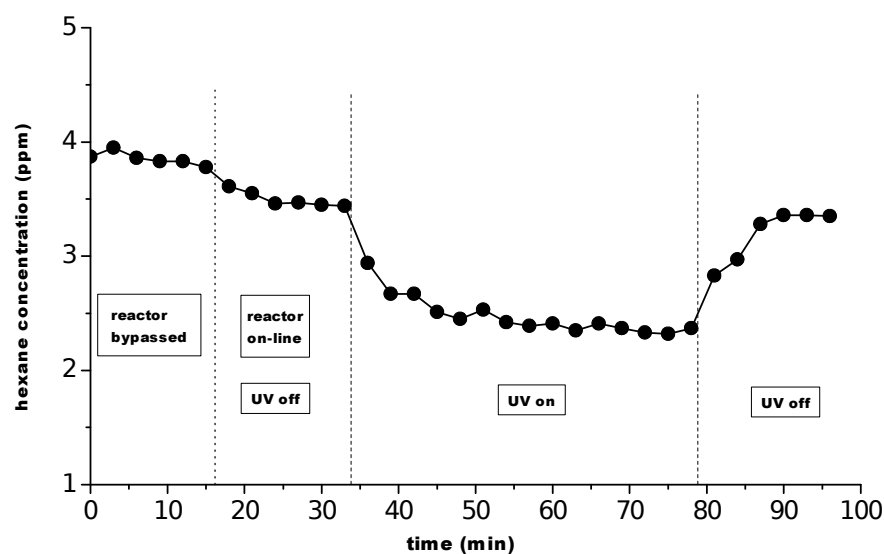


Fig. 45 Photocatalytic degradation of hexane using pure TiO<sub>2</sub> powder layer (hexane concentration was measured in the flowing gas as a function of time for several regimes, namely – Bypass of the reactor, Reactor UV lights OFF, Reactor UV lights ON, Reactor UV lights OFF).

Under the same conditions, we measured the photocatalytic activity of prepared composites. The results are shown in Fig. 46 and Fig. 47 for composites (D) prepared from TiO<sub>2</sub> powder and SiO<sub>2</sub> suspension and in Fig. 48 and Fig. 49 for composites prepared by direct mixing of precursor suspensions (preparations described in detail in 4.1.4.3).

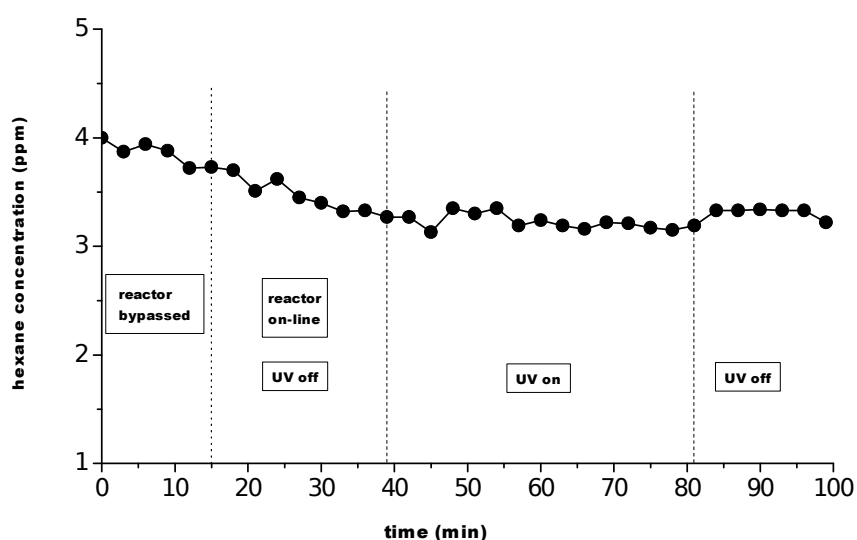


Fig. 46 Photocatalytic degradation of hexane using composite TiO<sub>2</sub>/SiO<sub>2</sub> 1:1 (P) prepared from TiO<sub>2</sub> dried powder and SiO<sub>2</sub> suspension (the same regime of measurement as described in Fig. 45).

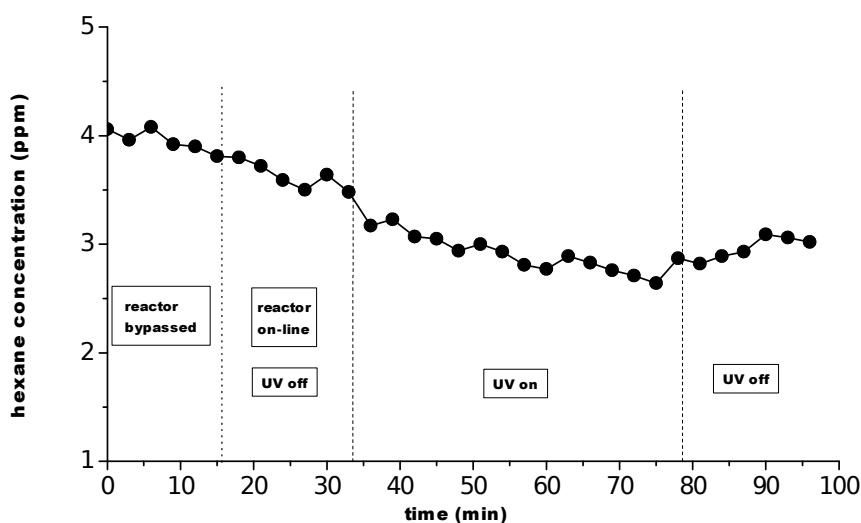


Fig. 47 Photocatalytic degradation of hexane using composite  $\text{TiO}_2/\text{SiO}_2$  1:10 (P) prepared from  $\text{TiO}_2$  dried powder and  $\text{SiO}_2$  suspension (the same regime of measurement as described in Fig. 45).

In the Fig. 46 and Fig. 47,m we can see the decrease of hexane concentration; however, in the same time scale as for pure  $\text{TiO}_2$  the constant hexane concentration in outlet of the reactor in dark was not reached and no significant changes were observed after the irradiation was started. When the light was turned off again, the hexane concentration increased only about 3-4 % in both cases, which means that these samples do not exhibit sufficient photocatalytic activity.

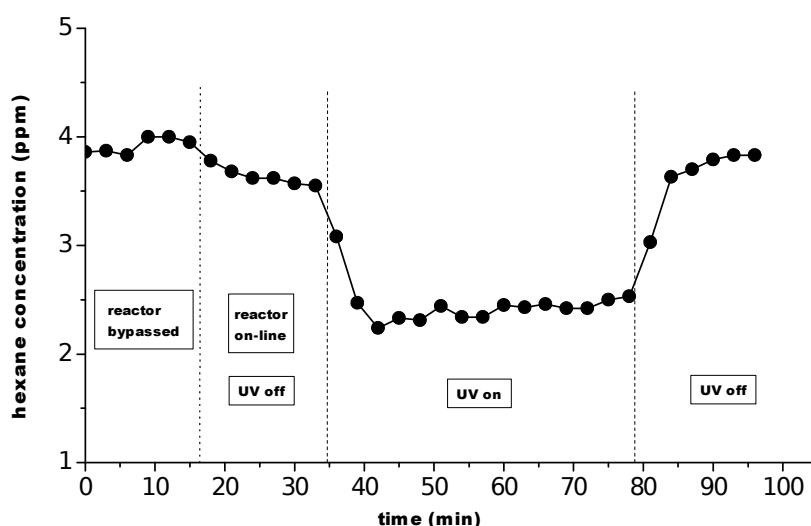


Fig. 48 Photocatalytic degradation of hexane using composite  $\text{TiO}_2/\text{SiO}_2$  1:1 (D) prepared by direct coagulation of mixed precursor suspensions (same regime of measurement as described in Fig. 45).

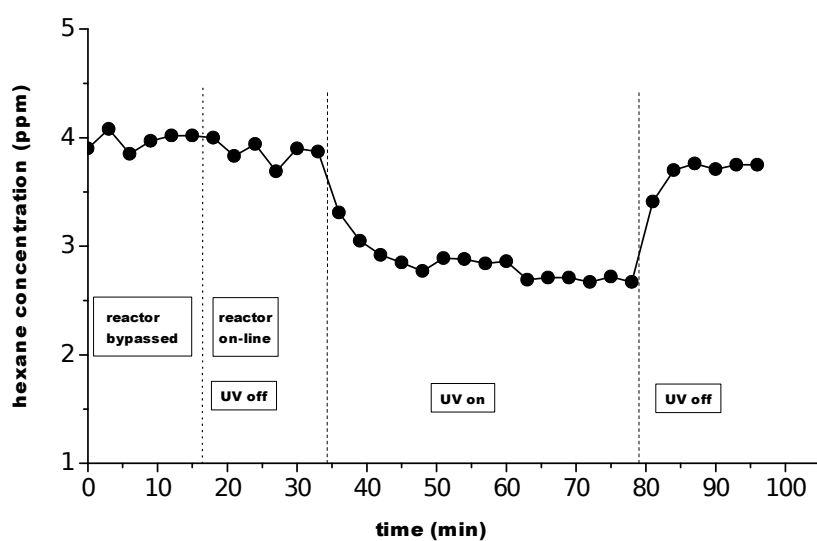


Fig. 49 Photocatalytic degradation of hexane using composite  $\text{TiO}_2/\text{SiO}_2$  1:10 (D) prepared by direct coagulation of mixed precursor suspensions (same regime of measurement as described in Fig. 45).

The behaviour of samples prepared by direct coagulation (D) is similar to behaviour of pure  $\text{TiO}_2$  (Fig. 48 and Fig. 49). The hexane concentration slightly decreased when the hexane passed through the reactor with UV light off. After light is turned on, the decrease of hexane concentration was significant (total hexane concentration decrease about 35%). When the light was turned off again, the hexane concentration increased to the almost the same value as in the second step of measurement (regime reactor online UV off).

#### 5.4.4. Relation between surface morphology and photocatalytic activity

The composites prepared from  $\text{TiO}_2$  dried powder and  $\text{SiO}_2$  suspension ( $\text{TiO}_2/\text{SiO}_2$  1:1 (P) and  $\text{TiO}_2/\text{SiO}_2$  1:10 (P)) did not show almost any photocatalytic activity. Indeed under UV, it seems that mainly additional adsorption on the photocatalyst surface was observed. This can be explained by the aggregation of amorphous  $\text{TiO}_2$  nanoparticle and coverage of the surface of  $\text{TiO}_2$  particles by  $\text{SiO}_2$  [224],  $\text{TiO}_2$  particles are thus present mainly in the bulk of composite.

On the other side, composites prepared by the coagulation of mixed  $\text{TiO}_2$  and  $\text{SiO}_2$  suspensions ( $\text{TiO}_2/\text{SiO}_2$  1:1 (D) and  $\text{TiO}_2/\text{SiO}_2$  1:10 (D)) are photocatalytically active. The photocatalytic activity of composite  $\text{TiO}_2/\text{SiO}_2$  1:1 (D) was even higher than of pure  $\text{TiO}_2$ ; This can be explained by the presence of crystalline  $\text{TiO}_2$  with anatase structure which was confirmed by XRD analysis. Another supporting explanation can be that the surface of  $\text{TiO}_2$  is not completely covered by  $\text{SiO}_2$ . It was confirmed by EDS/SEM analysis that surface of composites contains  $\text{TiO}_2$  and  $\text{SiO}_2$  in ratio 1:0.36 in the case of composite  $\text{TiO}_2/\text{SiO}_2$  1:1 (D) and 1:5.66 in the case of composite  $\text{TiO}_2/\text{SiO}_2$  1:10 (D). The possibility of  $\text{SiO}_2$  particles

covered by  $\text{TiO}_2$  is more presumable than in the case of composites marked as (P) because the suspensions contained the nanoparticles of similar size ( $\text{SiO}_2$  21 nm,  $\text{TiO}_2$  14 nm). If we compare the results of  $\text{TiO}_2/\text{SiO}_2$  1:1 (D) and  $\text{TiO}_2/\text{SiO}_2$  1:10 (D) composites we can see that the sample  $\text{TiO}_2/\text{SiO}_2$  1:1 (D) shows higher conversion than the sample  $\text{TiO}_2/\text{SiO}_2$  1:10 (D), evidencing that the increase of  $\text{SiO}_2$  amount in the composite decreases the photocatalytic activity. This phenomenon could be explained by a larger portion of  $\text{TiO}_2$  surface covered by  $\text{SiO}_2$  nanoparticles resulting in the decrease of accessible active surface of  $\text{TiO}_2$ .

The SEM images of pure  $\text{TiO}_2$  and  $\text{TiO}_2/\text{SiO}_2$  composites (D) are shown in Fig. 50, Fig. 51 and Fig. 52. It was found that after coagulation  $\text{TiO}_2$  formed agglomerates which are composed of particles of about 1-6  $\mu\text{m}$  in size (Fig. 50). In the case of composite (Fig. 51, Fig. 52), the morphology is very similar to the morphology of pure  $\text{TiO}_2$ . It only seems that composite samples contain higher amount of porous aggregates than the pure  $\text{TiO}_2$  or we can assume that the particles of  $\text{TiO}_2$  are covered by porous layer formed by  $\text{SiO}_2$  nanoparticles. Nevertheless, it is impossible to distinguish which one are  $\text{TiO}_2$  and  $\text{SiO}_2$ .

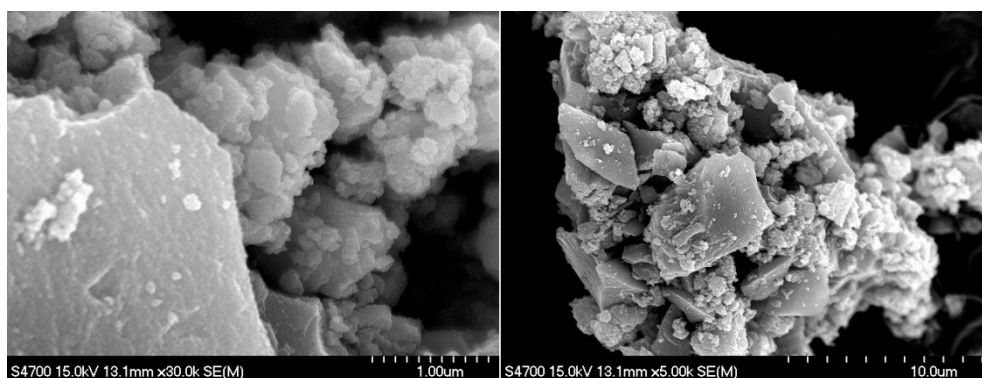


Fig. 50 SEM images of the pure  $\text{TiO}_2$

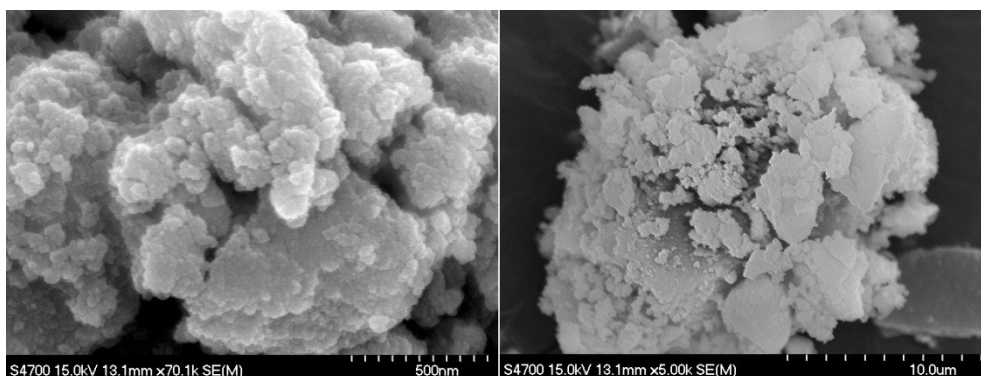


Fig. 51. SEM of the sample  $\text{TiO}_2/\text{SiO}_2$  1:1 (D)

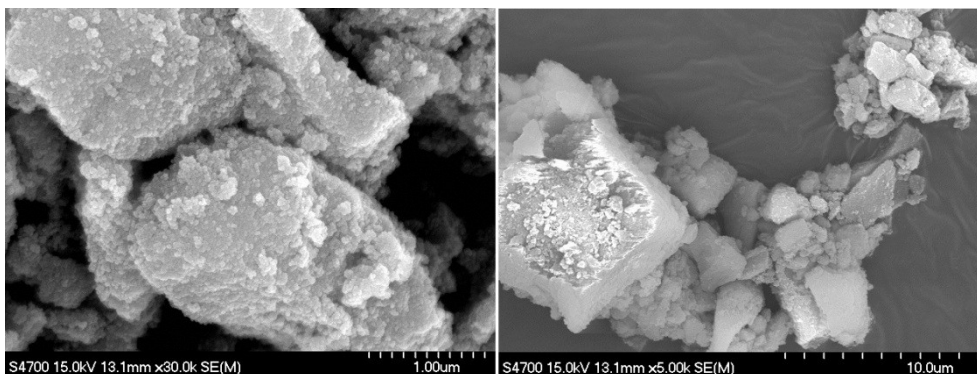


Fig. 52 Fig 3.21. SEM of the sample  $\text{TiO}_2/\text{SiO}_2$  1:10 (D)

The determination of surface composition was performed by scanning electron microscopy equipped with X-ray microanalysis, the results of this analysis are shown in Table 18.

Table 18 Composition of composites prepared by direct coagulation measured by EDS/SEM

Sample	$\text{TiO}_2$ content (wt.%)	$\text{SiO}_2$ content (wt.%)	Ratio $\text{TiO}_2/\text{SiO}_2$ ( $\pm 0.03$ )
$\text{TiO}_2/\text{SiO}_2$ 1:1 (D)	73.57	26.43	1:0.36
$\text{TiO}_2/\text{SiO}_2$ 1:10 (D)	14.95	85.05	1:5.66

It was found that surface layer of composite has different ratio of  $\text{TiO}_2/\text{SiO}_2$  than the ratio calculated from the XRF results. According to XRF, sample  $\text{TiO}_2/\text{SiO}_2$  1:1 (D) has the  $\text{TiO}_2/\text{SiO}_2$  ratio 1:0.63, however, according to EDS/SEM the surface ratio is only 1:0.36, this composite contains more  $\text{TiO}_2$  on the surface. The opposite trend was observed for sample  $\text{TiO}_2/\text{SiO}_2$  1:10 (D); ratio according XRF was 1:4.82, but according to EDS/SEM the surface ratio was 1:5.66. That means that during synthesis of  $\text{TiO}_2/\text{SiO}_2$  1:10 (D) higher amount of  $\text{SiO}_2$  is present on the composite surface. We confirmed that composite with 1:10 ratio has higher coverage of  $\text{TiO}_2$  surface by  $\text{SiO}_2$  than in the bulk of composite.

BET specific surface area was measured for samples prepared by simultaneous coagulation; the results are shown in Table 19. Coagulation in the presence of  $\text{SiO}_2$  (with ratio 1:1) leads to the increase of surface area about 20%. However, when the coagulation is performed at ratio  $\text{TiO}_2/\text{SiO}_2 = 1:10$  (D) BET decreased about 8%. The porous volume of both prepared composites significantly increased – for sample  $\text{TiO}_2/\text{SiO}_2$  1:1 (D) the increase was almost two times (1.9x higher) and for sample  $\text{TiO}_2/\text{SiO}_2$  1:10 (D) more than two times (2.2x higher). This increase of porous volume is caused by an increasing volume of mesopores in the composites structure (as shown in Table 19).

Table 19 Surface area and Porous volume of pure  $\text{TiO}_2$ ,  $\text{TiO}_2/\text{SiO}_2$  1:1 (D) and  $\text{TiO}_2/\text{SiO}_2$  1:10 (D)

Sample	S BET ( $\text{m}^2 \cdot \text{g}^{-1}$ ) $\pm 2$	Porous Volume ( $\text{cm}^3 \cdot \text{g}^{-1}$ )	Volume of Micropores ( $\text{cm}^3 \cdot \text{g}^{-1}$ )
Pure $\text{TiO}_2$	291	0.210	0.0215
$\text{TiO}_2/\text{SiO}_2$ 1:1 (D)	352	0.398	0.0156
$\text{TiO}_2/\text{SiO}_2$ 1:10 (D)	269	0.472	0.0108

The pore distribution curve is shown in Fig. 53. Pure  $\text{TiO}_2$  contains micropores (their volume is  $0.0215 \text{ cm}^3 \cdot \text{g}^{-1}$  which was about 10% of whole porous volume in this sample) and mesopores with diameter 3.5-4 nm. Addition of  $\text{SiO}_2$  leads to the decrease of amount of micropores, volume of micropores in  $\text{TiO}_2/\text{SiO}_2$  1:1 (D) was  $0.0156 \text{ cm}^3 \cdot \text{g}^{-1}$  and this sample contained mesopores with diameter 4-4.5 nm. The highest decrease in micropore volume was observed for sample  $\text{TiO}_2/\text{SiO}_2$  1:10 (D) –  $0.0108 \text{ cm}^3 \cdot \text{g}^{-1}$ , mesopores in this sample had diameter 8-8.5 nm. From these results, we can assume that pure  $\text{TiO}_2$  after coagulation forms the mesoporous structure with high content of micropores which contributed in high surface area  $291 \text{ m}^2 \cdot \text{g}^{-1}$ . Coagulation in the presence of  $\text{SiO}_2$  in ratio 1:1 leads to slight decrease of volume of micropores, however, the whole volume of pores increased about two times. This can be explained by partly covered  $\text{TiO}_2$  surface by  $\text{SiO}_2$  which could cause the deepening of mesopores and partial filling of micropores. For the ratio 1:10 ( $\text{TiO}_2/\text{SiO}_2$ ), the noticeable loss of microporosity was observed, volume of micropores was  $0.0108 \text{ cm}^3 \cdot \text{g}^{-1}$ , which is only 2 % of whole porous volume. In this case,  $\text{SiO}_2$  covered bigger area of  $\text{TiO}_2$  surface and even the micropores. So the BET measurement of surface mainly describes the surface properties of  $\text{SiO}_2$  which has mesoporous structure with bigger pores than  $\text{TiO}_2$  and thus the surface area of whole composite decreased.

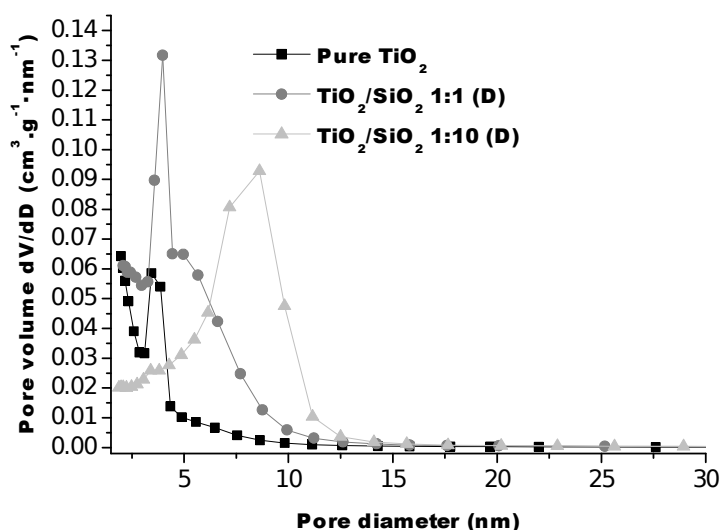


Fig. 53 Pore distribution curves of pure  $\text{TiO}_2$  and  $\text{TiO}_2/\text{SiO}_2$  composites

## 5.5. ZnCr-LDH

Since ZnCr based LDH compound was reported as an efficient photocatalyst for visible light water splitting, in this part, carbonate intercalated ZnCr-LDH has been prepared and tested for degradation of Acid Orange 7. Evolution of the physico-chemical features and photocatalytic properties of  $Zn_2CrCO_3$  phase, calcined at different temperatures were deeply studied. Indeed when  $Zn_2CrCO_3$  LDH was exposed to thermal treatment, hydroxylated structure of LDH collapses leading to mixed oxides containing ZnO which is known for its quite high photocatalytic activity [225].

### 5.5.1. Characterization of prepared $Zn_2CrCO_3$ -LDH

Carbonate intercalated LDH phases were considered as precursors of choice to produce derived mixed oxides due to the carbonate anions full decomposition at rather low temperatures.  $Zn_2CrCO_3$  was successfully prepared by coprecipitation of  $Zn_2CrCl$  followed by anionic exchange with carbonate anions. This two steps method was preferred to the direct carbonate LDH phase preparation to ensure a high crystallinity level of Cr based LDH phase, favoured in rather acidic conditions. Indeed, a high level of LDH crystallinity was reported to enhance the LDH photocatalytic activity [226].

Fig. 54A shows the XRD patterns of  $Zn_2CrCl$  and  $Zn_2CrCO_3$  samples both displaying the typical LDH structure reflections which can be indexed with a hexagonal lattice and R-3m symmetry. The interlamellar distances deduced from the  $00l$  diffraction lines correspond to 0.77 nm and 0.76 nm respectively for  $Zn_2CrCl$  and  $Zn_2CrCO_3$  which is in good agreement with the values reported in the literature. Note that a molar ratio of 2.3 between Zn and Cr into  $Zn_2CrCO_3$  was determined by EDS. This value is in quite good agreement with the  $M^{II}/M^{III}$  ratio (2.0) of the starting metal salt solution involved in the coprecipitation process. Concerning the interlayer anion, the replacement of chloride by carbonate anions was more clearly evidenced on the FTIR spectra (Fig. 54B) by the presence after the anionic exchange reaction of an intense band at  $1361\text{ cm}^{-1}$  characteristic of carbonate anion ( $\nu_{CO_3}$ ), all the others bands characteristic of LDH layers such as  $\nu_{OH}$  ( $3400\text{ cm}^{-1}$ ),  $\nu_{H_2O}$  ( $1618\text{ cm}^{-1}$ ),  $\nu_{MO}$  ( $720, 570$  and  $508\text{ cm}^{-1}$ ), being maintained.

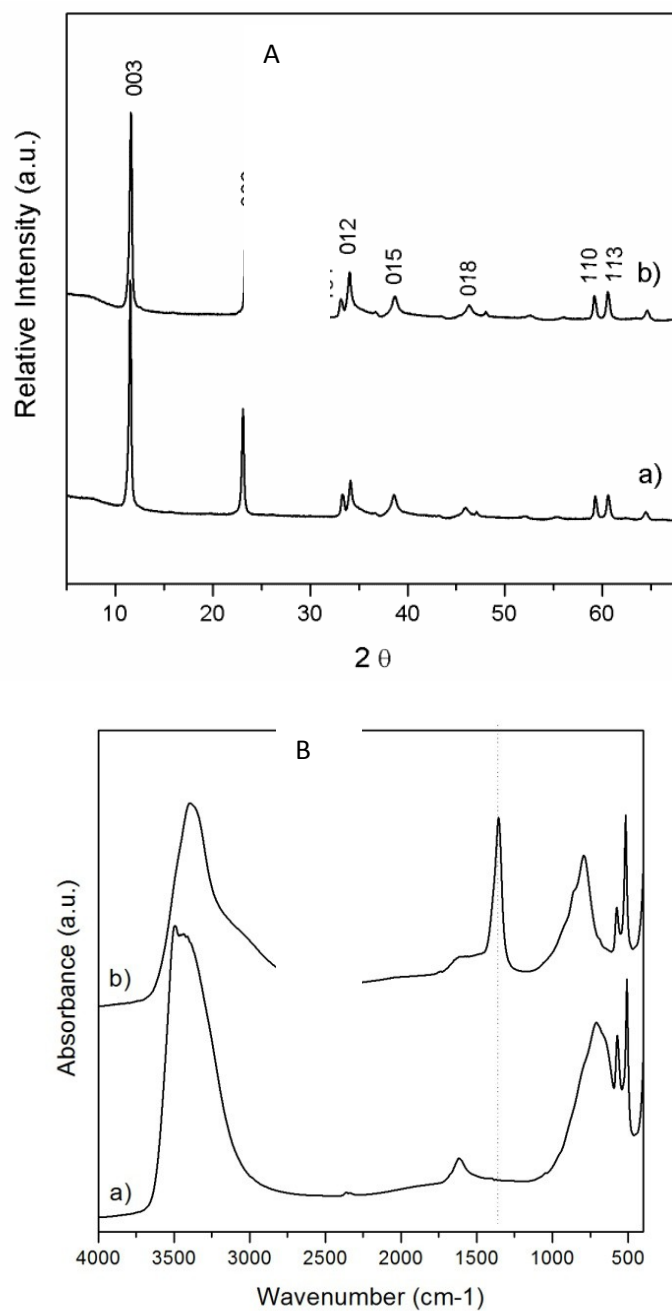
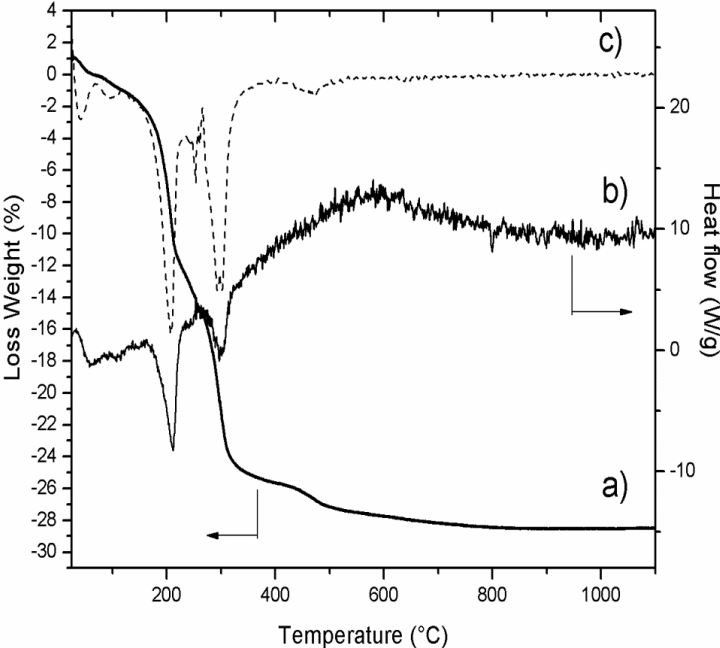


Fig. 54 A XRD patterns and B FTIR spectra of a)  $\text{Zn}_2\text{CrCl}$  and b)  $\text{Zn}_2\text{CrCO}_3$

To get further insight on the thermal behaviour of LDH precursor compound, both TGA/DTG and high temperature in situ XRD were studied. The TGA curve clearly reveals on Fig. 55A, four main mass loss steps. The first one between 25°C and 150°C is correlated to the loss of surface adsorbed and interlayer water. The next two endothermic mass losses are partially overlapped with the main loss weight (24.2%/28.5%) corresponding to dehydroxylation of the hydroxide layers and partial anion decomposition. Indeed the final weight loss above 375 °C (3.1%) is less than what could be expected for complete anion decomposition (9%) according to the theoretical formula. The XRD patterns recorded in situ at different temperatures (Fig. 55B) in quite similar TGA conditions, evidence that in the

range of temperature between 30 °C and 150 °C, no significant change in the patterns are noticed evidencing that the removal of water molecules from the  $Zn_2CrCO_3$  LDH matrix and the moderate thermal treatment do not strongly modify the interlayer domain structure.

A



B

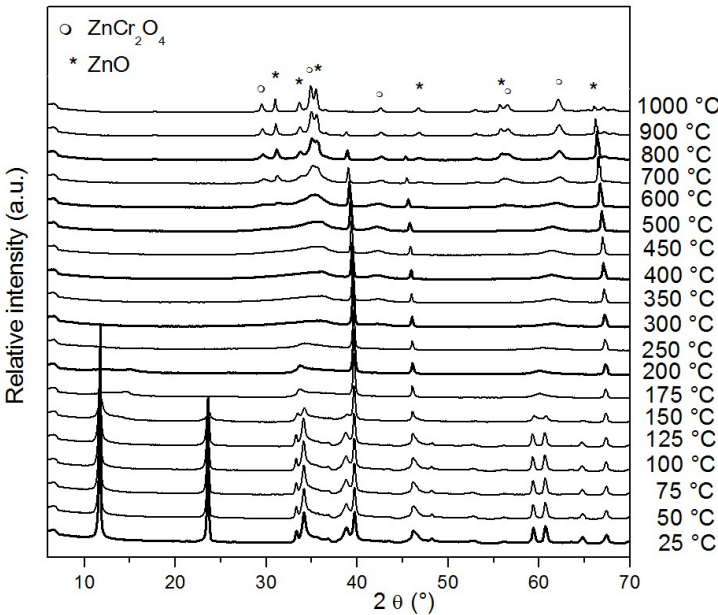


Fig. 55 A) Thermogravimetric (a), heat flow (b) and DTG (c) curves and B) high temperature in-situ PXRD of  $\text{Zn}_2\text{CrCO}_3$

Above  $150\text{ }^\circ\text{C}$ , the in-situ PXRD patterns display very broad and ill-defined XRD peaks evidencing that such temperature corresponding to the beginning of the dehydroxylation, induces the collapse of the dehydrated  $\text{Zn}_2\text{CrCO}_3$  which is converted to an amorphous phase. Characteristic diffraction lines of mixed oxides and oxides ( $\text{ZnCr}_2\text{O}_4$  and  $\text{ZnO}$ ) appear in the patterns for calcination of the sample above  $600\text{ }^\circ\text{C}$ . These latter become more intense and thin upon a further increase of the temperature causing higher crystallization of  $\text{ZnCr}_2\text{O}_4$  and  $\text{ZnO}$ . In parallel, PXRD patterns were also recorded classically on samples calcined at fixed temperature for 4h. It is noteworthy that in this thermal treatment conditions, oxides and mixed oxides crystallize at lower temperatures. At  $500\text{ }^\circ\text{C}$ , rather thin and well-defined diffraction lines of  $\text{ZnCr}_2\text{O}_4$  and  $\text{ZnO}$  are already observed due to the prolonged thermal treatment at fixed temperatures which were not yet present in using *in-situ* PXRD measurements.

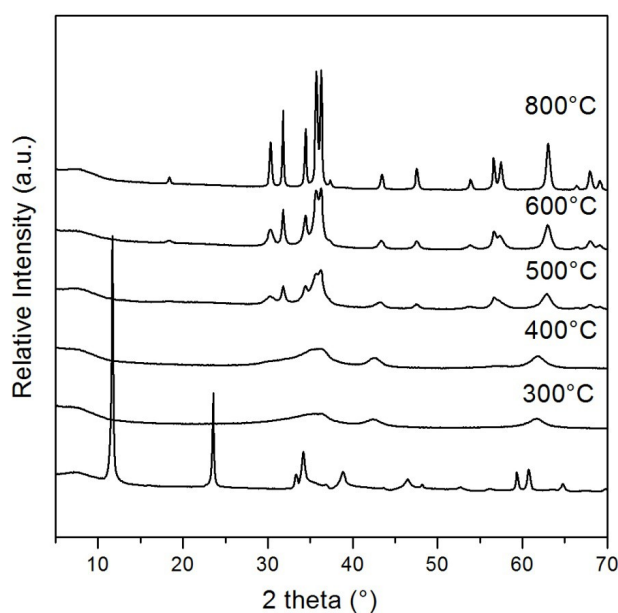


Fig. 56 PXRD patterns of  $\text{Zn}_2\text{CrCO}_3$  and the derived materials after calcination at different temperatures for 4 h

After the calcinations, from FTIR spectra (Fig. 56) we can see the disappearance of band close to  $3400\text{ cm}^{-1}$  and  $1640\text{ cm}^{-1}$  which belongs to OH stretching and  $\text{H}_2\text{O}$  bending modes of water molecules traducing the dehydration and dehydroxylation of the LDH structure. The band at  $1359\text{ cm}^{-1}$ , ascribed to carbonate species which was observed in original LDH, also disappeared due to carbonate anion decomposition at  $600\text{ }^\circ\text{C}$ . Calcination gives also major changes to the spectrum in the  $900\text{-}300\text{ cm}^{-1}$  with main adsorption at  $617\text{ cm}^{-1}$  and  $497\text{ cm}^{-1}$ .

Changes observed in the shape and intensity of the band close to 500  $\text{cm}^{-1}$  are related to crystallization of  $\text{ZnCr}_2\text{O}_4$  spinel [111].

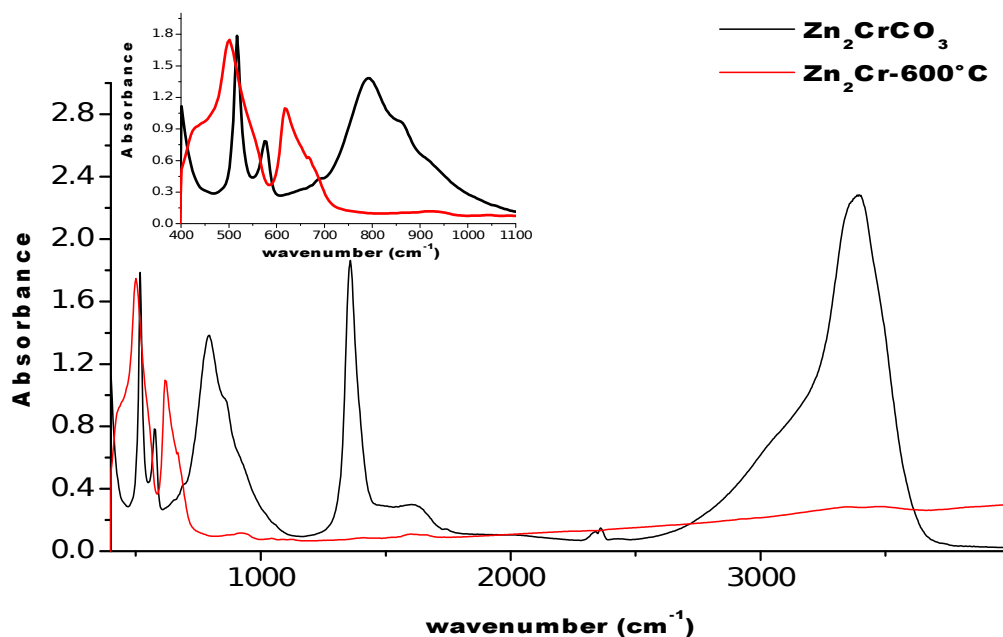


Fig. 57 FTIR spectra of  $\text{Zn}_2\text{CrCO}_3$  and  $\text{Zn}_2\text{Cr-600}^\circ\text{C}$

Table 20 Zn/Cr molar ratio, surface area, porous volume and zeta potential for the  $\text{Zn}_2\text{CrCO}_3$  matrix and the calcined derivatives.

Sample	Zn/Cr ratio*	$\zeta$ (mV) $\pm$ 5	S BET ( $\text{m}^2\cdot\text{g}^{-1}$ ) $\pm$ 2	Porous Volume ( $\text{cm}^3\cdot\text{g}^{-1}$ )	Particle Size (nm)
$\text{Zn}_2\text{CrCO}_3$	2.3	25	39	0.137	740
$\text{Zn}_2\text{Cr-300}^\circ\text{C}$	2.4	0	40	0.140	>1000
$\text{Zn}_2\text{Cr-400}^\circ\text{C}$	2.3	3	36	0.147	>1000
$\text{Zn}_2\text{Cr-500}^\circ\text{C}$	2.3	3	29	0.108	>1000
$\text{Zn}_2\text{Cr-600}^\circ\text{C}$	2.	5	16	0.054	>1000
$\text{Zn}_2\text{Cr-800}^\circ\text{C}$	2.3	5	7	0.013	>1000

\*determined by EDS

As expected, EDS measurements indicate that the Zn/Cr molar ratio (Table 20) is nearly the same, regardless of the thermal treatment applied to the matrix. However, due to the dehydroxylation of the LDH layer at moderate temperature inducing a huge change of the surface properties, the zeta potential of the particles decreases from 25 mV for the pristine  $\text{Zn}_2\text{CrCO}_3$  material to 0 mV after 4h at 300 $^\circ\text{C}$  (Table 20) staying at similar values for

treatment at higher temperatures. Concerning the evolution of the Brunauer-Emmett-Teller (BET) specific surface areas upon calcination, the values (Table 20) are significantly reduced above 500°C. This trend is directly correlated to the oxides and mixed oxides crystallization. Generally for LDH matrices, an optimum is reached upon moderate thermal treatment (250°C-350°C) in term of surface area corresponding to the formation of amorphous mixed oxides [227]. Such behaviour is not observed for Zn<sub>2</sub>Cr composition probably due to the premature decomposition of hydroxyl layered previously evidenced by PXRD. As illustrated on the Figure 42, Zn<sub>2</sub>CrCO<sub>3</sub> and Zn<sub>2</sub>Cr-600°C exhibit type IV adsorption isotherms according to Rouquerol et al. [228] which are characteristic of mesoporous materials.

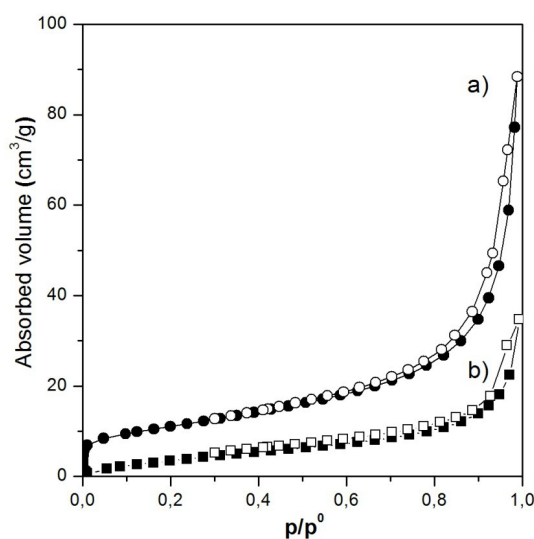


Fig. 58 Nitrogen adsorption-desorption isotherms of a) Zn<sub>2</sub>CrCO<sub>3</sub> and b) Zn<sub>2</sub>Cr-600 °C

The hysteresis loop is type H3 corresponding to slit shape pores usually observed for LDH materials due to the presence of aggregates of plate like particles. Such morphology is confirmed by SEM and TEM images presented in Figure 4 which reveal for the uncalcined Zn<sub>2</sub>CrCO<sub>3</sub> precursor the presence of stacked plate-like particles with size in the range of 150-200 nm ± 20 nm. Because of the collapse of the layered structure and the oxides crystallization occurring at 600°C, the particle size is clearly reduced on the SEM and TEM images (Fig. 43), with the presence of smaller spherical particles at the platelet surface.

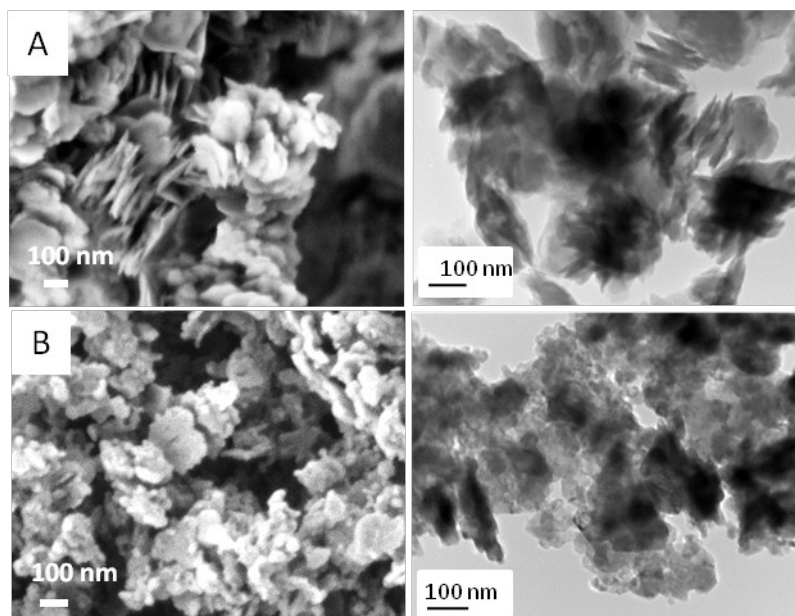


Fig. 59 FESEM (left) and TEM (right) images of A)  $Zn_2CrCO_3$  and B)  $Zn_2Cr-600^\circ C$

Other important parameters of photocatalysts are the size of particles, which has an influence on stability of aqueous suspension, and surface area. The size was possible to measure only for noncalcined sample  $Zn_2CrCO_3$ , an average of particle size of 740 nm was measured. For the other samples the size was larger than 1  $\mu m$  evidencing to some extent a sintering of the materials upon calcination. All calcined samples underwent sedimentation and contained big agglomerates, which is in good correlation with measurement of zeta potential of each sample (Table 20).

Indeed, LDH sample before calcination had positive zeta potential with value around 25 mV. After the calcinations the zeta potential significantly decreased close to zero value (calcination temperature  $300^\circ C$ ) and with increasing temperature of calcination also the value of zeta potential is roughly unmodified.

#### 5.5.1.1. Adsorption isotherms of Acid Orange 7

Prior to UV-vis irradiation, AO7 adsorption on  $Zn_2CrCO_3$  uncalcined and calcined was studied in dark. Indeed, LDH are well known for their high adsorption properties [229-231]. The adsorption experiments were carried out for all the samples by the same procedure. Adsorption isotherms of AO7 molecules by  $Zn_2CrCO_3$  LDH phase and calcined derivatives at  $20^\circ C$  are presented in Fig. 60.

It was found that the noncalcined LDH has the highest adsorption ability among all the prepared samples. With the increasing temperature of calcination, the amount of adsorbed AO7 on the sample surface is decreasing. According to the classification proposed by Giles et al. [232] these isotherms correspond to the L-type adsorption reaction which are observed when the adsorbent possesses a high affinity for adsorbed molecules. Such behaviour was

previously described for AO7 adsorbed on MgAl LDH [233]. In the case of the  $Zn_2CrCO_3$  LDH precursor adsorption seems to follow two different trends. At the lower concentration, high adsorption observed corresponds to a Langmuir behaviour while at higher concentration the isotherm correspond more to Freundlich model.

Systematically for calcined samples plateau is reached at very low equilibrium concentration ( $<0.5\text{mol.L}^{-1}$ ). Due to the greater adsorption properties of pristine LDH plateau is reached only for an equilibrium value of  $2.5\text{ mol.L}^{-1}$ . For all the samples no further adsorption is observed at higher concentrations ( $>4\text{ mol.L}^{-1}$ ). This trend indicates that the interactions between dye molecules and inorganic powder are stronger than the sorbent-sorbent interactions.

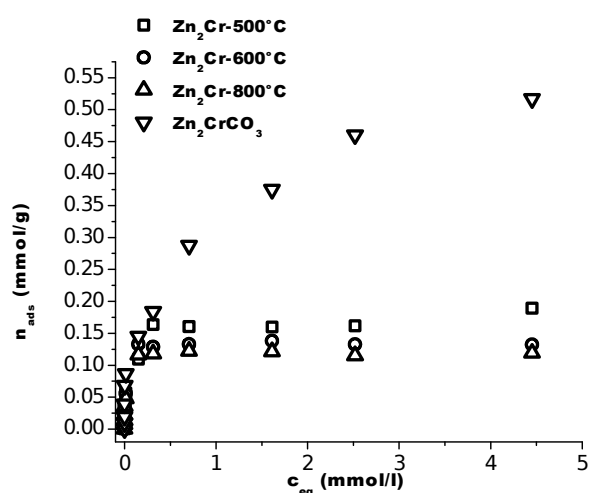


Fig. 60 AO7 adsorption isotherms for  $Zn_2CrCO_3$ ,  $Zn_2Cr-500^\circ C$ ,  $Zn_2Cr-600^\circ C$  and  $Zn_2Cr-800^\circ C$

The XRD spectra after the AO7 adsorption for sample  $Zn_2CrCO_3$  are shown in Fig. 61. All the diffraction lines are unmodified after adsorption process, in particular the 00l lines, evidencing that AO7 molecules are not intercalated into the layered structure but only adsorbed at the particle surface. Such behaviour is in good agreement with the high affinity of carbonate anions for LDH matrix, avoiding their replacement through anionic exchange process. However, on the PXRD patterns we can observe appearance of peak at  $\theta = 18^\circ$  with increasing AO7 concentration in the experimental system. This peak can be associated with adsorbed AO7 or intercalation of AO7 to the structure of  $ZnCr-LDH$ .

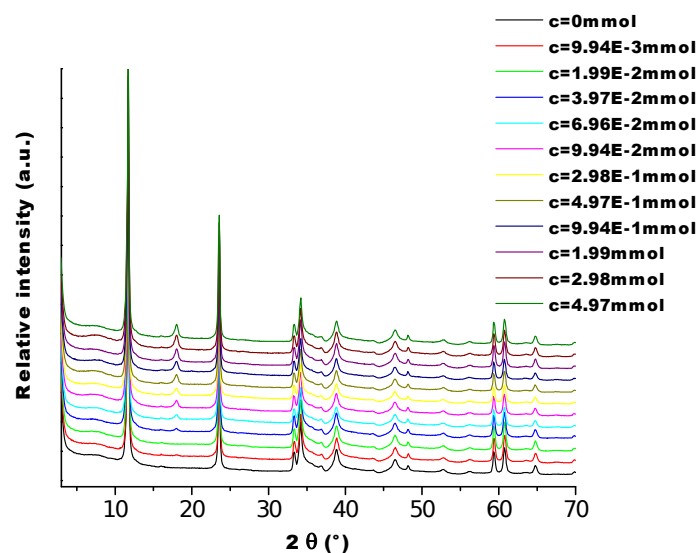


Fig. 61 XRD patterns of  $Zn_2CrCO_3$  after the 12 hours adsorption isotherm measurement for the different AO7 concentrations tested

### 5.5.2. Photocatalytic activity

The study of photocatalytic activity of prepared LDH was done by degradation of Acid Orange 7. Experiments were performed with constant concentration of LDH in suspension. ( $0.5 \text{ g.L}^{-1}$ ), the concentration of model compound was systematically fixed at  $5 \cdot 10^{-5} \text{ mol.L}^{-1}$ . Concentration of photocatalyst was only modified to study the influence of photocatalyst loading on photocatalytic process and it will be described further in this chapter. Usually, 0.03 g of photocatalyst was added to 60 mL of AO7 solution and stirred in dark for 1 hour, and then the irradiation was started. At first noncalcined sample  $Zn_2CrCO_3$  LDH was studied. Before the measurement of AO7 concentration, it was necessary to dissolve the photocatalyst, because most of the AO7 was adsorbed on its surface. It was found that this sample exhibits photocatalytic properties. So the study at different pH was performed for this sample and the results are shown in Fig. 62.

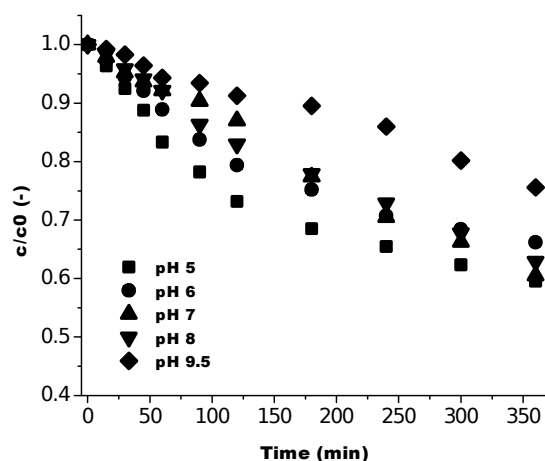


Fig. 62 Photodegradation of AO7 by  $Zn_2CrCO_3$  at different pH,  $c_{AO7} = 5 \times 10^{-5} \text{ mol.L}^{-1}$ , photocatalyst concentration  $0.5 \text{ g.L}^{-1}$

Before each photocatalytic test, the reaction system was kept without the UV irradiation for half an hour to reach the adsorption equilibrium. It was found that adsorption at pH 5 was about 28%, for pHs 6, 7 and 8 was about 25%, and for pH 9.5 was only 18%. For further study we chose neutral pH - pH 7, which is closer to real applications.

For pH range from 5 to 8, all the results were quite comparable, only the higher decrease of photoactivity was observed when the reaction took place at pH 9.5. It can be caused by decreasing adsorption of AO7 with increasing pH. The decrease in adsorption can be caused by competition with carbonate intercalation [233]. The degradation rates are shown in Table 17.

Table 21 Degradation rate of AO7 in first 60 minutes of irradiation,  $ZnCrCO_3$

pH	5	6	7	8	9.5
$r_i (\text{mol.min}^{-1})$	$8.00 \times 10^{-9}$	$5.59 \times 10^{-9}$	$3.70 \times 10^{-9}$	$3.82 \times 10^{-9}$	$2.86 \times 10^{-9}$

Then the influence of different calcinations temperature was studied. Sample  $Zn_2CrCO_3$  was calcined at 300, 400, 500, 600 and 800°C and the photoactivity of these calcined derivatives was measured in the conditions as before at fixed pH 7. It was found that the calcination temperature has significant influence on photocatalytic activity of  $Zn_2CrCO_3$  LDH. A moderate thermal treatment at temperature lower than 500°C induces a net decrease of the photocatalytic activity, whereas for calcined  $Zn_2CrCO_3$  at higher temperature (500°C, 600°C and 800°C) the photoactivity increased. Note that for the temperature 600°C and 800°C, the rate of the degradation was almost the same. The results of AO7 degradation are shown in Fig. 63 and  $r_i$  in Fig. 64.

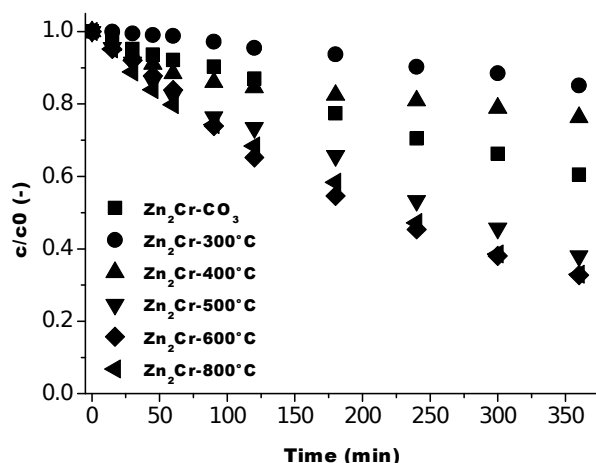


Fig. 63 Photodegradation of AO7 by Zn<sub>2</sub>CrCO<sub>3</sub> calcined at different temperatures, pH 7, c<sub>AO7</sub> = 5×10<sup>-5</sup> mol.L<sup>-1</sup>, photocatalyst concentration 0.5 g.L<sup>-1</sup>

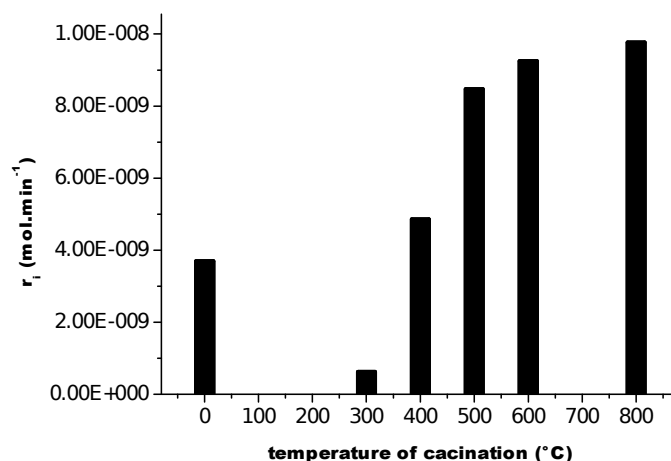


Fig. 64 Degradation rate of ZnCrCO<sub>3</sub> calcined at different temperatures in first 60 minutes

Samples calcined at 500, 600 and 800°C showed the highest photoactivity, these samples according to XRD measurement contain crystalline ZnO phase. To see the influence of photocatalytic reaction on the structure of photocatalysts, the XRD spectra were measured for all the samples before and after the photocatalytic measurement. The results are shown in Fig. 65.

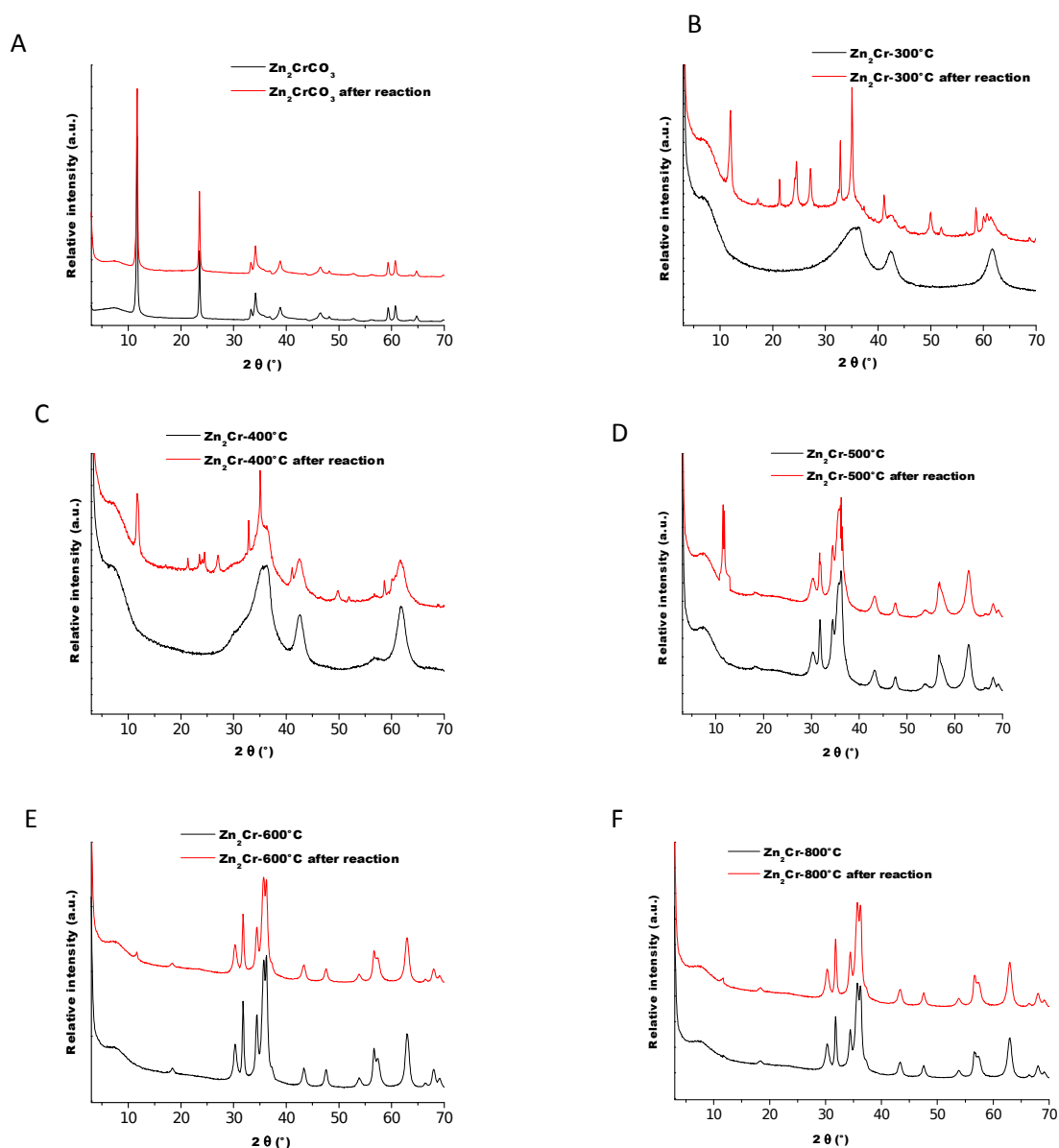


Fig. 65 XRD spectra before and after photocatalytic experiments for samples: A)  $\text{Zn}_2\text{CrCO}_3$ , B)  $\text{Zn}_2\text{Cr-300}^\circ\text{C}$ , C)  $\text{Zn}_2\text{Cr-400}^\circ\text{C}$ , D)  $\text{Zn}_2\text{Cr-500}^\circ\text{C}$ , E)  $\text{Zn}_2\text{Cr-600}^\circ\text{C}$  and F)  $\text{Zn}_2\text{Cr-800}^\circ\text{C}$

The main differences in spectra can be seen for samples  $\text{Zn}_2\text{Cr-300}^\circ\text{C}$  and  $\text{Zn}_2\text{Cr-400}^\circ\text{C}$ . In these cases almost no photocatalytic degradation took place and the XRD patterns display broad diffraction lines corresponding to the formation of amorphous mixed oxides. After photocatalytic measurements, we can see on the XRD patterns the appearance of supplementary thin diffraction lines evidencing the formation of new phases probably by mixed oxides rehydration. It is important to remind here a specific feature of LDH compound which is based on the ability of pristine LDH materials to recover after moderate thermal treatment its starting layered structure by simple rehydration. Accordingly, we can see reappearance of typical XRD lines of LDH at  $2\theta = 11^\circ$  and two at above  $2\theta = 60^\circ$ . For the rest of the samples the main change appears around value  $2\theta = 11^\circ$ , we can see a new peak there.

The XRD spectra of Zn<sub>2</sub>Cr-600°C and Zn<sub>2</sub>Cr-800°C showed minimal changes. Samples Zn<sub>2</sub>Cr-600°C and Zn<sub>2</sub>Cr-800°C showed the highest photoactivity, however, it is more economical to prepare the photocatalyst at lower temperature so the sample Zn<sub>2</sub>Cr-600°C was chosen for further study.

The same study of pH influence as for Zn<sub>2</sub>CrCO<sub>3</sub> was performed for Zn<sub>2</sub>Cr-600°C. The results are shown in Fig. 66.

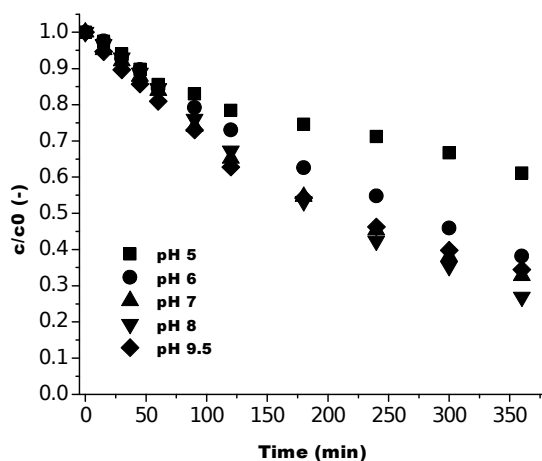


Fig. 66 Photodegradation of AO7 by Zn<sub>2</sub>Cr-600°C at different pHs

Initial degradation rate were calculated and are shown in Table 22.

Table 22 Degradation rate of AO7 in first 60 minutes of irradiation, ZnCr-600°C

pH	5	6	7	8	9,5
r <sub>i</sub> (mol.min <sup>-1</sup> )	8.07×10 <sup>-9</sup>	7.51×10 <sup>-9</sup>	8.00×10 <sup>-9</sup>	7.50×10 <sup>-9</sup>	9.77×10 <sup>-9</sup>

It was found that the lowest degradation rate is at pH 5, with increasing pH the degradation rate slightly increases but for pHs 7, 8 and 9.5 the rate is almost the same, which is opposite to non-calcined sample behaviour. This can be explained by the different surface charge of both photocatalysts. The zeta potential of calcined sample suspended in water at pH 7 is almost zero, this means that surface charge of photocatalyst is also almost zero, which means that AO7 is not that much adsorbed on the surface of Zn<sub>2</sub>Cr-600°C so the pH should not have strong influence on the photoactivity like in the case of noncalcined sample. Different behaviour was observed at pH 5, after one hour of irradiation the degradation rate decreased and it can be explained by the decreased stability of Zn<sub>2</sub>Cr-600°C in lower pH and possible reconstruction of LDH structure at pH 5 [234].

As a next step the influence of photocatalyst loading was investigated and shown in Fig. 67, the rate of degradation of AO7 is shown Fig. 68. It can be seen that degradation rate of AO7 increases with increasing concentration of  $Zn_2Cr-600^\circ C$  from  $0.25\text{ g.L}^{-1}$  to  $0.5\text{ g.L}^{-1}$ . However, with further increase in concentrations from  $0.5$  to  $1\text{ g.L}^{-1}$  we see only very small increase. The increase of the catalyst mass results in an increase of absorbed light and it will, at some point, lead to the saturation of light absorption and the fact that the rate of degradation do not further increase. Thus, the amount of  $0.5\text{ g.L}^{-1}$  seems to be an optimal amount of photocatalyst.

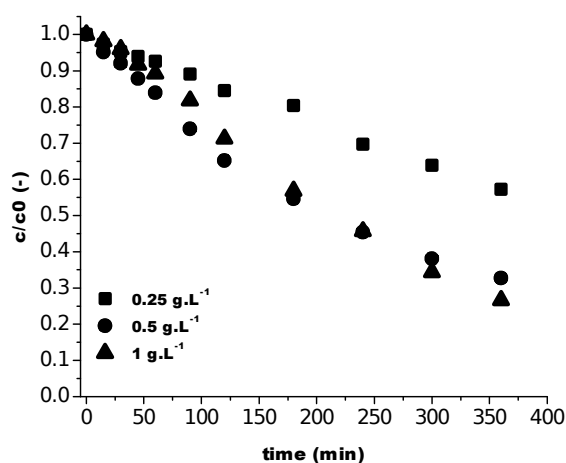


Fig. 67 Influence of photocatalyst loading ( $Zn_2Cr-600^\circ C$ ) on the degradation of AO7

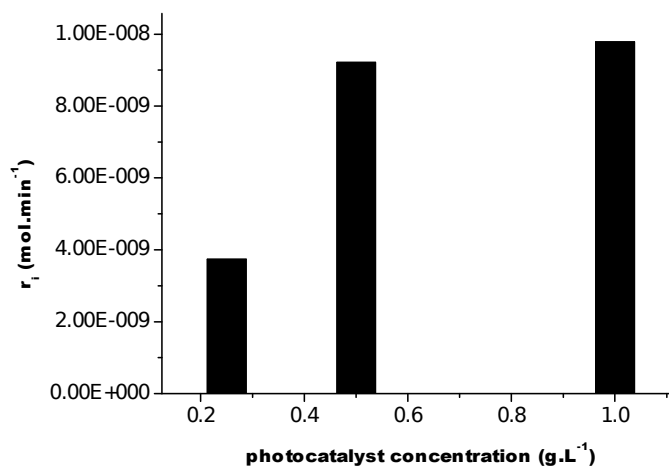


Fig. 68 Degradation rate of  $ZnCr-600$  in first 60 minutes – different concentration of photocatalyst

As another parameter the influence of light source was investigated. Three types of lamps were used:

- Philips HPW type 125 W (narrow maximum at 365 nm)
- Phillips TLD 15W/05 (wide maximum at 365 nm)
- TL100W/10R UV-A BULB (maximum at 313 nm).

The results of measurement are in Fig. 69.

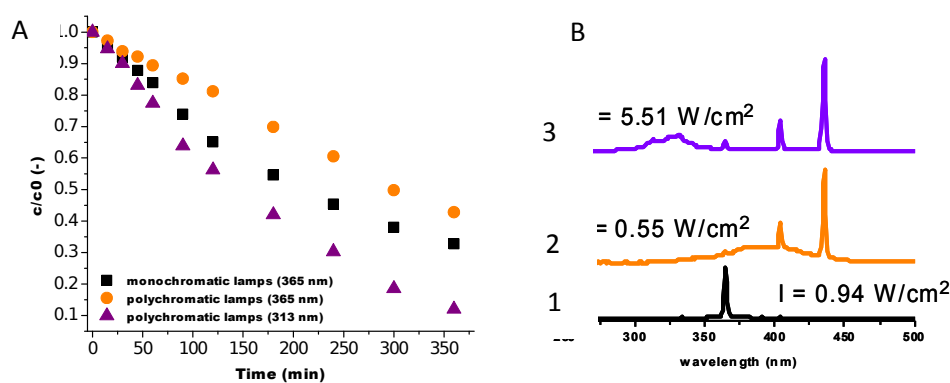


Fig. 69 Influence of different light sources on AO7 degradation, A)  $\text{Zn}_2\text{Cr}$ -600°C photocatalyst and B) light sources spectra and intensity , 1 - Philips HPW type 125 W, 2 - Phillips TLD 15W/05, 3 - TL100W/10R UV-A BULB

$\text{ZnCr}$ -600 photocatalyst showed the highest photocatalytic activity under the irradiation by light source with the emission around 313 nm, but it is necessary to mention, that this light source has not only the highest light intensity ( $5.5 \text{ W}\cdot\text{cm}^{-2}$ ) but also the highest energy (given by the wavelength) which both are crucial for the rate of photocatalytic processes [235]. The lamps with emission maximum around 365 nm have five times lower efficiency (monochromatic lamp), respectively 10 times lower (polychromatic lamp), than lamp with maximum at 313 nm. When we compare two lamps with maximum at 365 nm, we can see the difference which can be caused by the different intensity of light emitted by these lamps [236]. Philips HPW type 125 W (narrow maximum at 365 nm) has the intensity of light  $0.94 \text{ W}\cdot\text{cm}^{-2}$  which is almost two times higher than light intensity of Phillips TLD 15W/05 (wide maximum at 365 nm) –  $0.55 \text{ W}\cdot\text{cm}^{-2}$ . The initial reaction rate at time 60 minutes is shown in Table 23.

Table 23 Degradation rate of AO7 for different light sources,  $\text{ZnCr}$ -600

Lamp type	Philips HPW type 125 W	Phillips TLD 15W/05	TL100W/10R UV-A BULB
-----------	------------------------	---------------------	----------------------

	(narrow maximum at 365 nm)	(wide maximum at 365 nm)	(maximum at 313 nm)
$r_i$ ( $\text{mol}\cdot\text{min}^{-1}$ )	$9.22 \times 10^{-9}$	$5.22 \times 10^{-9}$	$1.11 \times 10^{-8}$

In first 60 minutes the difference in degradation rate for lamps emitting at 365 nm corresponds to the difference in their intensity. Initial degradation rate of lamp with narrow maximum at 365 nm is almost two times higher than for lamp with wide maximum at 365 nm, which is same as for their light intensity.

To find out if the AO7 undergoes complete mineralization by the degradation with  $\text{Zn}_2\text{Cr}-600^\circ\text{C}$  the total organic carbon (TOC) measurement was performed. The results are shown in Fig. 70. TOC analysis consists of total carbon (TC) and inorganic carbon (IC) measurement. Total organic carbon is then calculated by following equation:

$$\text{TOC} = \text{TC} - \text{IC} \quad (5-5-0)$$

We can see that organic carbon decreases with irradiation time. Starting amount of TOC was  $7.5 \text{ mg}\cdot\text{L}^{-1}$ , after 10 days (240 h), TOC concentration was  $1.3 \text{ mg}\cdot\text{L}^{-1}$ . So the photodegradation with  $\text{Zn}_2\text{Cr}-600^\circ\text{C}$  leads to total mineralization of AO7 to  $\text{CO}_2$ ,  $\text{H}_2\text{O}$  and inorganic salts. The decrease of TOC can be explained by the release of  $\text{CO}_2$  to the atmosphere. Starting concentration of IC corresponds to the solubility of  $\text{CO}_2$  in water at temperature  $15^\circ\text{C}$  (temperature during photodegradation reaction) and its increase during the reaction can be given by its further absorption in the reaction solution and on the photocatalyst, this can lead to the increase of inorganic carbon in the system.

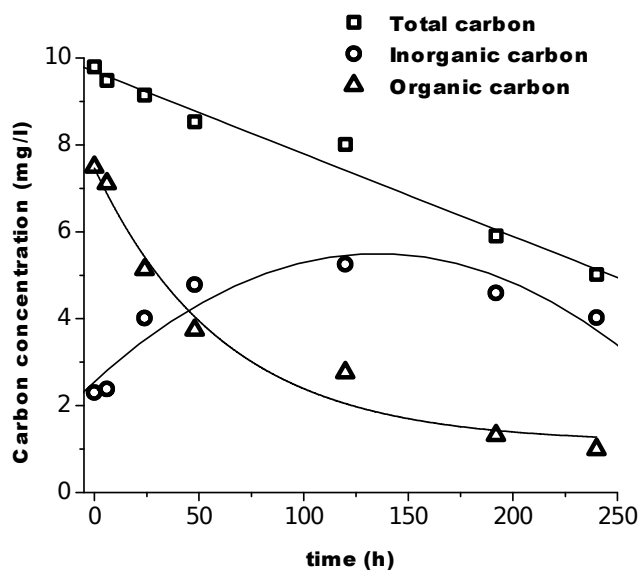


Fig. 70 TOC measurement of AO7 ( $5.10^{-5}$  mol.L<sup>-1</sup>) in the presence of Zn<sub>2</sub>Cr-600°C and under irradiation, pH 7

### 5.5.3. Study of the reaction mechanism

To be able to describe the degradation mechanism of pollutants by chosen photocatalyst it is necessary to measure the influence of different parameters on the reaction rate. First step was an identification of the oxidant species. At first, the photoproduction of HO<sup>•</sup> radicals was measured by photodegradation of terephthalic acid. Results of measurements performed at different wavelengths are shown in Fig. 71.

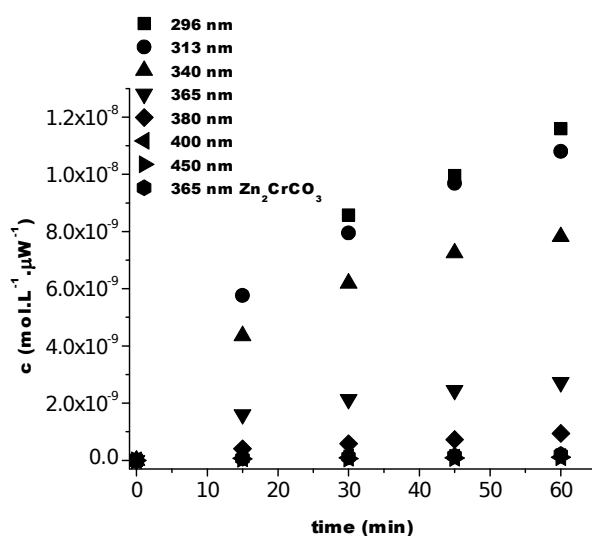


Fig. 71 Dependence of photoproduction of HO<sup>•</sup> radical on the light wavelength (Zn<sub>2</sub>Cr-600°C and Zn<sub>2</sub>CrCO<sub>3</sub> at 365 nm)

It was proved that HO<sup>•</sup> radicals are photoproduced at all wavelengths, but with different efficiency. The amount of HO<sup>•</sup> radicals produced increased with decreasing wavelengths from 296 to 450 nm. The highest production was observed for light of wavelength 296 nm. For the light with higher wavelengths than 400 nm, the production was around 2 orders of magnitude lower than for lower wavelengths. It was also proved that even after irradiation of noncalcined sample HO<sup>•</sup> radicals were produced. The concentration of HO<sup>•</sup> radicals in first 15 minutes of measurement is shown in Table 24. The rate of HO<sup>•</sup> radical photoproduction,  $r_{OH}$  was calculated according to the following equation:

$$r_{OH} = \frac{c_{TAOH}}{Y_{TAOH} \cdot t \cdot I_0} \quad , \quad (5-5-0)$$

where  $c_{TAOH}$  is concentration of produced TAOH in mol.L<sup>-1</sup>,  $Y_{TAOH}$  is the formation yield of TAOH – value for our system 0.22 [188],  $t$  is irradiation time in minutes and  $I_0$  is light intensity in  $\mu\text{W}\cdot\text{cm}^{-2}$ .

Table 24: Reaction rate of HO<sup>•</sup> radicals photoproduction in first 15 minutes of measurement

Sample	Zn <sub>2</sub> Cr- 600°C							Zn <sub>2</sub> CrCO <sub>3</sub>
	296	313	340	365	380	400	450	365
Wavelength (nm)	296	313	340	365	380	400	450	365
I ( $\mu\text{W}\cdot\text{cm}^{-2}$ )	98.1	160	251	397	758	914	846	397
$c_{OH}$ (mol.L <sup>-1</sup> ) 10 <sup>-6</sup>	1.85	2.76	3.28	1.91	0.925	0.199	0.118	0.0830
$r_{OH}$ (mol.L <sup>-1</sup> · $\mu\text{W}^{-1}$ ·min <sup>-1</sup> ) 10 <sup>-11</sup>	2.80	2.56	1.93	0.71	0.180	0.032	0.021	0.031

The increase of photoproduction of HO<sup>•</sup> radicals for calcined sample can be caused by the presence of ZnO which is known photocatalyst and it was proved that ZnO is able to produce HO<sup>•</sup> radicals [237].

As another step it was necessary to test if the HO<sup>•</sup> radicals are only oxidation species in the reaction. This photodegradation of AO7 was performed in the presence of isopropanol which is known as an efficient scavenger of HO<sup>•</sup> radicals [238]. The results for the samples Zn<sub>2</sub>Cr-600°C and Zn<sub>2</sub>CrCO<sub>3</sub> are shown in Fig. 72 and Fig. 73.

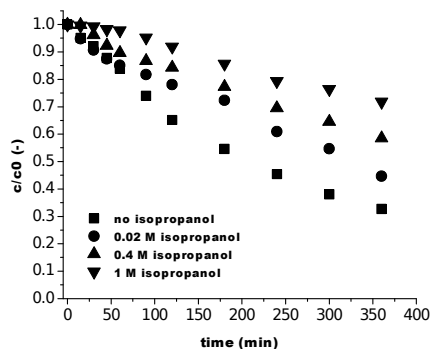


Fig. 72 Influence of addition of isopropanol to reaction system Zn<sub>2</sub>Cr-600°C 0.5 g.L<sup>-1</sup> on the degradation of AO7 ( $c = 5 \times 10^{-5}$  mol.L<sup>-1</sup>)

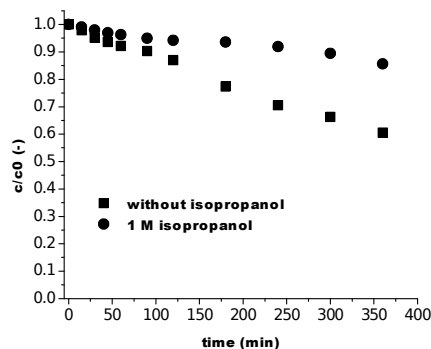


Fig. 73 Influence of addition of isopropanol to reaction system, Zn<sub>2</sub>CrCO<sub>3</sub> 0.5 g.L<sup>-1</sup> on the degradation of AO7 ( $c = 5 \times 10^{-5}$  mol.L<sup>-1</sup>)

From the data shown in Fig. 72 and Fig. 73 initial degradation rates were calculated and shown in Fig. 67 as a function of isopropanol concentration. We can see that the isopropanol has an influence on the degradation of AO7 by Zn<sub>2</sub>Cr-600°C, but only at higher concentrations. If the concentration of isopropanol is 1 mol.L<sup>-1</sup>, then the degradation of AO7 is strongly decreased (total amount of AO7 degraded after 6 hours decreased about four times - Fig. 74). For low isopropanol concentrations (0.02 M), the influence of isopropanol is almost negligible. But even thus we can observe the decrease of initial reaction rate. Chen et al. described that low concentration of isopropanol (0.1 mol.L<sup>-1</sup>) almost does not affect the degradation rate of AO7 [23], which is in agreement with obtained results. However, using the isopropanol with concentration of 1 mol.L<sup>-1</sup> decreased the initial degradation rate  $r_i$  almost 10 times.

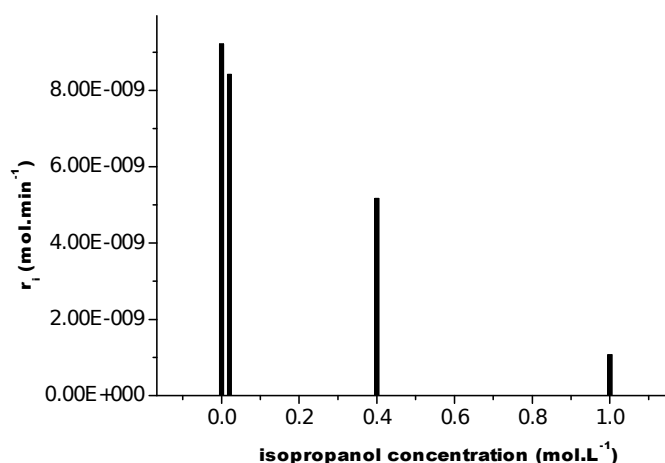


Fig. 74 Reaction rate of AO7 degradation in the system with isopropanol of different concentration, 0.5 g.L<sup>-1</sup> Zn<sub>2</sub>Cr-600°C, pH = 7

In the case of Zn<sub>2</sub>CrCO<sub>3</sub> catalyst, degradation of AO7 in the presence of 1 mol.L<sup>-1</sup> isopropanol decreased but did not stopped completely. The final amount of degraded AO7 was only around 14% which is much lower in comparison with system without isopropanol – 40% degraded AO7. The initial rate of degradation in the presence of isopropanol was 1.9×10<sup>-9</sup> mol.min<sup>-1</sup> which is four time lower than for the system without isopropanol (r<sub>i</sub> = 8.0×10<sup>-9</sup> mol.min<sup>-1</sup>).

After those test we can assume that the degradation of azo dye, in the presence of noncalcined ZnCr LDH or calcined ZnCr LDH, is undergoing the reaction by hydroxyl radical mechanism in bulk and the direct hole mechanism on the surface of the photocatalyst in the same time because the AO7 is adsorbed on the surface of all used photocatalyst and the reaction is not inhibited by addition of isopropanol.

For the better understanding of reaction mechanism, another model compound was used – 4-chlorophenol. 4-CP is not adsorbed on the surface of photocatalyst, after the 0.5 h in dark the concentration of 4-CP in the suspension of catalyst did not decrease. The measurements were performed with Zn<sub>2</sub>CrCO<sub>3</sub> and with Zn<sub>2</sub>Cr-600 °C at pH 7 and the results are shown in Fig. 75. The degradation of 4-CP was observed only with the usage of calcined sample, initial reaction rate of this reaction was 6.60×10<sup>-9</sup> mol.min<sup>-1</sup>. When the degradation was carried out in the presence of 1 mol.L<sup>-1</sup> isopropanol, the reaction was almost stopped, inhibition of 4-CP degradation by isopropanol was described by Lin et al [239]. The concentration of 4-CP decreased only about 4 %.

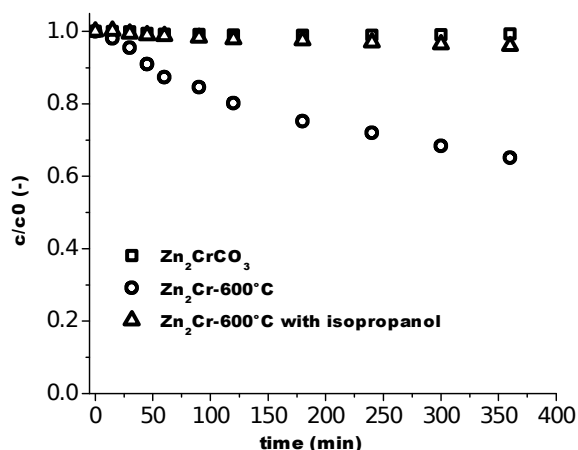


Fig. 75 Degradation of 4-CP by Zn<sub>2</sub>CrCO<sub>3</sub> and Zn<sub>2</sub>Cr-600°C (reaction carried out without and with isopropanol)

This decrease of photocatalytic activity in the case of 4-CP can be caused by the different mechanism than in the case of AO7. As 4-CP is not adsorbed on the surface, the reaction can be carried out only in the bulk by hydroxyl radical mechanism. In the case of Zn<sub>2</sub>CrCO<sub>3</sub> the amount of HO<sup>•</sup> radicals is so low, that we cannot observe any change of the pollutant concentration. But in the case of AO7 degradation still occurs even in the presence of isopropanol, AO7 is adsorbed on the surface of ZnCrCO<sub>3</sub>. This means that in the case of non-calcined ZnCrCO<sub>3</sub> the organic compounds are degraded mainly by direct hole mechanism on the photocatalyst surface and HO<sup>•</sup> radicals has minor effect. This confirm the theory about two simultaneous reaction (in the bulk by HO<sup>•</sup> radicals and on the surface by direct hole mechanism), when the model compound was not adsorbed on the photocatalyst surface and the reaction carried out by the HO<sup>•</sup> radicals was inhibited, the degradation of organic compound did not occurred. LDH photocatalysts are therefore better for removal of absorbable compounds.

## 6. CONCLUSIONS

It was confirmed that the simple visible absorption spectrophotometry can be used reliably to determine the concentration changes of AO7 during its photocatalytic degradation. At low concentrations ( $10^{-5}$ - $10^{-4}$  mol.L<sup>-1</sup>) the first order rate constant for the photocatalytic destruction of AO7 decreases with increasing concentration of AO7, whereas for 4-CP, it remains unchanged. This effect is not due to an approaching monolayer surface coverage of the AO7 on the titania photocatalyst but instead is due to UV screening of the titanium dioxide film by the dye AO7. This UV screening effect of AO7 solution is significant for concentrations  $> 2.5 \times 10^{-5}$  mol.L<sup>-1</sup> and can be corrected in the calculation of initial degradation rates to reveal a direct dependence of rate upon AO7 concentration under the experimental conditions used in this work. At low stirring speeds ( $< 890$  rpm for AO7 and  $< 220$  rpm for 4-CP) the kinetics of organic destruction are mass transfer controlled. Calculations show that under these conditions, the photocatalytic degradation rate was controlled by the diffusion rate of a model compound (AO7 or 4-CP) to the surface of TiO<sub>2</sub> layer.

Acidic colloidal suspension of TiO<sub>2</sub> was successfully prepared. Concerning the transformation of TiO<sub>2</sub> colloidal suspensions from acidic to alkaline environments, it was found that the change in particle size depends on the type of basic agent used (KOH, NH<sub>4</sub>OH), on its concentration and on the starting concentration of TiO<sub>2</sub>. The smallest change of particle size was observed after titration with NH<sub>4</sub>OH and during aging of suspensions prepared from 6.3 mmol.dm<sup>-3</sup> TiO<sub>2</sub> and 1 mol.dm<sup>-3</sup> NH<sub>4</sub>OH kept at 20°C. It was also found that the acidic suspension kept at 4°C had the slowest change in particle size during aging. This suspension also had the slowest decrease in band gap energy and the quantum yield of photocatalytic degradation of 4-chlorophenol remained unchanged (~1%). The suspension, after more than five months, was clear and without turbidity. Other acidic suspensions kept at higher temperatures were turbid even after long time periods. From the perspective of minimal particle size change, storing in acidic suspension at low temperature (e.g. 4°C) is optimal, the colloidal suspension remaining transparent. To achieve the best photoactivity, storage in the form of acidic suspension at room temperature (e.g. 20°C) is optimal. The quantum yield of 4-CP degradation for suspensions kept at 20°C and 40°C are similar (especially for long aging times); thus storing at room temperature avoids the additional cost of energy for heating.

TiO<sub>2</sub>/Mg<sub>2</sub>Al nanocomposites were prepared by spontaneous self-assembly process involving colloidal suspensions of each component. High loading of TiO<sub>2</sub> nanoparticles in the nanocomposite was achieved whereas the use of Mg<sub>2</sub>Al support limits the TiO<sub>2</sub> nanoparticles aggregation. Immobilization of TiO<sub>2</sub> at the surface of the LDH nanosheet was evidenced by TEM and induced the creation of interparticular mesoporosity into the materials. Self-

assembled TiO<sub>2</sub>/Mg<sub>2</sub>Al nanocomposites exhibited equivalent or much higher photocatalytic activity than the original TiO<sub>2</sub> in basic conditions for AO7 and 4-CP degradation whereas they are much easier to recover by simple sedimentation.

TiO<sub>2</sub>/SiO<sub>2</sub> composite materials were prepared from aqueous suspensions of each component. The TiO<sub>2</sub>/SiO<sub>2</sub> composites were successfully prepared as a colloidal suspension and as a powder, obtained from the coagulation of mixed TiO<sub>2</sub> and SiO<sub>2</sub> colloidal suspensions. The photoactivity of colloidal suspension was tested in liquid phase by the AO7 and MB degradation. It was found that in acidic pH, the presence of SiO<sub>2</sub> increased the photodegradation of MB. Further, it was found that coagulation of prepared amorphous TiO<sub>2</sub> in the presence of SiO<sub>2</sub> leads to the crystallization of TiO<sub>2</sub> powder in anatase phase. From obtained powders, the layers were prepared by sedimentation method. Photocatalytic activity of the layers was tested in gas phase by the degradation of hexane as a model compound. The flow of carrier air was 1 Ndm<sup>3</sup>.min<sup>-1</sup> and hexane inlet concentration was 4 ppm. The maximum conversion reached was around 30% using TiO<sub>2</sub>/SiO<sub>2</sub> 1:1 (D) composite (composite prepared by mixing of precursors suspension followed by precipitation), which corresponds to hexane degradation rate of 0.1 mmol.m<sup>-2</sup>.h<sup>-1</sup>.

Zn<sub>2</sub>CrCO<sub>3</sub> LDH was prepared by coprecipitation and anionic exchange method. It was found that this type of LDH has photocatalytic activity. This sample was then calcined at different temperatures to obtain mixed oxides (especially ZnO which is known as a good photocatalyst) to increase the photocatalytic properties of prepared Zn<sub>2</sub>CrCO<sub>3</sub> LDH. It was found that the best temperature for the most photoactive sample is 600 °C. The sample at 600 °C was well crystalline and the rate of AO7 degradation was almost 2 times higher than for Zn<sub>2</sub>CrCO<sub>3</sub> LDH without calcinations. It was proved that one of oxidating species are HO<sup>•</sup> radicals. HO<sup>•</sup> radicals were produced even when noncalcined ZnCr-LDH is used as photocatalyst, but in concentrations 20 times lower than calcined sample with the same light irradiation (λ = 365 nm). Since the AO7 degradation was not completely inhibited by OH scavenger (isopropanol) we can assume that the hydroxyl radical mechanism is accompanied by direct hole mechanism - the degradation of adsorbed AO7 directly on the surface of photocatalyst. This assumption is supported elsewhere by the measurement of 4-CP degradation, which did not adsorb on the photocatalyst surface oppositively to AO7. At the same conditions, 4-CP degradation was fully inhibited by addition of isopropanol.

## 7. REFERENCES

- [1] P.M. Fedorak, S.E. Hrudey, *Water Research* 18 (1984) 361-367.
- [2] T. Reemtsma, M. Jekel, *Water Research* 31 (1997) 1035-1046.
- [3] I. Oller, S. Malato, J.A. Sánchez-Pérez, *Sci Total Environ* 409 (2011) 4141-4166.
- [4] J. Kulas, I. Roušar, J. Krýsa, J. Jirkovský, *Journal of Applied Electrochemistry* 28 (1998) 843-853.
- [5] M.R. Hoffmann, S.T. Martin, W. Choi, D.W. Bahnemann, *Chemical Reviews* 95 (1995) 69-96.
- [6] A. Fujishima, K. Honda, *Nature* 238 (1972) 37-38.
- [7] R. Portela, M. Hernández-Alonso, in: J.M. Coronado, F. Fresno, M.D. Hernández-Alonso, R. Portela (Eds.), *Design of Advanced Photocatalytic Materials for Energy and Environmental Applications*, Springer London, 2013, pp. 35-66.
- [8] R. Gao, J. Stark, D.W. Bahnemann, J. Rabani, *Journal of Photochemistry and Photobiology A: Chemistry* 148 (2002) 387-391.
- [9] Y. Zhao, J. Han, Y. Shao, Y. Feng, *Environ Technol* 30 (2009) 1555-1563.
- [10] S.P. Paredes, M.A. Valenzuela, G. Fetter, S.O. Flores, *Journal of Physics and Chemistry of Solids* 72 (2011) 914-919.
- [11] D.W. Bahnemann, S.N. Kholuiskaya, R. Dillert, A.I. Kulak, A.I. Kokorin, *Applied Catalysis B: Environmental* 36 (2002) 161-169.
- [12] A. Mantilla, G. Jácome-Acatitla, G. Morales-Mendoza, F. Tzompantzi, R. Gómez, *Industrial & Engineering Chemistry Research* 50 (2011) 2762-2767.
- [13] F. Bruna, R. Celis, I. Pavlovic, C. Barriga, J. Cornejo, M.A. Ulibarri, *Journal of hazardous materials* 168 (2009) 1476-1481.
- [14] D.F. Ollis, *Comptes Rendus de l'Académie des Sciences - Series IIC - Chemistry* 3 (2000) 405-411.
- [15] A. Houas, H. Lachheb, M. Ksibi, E. Elaloui, C. Guillard, J.M. Herrmann, *Applied Catalysis B: Environmental* 31 (2001) 145-157.
- [16] M. Alexander, *Biotechnology and Bioengineering* 15 (1973) 611-647.
- [17] *Environ Eng Res* 6 (2001) 199-210.
- [18] C.S. Turchi, D.F. Ollis, *Journal of Catalysis* 122 (1990) 178-192.
- [19] O.M. Alfano, M.a.I. Cabrera, A.E. Cassano, *Journal of Catalysis* 172 (1997) 370-379.
- [20] M.a.I. Cabrera, A.C. Negro, O.M. Alfano, A.E. Cassano, *Journal of Catalysis* 172 (1997) 380-390.
- [21] K.-i. Ishibashi, A. Fujishima, T. Watanabe, K. Hashimoto, *Journal of Photochemistry and Photobiology A: Chemistry* 134 (2000) 139-142.
- [22] S.-H. Yoon, J.H. Lee, *Environmental Science & Technology* 39 (2005) 9695-9701.

- [23] Y. Chen, S. Yang, K. Wang, L. Lou, *Journal of Photochemistry and Photobiology A: Chemistry* 172 (2005) 47-54.
- [24] U. Stafford, K.A. Gray, P.V. Kamat, *The Journal of Physical Chemistry* 98 (1994) 6343-6351.
- [25] L. Cermenati, P. Pichat, C. Guillard, A. Albini, *The Journal of Physical Chemistry B* 101 (1997) 2650-2658.
- [26] L. Sun, J.R. Bolton, *The Journal of Physical Chemistry* 100 (1996) 4127-4134.
- [27] R.W. Matthews, *Journal of the Chemical Society, Chemical Communications* (1983) 177-179.
- [28] Y. Mao, C. Schoeneich, K.D. Asmus, *The Journal of Physical Chemistry* 95 (1991) 10080-10089.
- [29] S. Goldstein, G. Czapski, J. Rabani, *The Journal of Physical Chemistry* 98 (1994) 6586-6591.
- [30] R.B. Draper, M.A. Fox, *Langmuir : the ACS journal of surfaces and colloids* 6 (1990) 1396-1402.
- [31] Y. Sun, J.J. Pignatello, *Environmental Science & Technology* 29 (1995) 2065-2072.
- [32] K.-H. Wang, Y.-H. Hsieh, C.-H. Lin, C.-Y. Chung, *Chemosphere* 39 (1999) 1371-1384.
- [33] C.P. Chang, J.N. Chen, M.C. Lu, *J. Environ. Sci. Health Part A-Toxic/Hazard. Subst. Environ. Eng.* 38 (2003) 1131-1143.
- [34] M.A. Fox, M.T. Dulay, *Chemical Reviews* 93 (1993) 341-357.
- [35] C.H. Ao, S.C. Lee, *Journal of Photochemistry and Photobiology A: Chemistry* 161 (2004) 131-140.
- [36] Y. Luo, D.F. Ollis, *Journal of Catalysis* 163 (1996) 1-11.
- [37] T.N. Obee, S.O. Hay, *Environmental Science & Technology* 31 (1997) 2034-2038.
- [38] C. Raillard, V. Héquet, P. Le Cloirec, J. Legrand, *Journal of Photochemistry and Photobiology A: Chemistry* 163 (2004) 425-431.
- [39] J. Peral, D.F. Ollis, *Journal of Molecular Catalysis A: Chemical* 115 (1997) 347-354.
- [40] N. Abbas, M. Hussain, N. Russo, G. Saracco, *Chemical Engineering Journal* 175 (2011) 330-340.
- [41] J. Blanco, P. Avila, A. Bahamonde, E. Alvarez, B. Sánchez, M. Romero, *Catalysis Today* 29 (1996) 437-442.
- [42] E. Piera, J.A. Ayllón, X. Doménech, J. Peral, *Catalysis Today* 76 (2002) 259-270.
- [43] M.C. Blount, J.L. Falconer, *Applied Catalysis B: Environmental* 39 (2002) 39-50.
- [44] V. Augugliaro, S. Coluccia, V. Loddo, L. Marchese, G. Martra, L. Palmisano, M. Schiavello, *Applied Catalysis B: Environmental* 20 (1999) 15-27.
- [45] N. González-García, J.A. Ayllón, X. Doménech, J. Peral, *Applied Catalysis B: Environmental* 52 (2004) 69-77.
- [46] X. Fu, L.A. Clark, W.A. Zeltner, M.A. Anderson, *Journal of Photochemistry and Photobiology A: Chemistry* 97 (1996) 181-186.

- [47] B. Ohtani, *Journal of Photochemistry and Photobiology C: Photochemistry Reviews* 11 (2010) 157-178.
- [48] G.R. Belton, *MTB* 7 (1976) 35-42.
- [49] R.R. Giri, H. Ozaki, S. Taniguchi, R. Takanami, *Int. J. Environ. Sci. Technol.* 5 (2008) 17-26.
- [50] B. Neppolian, H.C. Choi, S. Sakthivel, B. Arabindoo, V. Murugesan, *Journal of hazardous materials* 89 (2002) 303-317.
- [51] P. Supphasrirongjaroen, P. Praserttham, J. Panpranot, D. Na-Ranong, O. Mekasuwandumrong, *Chemical Engineering Journal* 138 (2008) 622-627.
- [52] A. Lair, C. Ferronato, J.-M. Chovelon, J.-M. Herrmann, *Journal of Photochemistry and Photobiology A: Chemistry* 193 (2008) 193-203.
- [53] S. Sakthivel, B. Neppolian, M.V. Shankar, B. Arabindoo, M. Palanichamy, V. Murugesan, *Solar Energy Materials and Solar Cells* 77 (2003) 65-82.
- [54] N. Serpone, *Journal of Photochemistry and Photobiology A: Chemistry* 104 (1997) 1-12.
- [55] A. Fuerte, M.D. Hernandez-Alonso, A.J. Maira, A. Martinez-Arias, M. Fernandez-Garcia, J.C. Conesa, J. Soria, *Chemical Communications* (2001) 2718-2719.
- [56] G. Marci, M. Addamo, V. Augugliaro, S. Coluccia, E. García-López, V. Loddo, G. Martra, L. Palmisano, M. Schiavello, *Journal of Photochemistry and Photobiology A: Chemistry* 160 (2003) 105-114.
- [57] M. Zlámal, J. Krýsa, J. Jirkovský, *Catal Lett* 133 (2009) 160-166.
- [58] A.L. Linsebigler, G. Lu, J.T. Yates Jr, *Chemical Reviews* 95 (1995) 735-758.
- [59] N. Serpone, G. Sauvé, R. Koch, H. Tahiri, P. Pichat, P. Piccinini, E. Pelizzetti, H. Hidaka, *Journal of Photochemistry and Photobiology A: Chemistry* 94 (1996) 191-203.
- [60] R. Inaba, T. Fukahori, M. Hamamoto, T. Ohno, *Journal of Molecular Catalysis A: Chemical* 260 (2006) 247-254.
- [61] S. Ikeda, H. Kobayashi, T. Sugita, Y. Ikoma, T. Harada, M. Matsumura, *Applied Catalysis A: General* 363 (2009) 216-220.
- [62] C. Karunakaran, S. Senthilvelan, *Catalysis Communications* 6 (2005) 159-165.
- [63] B. Neppolian, Q. Wang, H. Jung, H. Choi, *Ultrasonics Sonochemistry* 15 (2008) 649-658.
- [64] J. Krýsa, G. Waldner, H. Měšťánková, J. Jirkovský, G. Grabner, *Applied Catalysis B: Environmental* 64 (2006) 290-301.
- [65] R. Hahn, M. Stark, M.S. Killian, P. Schmuki, *Catalysis Science & Technology* 3 (2013) 1765-1770.
- [66] L.H. Levine, J.T. Richards, J.L. Coutts, R. Soler, F. Maxik, R.M. Wheeler, *J Air Waste Manag Assoc* 61 (2011) 932-940.
- [67] J. Sun, L. Qiao, S. Sun, G. Wang, *Journal of hazardous materials* 155 (2008) 312-319.
- [68] A.E. Cassano, O.M. Alfano, *Catalysis Today* 58 (2000) 167-197.

- [69] V. Pareek, S. Chong, M. Tadé, A.A. Adesina, *Asia-Pacific Journal of Chemical Engineering* 3 (2008) 171-201.
- [70] R. Dillert, A. Engel, J. Grosse, P. Lindner, D.W. Bahnemann, *Physical Chemistry Chemical Physics* (2013).
- [71] T. Van Gerven, G. Mul, J. Moulijn, A. Stankiewicz, *Chemical Engineering and Processing: Process Intensification* 46 (2007) 781-789.
- [72] J.M. Hermann, *Catal. Today* 53 (1999) 115.
- [73] G. Al-Sayyed, J.C. D'Oliveira, P. Pichat, *Journal of Photochemistry and Photobiology, A: Chemistry* 58 (1991) 99-114.
- [74] J.-M. Herrmann, *Catalysis Today* 53 (1999) 115-129.
- [75] D.F. Ollis, E. Pelizzetti, N. Serpone, *Environmental Science and Technology* 25 (1991) 1522-1529.
- [76] S. Malato, P. Fernández-Ibáñez, M.I. Maldonado, J. Blanco, W. Gernjak, *Catalysis Today* 147 (2009) 1-59.
- [77] A. Mills, S. Le Hunte, *Journal of Photochemistry and Photobiology A: Chemistry* 108 (1997) 1-35.
- [78] S.T. Aruna, K.C. Patil, *Journal of Materials Synthesis and Processing* 4 (1996) 175-179.
- [79] V. Štengl, S. Bakardjieva, N. Murafa, J. Šubrt, H. Měšťánková, J. Jirkovský, *Materials Chemistry and Physics* 105 (2007) 38-46.
- [80] M. Landmann, E. Rauls, W.G. Schmidt, *Journal of Physics: Condensed Matter* 24 (2012) 195503.
- [81] L.G. Devi, B.N. Murthy, S.G. Kumar, *Journal of Molecular Catalysis A: Chemical* 308 (2009) 174-181.
- [82] X. Fu, L.A. Clark, Q. Yang, M.A. Anderson, *Environmental Science & Technology* 30 (1996) 647-653.
- [83] A. Henglein, *Berichte der Bunsengesellschaft für physikalische Chemie* 101 (1997) 1562-1572.
- [84] H. Weller, A. Eychmüller, *Advances in Photochemistry*, John Wiley & Sons, Inc., 2007, pp. 165-216.
- [85] P.V. Kamat, *Journal Name: CHEMTECH; Journal Volume: 25; Journal Issue: 6; Other Information: PBD: Jun 1995 (1995) Medium: X; Size: pp. 22-28.*
- [86] N. Serpone, D. Lawless, E. Pelizzetti, in: E. Pelizzetti (Ed.), *Fine Particles Science and Technology*, Springer Netherlands, 1996, pp. 657-673.
- [87] H. Lin, C.P. Huang, W. Li, C. Ni, S.I. Shah, Y.H. Tseng, *Applied Catalysis B-Environmental* 68 (2006) 1-11.
- [88] A. Hagfeldt, M. Graetzel, *Chemical Reviews* 95 (1995) 49-68.
- [89] Y. Wang, N. Herron, *The Journal of Physical Chemistry* 95 (1991) 525-532.

- [90] A. Golubović, M. Šćepanović, A. Kremenović, S. Aškračić, V. Berec, Z. Dohčević-Mitrović, Z.V. Popović, *J Sol-Gel Sci Technol* 49 (2009) 311-319.
- [91] Y. You, S. Zhang, L. Wan, D. Xu, *Applied Surface Science* 258 (2012) 3469-3474.
- [92] A. Chemseddine, T. Moritz, *European Journal of Inorganic Chemistry* 1999 (1999) 235-245.
- [93] V. Lafond, P.H. Mutin, A. Vioux, *Chemistry of Materials* 16 (2004) 5380-5386.
- [94] D.P. Serrano, G. Calleja, R. Sanz, P. Pizarro, in: F.F.F.D.R. A. Galarneau, J. Vedrine (Eds.), *Studies in Surface Science and Catalysis*, Elsevier, 2001, p. 251.
- [95] K.D. Kim, S.H. Kim, H.T. Kim, *Colloids and Surfaces A: Physicochemical and Engineering Aspects* 254 (2005) 99-105.
- [96] D.V. Bavykin, J.M. Friedrich, F.C. Walsh, *Advanced Materials* 18 (2006) 2807-2824.
- [97] Y. Jing, L. Li, Q. Zhang, P. Lu, P. Liu, X. Lü, *Journal of hazardous materials* 189 (2011) 40-47.
- [98] J.H. Lee, Y.S. Yang, *Materials Chemistry and Physics* 93 (2005) 237-242.
- [99] M. Kolář, H. Měšťánková, J. Jirkovský, M. Heyrovský, J. Šubrt, *Langmuir : the ACS journal of surfaces and colloids* 22 (2005) 598-604.
- [100] Y. Chen, A. Lin, F. Gan, *Powder Technology* 167 (2006) 109-116.
- [101] V. Tohver, J.E. Smay, A. Braem, P.V. Braun, J.A. Lewis, *Proceedings of the National Academy of Sciences* 98 (2001) 8950-8954.
- [102] R. Greenwood, K. Kendall, *Journal of the European Ceramic Society* 19 (1999) 479-488.
- [103] D. Hanaor, M. Michelazzi, C. Leonelli, C.C. Sorrell, *Journal of the European Ceramic Society* 32 (2012) 235-244.
- [104] C.G. Silva, Y. Bouizi, V. Fornés, H. García, *Journal of the American Chemical Society* 131 (2009) 13833-13839.
- [105] V. Rives, *Layered Double Hydroxides: Present and Future*, Nova Science Publishers, 2001.
- [106] S. Pausova, J. Krysa, J. Jirkovsky, G. Mailhot, V. Prevot, *Environ Sci Pollut Res Int* 19 (2012) 3709-3718.
- [107] R.E. Johnsen, Q. Wu, A.O. Sjøstad, Ø.B. Vistad, F. Krumeich, P. Norby, *Journal of Physical Chemistry C* 112 (2008) 16733-16739.
- [108] L. Li, R. Ma, Y. Ebina, N. Iyi, T. Sasaki, *Chemistry of Materials* 17 (2005) 4386-4391.
- [109] F. Leroux, M. Adachi-Pagano, M. Intissar, S. Chauvière, C. Forano, J.P. Besse, *Journal of Materials Chemistry* 11 (2001) 105-112.
- [110] F. Kovanda, T. Grygar, V.t. Dorničák, *Solid State Sciences* 5 (2003) 1019-1026.
- [111] M. del Arco, V. Rives, R. Trujillano, P. Malet, *Journal of Materials Chemistry* 6 (1996) 1419.
- [112] Y. Guo, D. Li, C. Hu, Y. Wang, E. Wang, *International Journal of Inorganic Materials* 3 (2001) 347-355.
- [113] Y. Zhi, Y. Li, Q. Zhang, H. Wang, *Langmuir : the ACS journal of surfaces and colloids* 26 (2010) 15546-15553.

- [114] E.M. Seftel, E. Popovici, M. Mertens, K.D. Witte, G.V. Tendeloo, P. Cool, E.F. Vansant, *Microporous and Mesoporous Materials* 113 (2008) 296-304.
- [115] K. Morimoto, K. Tamura, N. Iyi, J. Ye, H. Yamada, *Journal of Physics and Chemistry of Solids* 72 (2011) 1037-1045.
- [116] L. Mohapatra, K.M. Parida, *Separation and Purification Technology* 91 (2012) 73-80.
- [117] N. Ahmed, Y. Shibata, T. Taniguchi, Y. Izumi, *Journal of Catalysis* 279 (2011) 123-135.
- [118] A. Mantilla, F. Tzompantzi, J.L. Fernández, J.A.I. Díaz Góngora, G. Mendoza, R. Gómez, *Catalysis Today* 148 (2009) 119-123.
- [119] S. Chakrabarti, B.K. Dutta, *Journal of hazardous materials* 112 (2004) 269-278.
- [120] F. Caruso, *Advanced Materials* 13 (2001) 11-22.
- [121] F. Caruso, X. Shi, R.A. Caruso, A. Susha, *Advanced Materials* 13 (2001) 740-744.
- [122] E.M. Seftel, E. Popovici, E. Beyers, M. Mertens, H.Y. Zhu, E.F. Vansant, P. Cool, *Journal of Nanoscience and Nanotechnology* 10 (2010) 8227-8233.
- [123] Z. Gao, B. Du, G. Zhang, Y. Gao, Z. Li, H. Zhang, X. Duan, *Industrial and Engineering Chemistry Research* 50 (2011) 5334-5345.
- [124] H. Shi, C. Yu, J. He, *Journal of Physical Chemistry C* 114 (2010) 17819-17828.
- [125] Y. Lee, J.H. Choi, H.J. Jeon, K.M. Choi, J.W. Lee, J.K. Kang, *Energy and Environmental Science* 4 (2011) 914-920.
- [126] L. Teruel, Y. Bouizi, P. Atienzar, V. Fornes, H. Garcia, *Energy & Environmental Science* 3 (2010) 154.
- [127] K.M. Parida, M. Sahoo, S. Singha, *Journal of Catalysis* 276 (2010) 161-169.
- [128] J. He, H. Shi, X. Shu, M. Li, *AIChE Journal* 56 (2010) 1352-1362.
- [129] M. Intissar, J.C. Jumas, J.P. Besse, F. Leroux, *Chemistry of Materials* 15 (2003) 4625-4632.
- [130] M. Shao, J. Han, M. Wei, D.G. Evans, X. Duan, *Chemical Engineering Journal* 168 (2011) 519-524.
- [131] X. Shu, J. He, D. Chen, Y. Wang, *J Phys Chem C Nanomater Interfaces* 112 (2008) 4151-4158.
- [132] G. Carja, A. Nakajima, S. Dranca, C. Dranca, K. Okada, *Journal of Physical Chemistry C* 114 (2010) 14722-14728.
- [133] M. Adachi-Pagano, C. Forano, J.P. Besse, *Chemical Communications* (2000) 91-92.
- [134] R. Ma, Z. Liu, L. Li, N. Iyi, T. Sasaki, *Journal of Materials Chemistry* 16 (2006) 3809-3813.
- [135] Q. Wu, A.O. Sjøstad, O.B. Vistad, K.D. Knudsen, J. Roots, J.S. Pedersen, P. Norby, *Journal of Materials Chemistry* 17 (2007) 965-971.
- [136] E. Gardner, K.M. Huntoon, T.J. Pinnavaia, *Advanced Materials* 13 (2001) 1263-1266.
- [137] T. Hibino, M. Kobayashi, *Journal of Materials Chemistry* 15 (2005) 653-656.
- [138] C. Jaubertie, M.J. Holgado, M.S. San Roman, V. Rives, *Chemistry of Materials* 18 (2006) 3114-3121.

- [139] N. Iyi, Y. Ebina, T. Sasaki, *Langmuir : the ACS journal of surfaces and colloids* 24 (2008) 5591-5598.
- [140] G.V. Manohara, D.A. Kunz, P.V. Kamath, W. Milius, J. Breu, *Langmuir : the ACS journal of surfaces and colloids* 26 (2010) 15586-15591.
- [141] J. ZHANG, Z. LIU, B. HAN, Z. LI, G. YANG, J. LI, J. CHEN, Preparation of silica and TiO<sub>2</sub>-SiO<sub>2</sub> core-shell nanoparticles in water-in-oil microemulsion using compressed CO<sub>2</sub> as reactant and antisolvent, Elsevier, Kidlington, ROYAUME-UNI, 2006.
- [142] V.M. Mohan, M. Shimomura, K. Murakami, *J Nanosci Nanotechnol.* 12 (2012) 433-438.
- [143] S. Chandren, B. Ohtani, *Journal of Photochemistry and Photobiology A: Chemistry* 246 (2012) 50-59.
- [144] J.-L. Hu, H.-S. Qian, J.-J. Li, Y. Hu, Z.-Q. Li, S.-H. Yu, *Particle & Particle Systems Characterization* 30 (2013) 306-310.
- [145] I.K. Konstantinou, T.A. Albanis, *Applied Catalysis B: Environmental* 49 (2004) 1-14.
- [146] D. Palomino, C. Yamunake, P. Le Coustumer, S. Stoll, *Journal of Colloid Science and Biotechnology* 2 (2013) 62-69.
- [147] C. Sentein, B. Guizard, S. Giraud, C. Yé, F. Ténégal, Dispersion and stability of TiO<sub>2</sub> nanoparticles synthesized by laser pyrolysis in aqueous suspensions, *Journal of Physics: Conference Series*, IOP Publishing, 2009, p. 012013.
- [148] W. Baran, A. Makowski, W. Wardas, *Dyes and Pigments* 76 (2008) 226-230.
- [149] M. Huang, C. Xu, Z. Wu, Y. Huang, J. Lin, J. Wu, *Dyes and Pigments* 77 (2008) 327-334.
- [150] U.G. Akpan, B.H. Hameed, *Journal of hazardous materials* 170 (2009) 520-529.
- [151] S. Liu, J.-H. Yang, J.-H. Choy, *Journal of Photochemistry and Photobiology A: Chemistry* 179 (2006) 75-80.
- [152] L.-C. Chen, C.-M. Huang, F.-R. Tsai, *Journal of Molecular Catalysis A: Chemical* 265 (2007) 133-140.
- [153] P. Bouras, E. Stathatos, P. Lianos, *Applied Catalysis B: Environmental* 73 (2007) 51-59.
- [154] P. Wei, J. Liu, Z. Li, *Ceramics International* 39 (2013) 5387-5391.
- [155] N. Riaz, F.K. Chong, B.K. Dutta, Z.B. Man, M.S. Khan, E. Nurlaela, *Chemical Engineering Journal* 185-186 (2012) 108-119.
- [156] N.A. Jamalluddin, A.Z. Abdullah, *Ultrasonics Sonochemistry* 18 (2011) 669-678.
- [157] K. Vinodgopal, D.E. Wynkoop, P.V. Kamat, *Environmental Science and Technology* 30 (1996) 1660-1666.
- [158] C. Bauer, P. Jacques, A. Kalt, *Journal of Photochemistry and Photobiology A: Chemistry* 140 (2001) 87-92.
- [159] A. Mills, *Applied Catalysis B: Environmental* 128 (2012) 144-149.
- [160] A. Houas, H. Lachheb, M. Ksibi, E. Elaloui, C. Guillard, J.-M. Herrmann, *Applied Catalysis B: Environmental* 31 (2001) 145-157.